UAB
Universitat Autònoma de Barcelona

# Tailoring the superconducting properties of YBa2Cu3O7–δ thin films by microstructure engineering and local oxygen doping

**Jordi Alcalà Barrat**

**ADVERTIMENT.** L'accés als continguts d'aquesta tesi queda condicionat a l'acceptació de les condicions d'ús establertes per la següent llicència Creative Commons: https://creativecommons.org/licenses/?lang=ca

**ADVERTENCIA.** El acceso a los contenidos de esta tesis queda condicionado a la aceptación de las condiciones de uso establecidas por la siguiente licencia Creative Commons: https://creativecommons.org/licenses/?lang=es

**WARNING.** The access to the contents of this doctoral thesis it is limited to the acceptance of the use conditions set by the following Creative Commons license: https://creativecommons.org/licenses/?lang=en







A dissertation submitted for the degree of
DOCTOR OF PHILOSOPHY IN MATERIAL SCIENCE

Universitat Autònoma de Barcelona
Departament de Física - Facultat de Ciències
Doctorat en Ciència de Materials

# Tailoring the superconducting properties of $YBa_2Cu_3O_{7-\delta}$ thin films by microstructure engineering and local oxygen doping

*Author:* Jordi Alcalà Barrat

*Supervisor:* Dr. Narcís Mestres Andreu

*Supervisor and Tutor:* Dr. Anna Palau Masoliver

Institut de Ciència de Materials de Barcelona (ICMAB-CSIC)

Superconducting Materials and Functional Nanoengineered Structures Group (SUMAN)

April 2024

*"I que ens vagin fent les trampes,*
*que ens anirem fent les lleis..."*

# Acknowledgements

After so many years and so much work, the result is reflected in this thesis, which would not have been possible without the direct and indirect help of so many people. Therefore, I begin by thanking ICMAB for allowing me to pursue the PhD in Material Science in its facilities and to all the workers who have made it so comfortable to work here.

Next, I would like to express my gratitude to my supervisors, Dr. Anna Palau and Dr. Narcís Mestres. Thank you for everything you have taught me over these years, for the assistance in all the discussions on how to prepare the experiments and analyze the results in different projects. Also, for your patience, guidance, trust, and the comfort of working together, as well as for the much-needed optimism in day-to-day work. I am very grateful to have been able to carry out the PhD with you.

I want to thank Prof. Teresa Puig, head of the Superconducting Materials and Functional Nanoengineered Structures Group, for the welcome she extended to me in the group and the comfort of being part of it. She, along with the former director of ICMAB, Prof. Xavier Obradors, provided valuable assistance with discussions and comments during different talks and presentations, as well as all the help and guidance in the EUROfusion project. Therefore, I also want to thank everyone who was part of that project: Dr. Susagna Ricard, Dr. Cornelia Pop, Dr. Laura Piperno and Pau Ternero.

I would like to thank all the members of the Department of Superconducting Materials and Functional Nanoengineered Structures: Prof. Xavier Granados, Dr. Jofre Gutiérrez, Dr. Mariona Coll, Dr. Roxana Vlad, Dr. Mar Tristany, Mariona de Palau, Guilherme, Martí, Neil, Meritxell, Ona, and all the former members: Joshua, Júlia, Artur, Hailin, Pengmei, Adrià, Poland Diana.

I am thankful to all my office mates, with whom I shared a lot of time within the same office but with many different people. Some were mentioned before, and I have to add Juri, Mathieu, Lavinia, Yunwei, Huan, Xao, Ais, Thomas and Alejandro R. Special thanks to Alejandro and Aleix, you have been like big and little brothers, respectively. We shared a lot time working together and also very good moments, thank you for all your help, support and for teaching me everything. I also want to add more people from ICMAB like Pamela, Pedro, Francesco, Adara, Irene, Sohini and Jewel, we shared very good moments in the lunch breaks.

Particular thanks to ICMAB-CSIC personnel, including administrative staff and scientific-technical services. Special mention to Dr. Bernat Bozzo and Dr. Ferran Vallès, from the Low Temperature and Magnetometry Lab, for all the help with the setup experiments and the magnetic characterization. Also to Raul Solanas, from Thin Films Lab, for the growth of PLD samples. I am very thankful to the Nanoquim staff for all the help, patience and change of a lot of reservations: Luigi, Neus, Rosa and the two Martas. Also thanks to Dr. Lluis Balcells for the help, guidance, the use of the sputtering and the discussions in some experiments.

From the two months stay in Milano I thank Dr. Edoardo Albisetti and Dr. Daniela Petti for the help and the opportunity to be part of their group in Polifab. Thanks to Valerio, Matteo V., Irene, Matteo P., Enrico, Simone and Davide, I will never forget the moments in the Nanofrazor, Wednesday lunches and the via ferrata.

Seguidament m'agradaria donar les gràcies als amics de la carrera: Josep, Elna i Adrià, pels bons moments que hem passat tot i triar camins diferents. Gràcies també a la meva gent de Reus pel suport, l'amistat i els grans moments: Sergi, Manel, Dani i Alejandro per una banda, i Lidia, Alba, Ana i Marina per l'altra. Segueixo donant les gràcies també als amics del camping, un grup de gent increïble que tot i la distància i el temps, sempre sou un pilar vital: Arnau, Marc, Bernat, Albert, Mireia, Pau, Josep, Anna, Carol, Far.

Moltes gràcies per tot i més a la Cunsu, a l'Antonio, a la Tere, al Juanpe i al Joan. Gràcies a la Cris per ser la millor referent. Gràcies per descomptat a la Tata, al Papa i a la Mama, per sempre estimar-me, creure i confiar en mi.

I finalment a la Marina, la millor companya de vida que podria triar. Gràcies per la paciència, l'ajuda, l'estima i per tants i tants moments.

# Abstract

Advances in the science of superconductivity have numerous challenges to improve old and create new technologies able to fulfil some of world the big challenges; ranging from power applications (storage and transport of clean, sustainable and reliable energy) to novel electronic devices (energy-efficient information technologies and data storage systems).

The individual and collective behavior of vortices (nano-tubes of magnetic flux) in a superconductor represents one of the most relevant physical aspects of these materials and it is of enormous practical significance for applications. This has sustained the study of different methods for engineering the vortex pinning landscape in order to infer in vortex dynamics of superconductors. Within this thesis, we have examined the impact of growth temperature on the formation of intrinsic pinning defects in $YBa_2Cu_3O_{7-\delta}$ (YBCO) films, grown by chemical solution deposition with Barium-deficient solutions. A clear correlation between the microstructure of the films and their superconducting performance have been obtained. An efficient pinning landscape consisting of stacking faults and associated nanostrain, naturally induced by simply tuning the growth temperature without the need to add artificial pinning sites. Samples grown at optimized temperature exhibited exceptionally high self-field $J_c$ values and improved $J_c(T, H, \theta)$ performances.

Moreover, high-temperature superconductors, in particular YBCO cuprates, offer unique opportunities to tune their physical properties with multiple external inputs, thus providing the basis for realizing energy-efficient electronic devices for information and communication technologies (sensors, logic and memory devices). In this direction, we have investigated field-induced oxygen doping to obtain reversible modulation of a metal-insulating transitions. The aim is to study the impact of field-induced oxygen diffusion on the magnetic field and angular

dependence of critical current density, discerning the role of induced defects in the switching performance. Results from transmission electron microscopy measurements reveal that the transition to irreversible high resistance states occurs through the formation of $YBa_2Cu_4O_7$ (Y124) intergrowths characterized by a significant presence of oxygen vacancies.

Finally, this work also focuses on pioneering a novel approach for tuning the superconducting properties of the films known as phase nano-engineering. This method utilizes a localized energy source applied to the material's surface through direct laser writing to induce property changes. The observed physical mechanism behind this is attributed to thermally activated oxygen migration within the written regions. Conductive AFM measurements demonstrate enhanced surface electric conductivity consistent with oxygen enrichment in the patterned regions. Furthermore, an enhancement of the reflectivity, reduced critical temperature, and critical current density in the patterned devices is obtained, as well as carrier density, indicative of oxygen vacancies generated in the bulk.

# Motivation and objectives

The aim of this thesis is to investigate different approaches to change and control the superconducting properties of YBCO thin films. The first approach involves the use of low temperature thin film growth using barium-deficient solutions through chemical solution deposition method to improve the pinning performance of YBCO films without the need of adding artificial pinning centres. A second approach involve the reversible manipulation of the metal-insulating transition in YBCO devices by field-induced oxygen doping. Finally, a third approach is used to explore the effect of thermally induced oxygen vacancies generated though direct laser writing.

The thesis is structured in different chapters. In Chapter 1 we introduce the main concepts of superconducting materials and the properties of high temperature cuprate superconductors, in particular YBCO. We provide a short overview of vortex pinning and oxygen doping in YBCO films. In Chapter 2 we describe the sample growth, micro- and nano-fabrication approaches, and the used characterization techniques.

The objective of Chapter 3 is to carefully analyse the morphology, angular, field, and temperature dependence of the critical current density of samples grown at different temperatures by chemical Barium-deficient solutions. Their perfomance is compared to pristine and nanocomposite YBCO films, to elucidate the nature and strength of pinning centres naturally induced when growing at low temperatures. Also the influence of the precursor solution and growth temperature on the doping level of the films will be evaluated.

The objective of Chapter 4 is to use field-induced resistive switching effects to study the critical current density performance of YBCO films at different oxygen doping levels. The effect of oxygen doping on the magnetic field and angular dependence of the critical current density may be of great relevance for the optimization of flux pinning through

microstructural modification. So the critical temperature, carrier density, critical current density at different resistance levels is measured. Here we will try to selectively tune the doping level of superconducting tracks by applying voltage pulses under metallic gates of different areas. Transmission electron microscopy experiments will be performed at low and high resistive states to study the generation of a large amount of $YBa_2Cu_4O_7$ (Y124) intergrowths with a high density of oxygen vacancies.

The objective of Chapter 5 is to achieve tunable local modifications in the electronic properties of YBCO thin films by employing Direct Laser Writing. The impact of laser patterning under different conditions, such as exposure dose, on the electronic properties will be studied by optical imaging and conductive Atomic Force Microscopy. Low-temperature transport measurements will be conducted on patterned YBCO films to obtain the critical temperature, the carrier density and dependencies on the critical current density, indicative of the oxygen movement.

# Nomenclature

**AFM** Atomic Force Microscopy

**APCs** Artifical Pinning Centres

**BHO** $BHfO_3$

**BZO** $BaZrO_3$

**CCs** Coated Conductors

**CSD** Chemical Solution Deposition

**CTA** Conventional Thermal Annealing

**EBL** Electron Beam Lithogrpahy

**DLW** Direct Laser Writing

**FH** Flash Heating

**GADDS** General Area Detector Diffraction System

**HTS** High Temperature Superconductors

**LAO** Lanthanum Aluminate

**LP** Laser Power

**LT** Laser Time

**MOD** Metal Organic Deposition

**NCs** Nanocomposites

**PLD** Pulsed Laser Deposition

**PPMS** Physical Property Measurement System

**SEM** Scanning Electron Microscopy

**SFs** Stacking Faults

**SQUID** Superconducting Quantum Interference Device

**TEM** Transmission Electron Microscopy

**TFA** Trifluoroacetate

**t-SPL** Thermal Scanning Probe Lithography

**XRD** X-Ray Diffraction

**YBCO** $YB_2Cu_3O_{7-x}$

$\alpha$ Power Law Index $J_c(H)$

$\gamma$ Intrinsic Anisotropy

$\gamma_{eff}$ Effective Anisotropy

$\delta$ Lattice Parameter

$\epsilon$ Nanostrain

$\theta$ Diffraction angle

$\lambda_L$ Penetration Length

$\mu_0$ Magnetic Permeability of Vacuum

$\xi_0$ Coherence Length

$\Phi$ Magnetic Flux Quantum

$\mathbf{E}_p$ Pinning Energy

$\mathbf{F}_L$ Lorentz Force

$\mathbf{F}_P$ Pinning Force

$\mathbf{H}_{eff}$ Effective Magnetic Field

$\mathbf{H}^*$ Crossover Magnetic Field

$\mathbf{H}_{irr}$ Irreversivility Magnetic Field

$\mathbf{H}_c$ Critical Magnetic Field

$\mathbf{H}_{c1}$ Upper Critical Magnetic Field

$\mathbf{H}_{c2}$ Upper Critical Magnetic Field

$\mathbf{I}_c$ Critical Current

$\mathbf{J}_c$ Critical Current Density

$\mathbf{n}_H$ Charge Carrier Density

$\mathbf{T}_0$ Characteristic Weak Pinning Temperature

$\mathbf{T}_0^*$ Characteristic Strong Pinning Temperature

$\mathbf{T}^*$ Pseudogap Temperature

$\mathbf{T}_c$ Critical Temperature

$\mathbf{V}_H$ Hall Voltage

**aniso** Anisotropic

**iso** Isotropic

**sf** Self-field

**str** Strong

**wk** Weak

# Contents

**Acknowledgements** **i**

**Abstract** **v**

**Motivation and objectives** **vii**

**Nomenclature** **ix**

**1 Introduction** **1**
1.1 Superconductivity . . . . . 1
1.1.1 Type I and type II superconductors . . . . . 5
1.1.2 Vortices in type II superconductors . . . . . 7
1.1.3 BCS theory of superconductivity . . . . . 12
1.1.4 Josephson effect . . . . . 14
1.1.5 Unconventional HTS . . . . . 15
1.2 YBCO cuprate HTS . . . . . 17
1.2.1 Vortex pinning . . . . . 19
1.2.2 Oxygen doping . . . . . 24

**2 Experimental methodology** **29**
2.1 YBCO Thin film growth . . . . . 29
2.1.1 Substrates . . . . . 29
2.1.2 Chemical Solution Deposition (CSD) . . . . . 30
2.1.2.1 Solution synthesis . . . . . 30
2.1.2.2 Deposition . . . . . 31
2.1.2.3 Pyrolysis . . . . . 32
2.1.2.4 Growth and oxygenation . . . . . 34
2.1.3 Pulsed Laser Deposition (PLD) . . . . . 36
2.2 YBCO thin film characterization . . . . . 37
2.2.1 X-ray diffraction . . . . . 38

2.2.2 SQUID dc-magnetometry . . . . . 40
2.2.3 Profilometer . . . . . 43
2.2.4 Atomic Force Microscopy . . . . . 44
2.2.5 Scanning Electron Microscopy . . . . . 45
2.2.6 Scanning Transmission Electron Microscopy . . 46
2.3 Micro & Nano-fabrication . . . . . 47
2.3.1 Photolithography . . . . . 47
2.3.2 Electron Beam Lithography . . . . . 53
2.3.3 Thermal Scanning Probe Lithography . . . . . 55
2.4 Electrical transport measurements . . . . . 56
2.4.1 Wire bonding . . . . . 57
2.4.2 Physical Property Measurement System . . . . 58
2.4.2.1 $T_c$ and $J_c$ measurements . . . . . 60
2.4.2.2 Hall measurements . . . . . 61
2.4.3 Source Measure Unit (SMU) . . . . . 64

**3 Ba-deficient solutions for high-performance superconducting YBCO films 67**
3.1 Barium-deficient solutions . . . . . 69
3.2 Patterning of YBCO films for transport measurements 70
3.3 Microstructural characterization . . . . . 71
3.4 Influence of growth temperature on the superconducting performance . . . . . 76
3.5 Pinning landscape of YBCO thin films grown at low temperatures . . . . . 80
3.5.1 Magnetic field dependence of $J_c$ at $H//c$ . . . . 80
3.5.2 Angular magnetic field dependence of $J_c$ . . . . 81
3.5.3 Nature and strength of pinning centres . . . . . 85
3.6 Influence of the carrier density on Jc . . . . . 87
3.7 Conclusions . . . . . 89

**4 Electric field-induced oxygen doping in YBCO films 91**
4.1 Oxygen doping in YBCO films of different thickness . . 93
4.2 Device fabrication . . . . . 96
4.3 Gate modulation of the RS effect . . . . . 99
4.4 Gate modulation of the YBCO bridge resistance . . . . 101
4.5 Gate modulation of the SC performance . . . . . 104
4.5.1 Impact of field-induced oxygen doping on $T_c$ . . 105
4.5.2 Impact of field-induced oxygen doping on $J_c$ . . 107

4.6 Conclusions . . . . . 113

**5 Thermally-induced oxygen doping in YBCO films 115**
5.1 Device fabrication . . . . . 116
5.2 Direct Laser writing in YBCO films . . . . . 117
5.2.1 Adjustment of the laser focus . . . . . 117
5.2.2 Laser power and writing time . . . . . 118
5.2.3 Thickness dependence of laser irradiation . . . . 120
5.3 Impact of laser patterning on the SC performance . . . 121
5.3.1 Impact of laser-induced oxygen doping on $T_c$ . . 124
5.3.2 Impact of laser-induced oxygen doping on $J_c$ . . 126
5.3.3 Local laser irradiation: Pattern with lines . . . 129
5.4 Conclusions . . . . . 130

**6 General Conclusions 133**

**Publications 137**

**Bibliography 139**

# Chapter 1

# Introduction

## 1.1 Superconductivity

On April 8, 1911, at the Leiden Cryogenic Laboratory in the Netherlands, Heike Kamerlingh Onnes and his team made a remarkable discovery: the phenomenon of superconductivity in mercury. This breakthrough emerged as a result of Onnes' investigations into cryogenic techniques aimed at achieving temperatures approaching absolute zero. In 1908, he successfully liquefied helium, which required temperatures only a mere 4 degrees above absolute zero.

Their research involved the examination of mercury's electrical properties at extremely low temperatures. Upon reaching a temperature of 4.2K (critical temperature), the electrical resistance of mercury vanished [1–3] as can be seen in Fig.1.1. Below the critical temperature, $T_c$ (intrinsic property of superconductors) the material conducts electricity with utmost efficiency.

In 1933, Walther Meissner and Robert Ochsfeld made anothe significant discovery. They found that materials in the superconducting phase, in addition to exhibiting the remarkable property of having no electrical resistance, also possess the ability to repel magnetic fields. When a superconductor is cooled below its transition temperature, while subjected to an applied magnetic field, it behaves as a perfect diamagnet and expels the magnetic field entirely [4]. This expulsion occurs through the generation of surface superconducting electrical currents, known as supercurrents, which effectively shield the interior from the applied magnetic field.

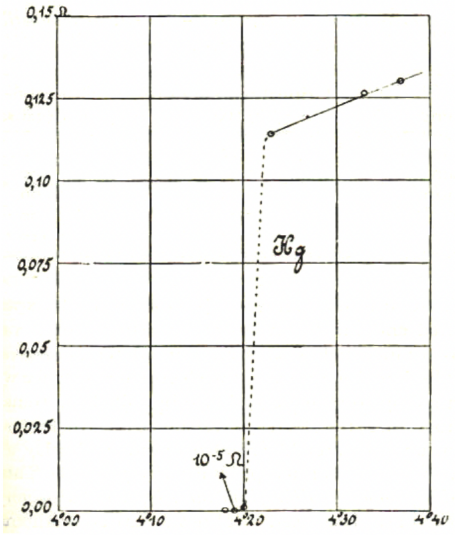



Figure 1.1: Historical graph done by H.K. Onnes of the Hg resistance as a function of the temperature. It is easy to see the transition at 4.20K when the material become superconductor.

This phenomenon is famously called the Meissner effect and it is the responsible for magnetic levitation. Importantly, the exclusion of the magnetic field from a superconductor occurs whether the material becomes superconducting before or after the external magnetic field is applied.

In 1935, siblings Fritz and Heinz London put forth a phenomenological "modification" to Maxwell's fundamental equations. These adjustments aimed to describe the two fundamental characteristics of superconductors: zero electrical resistance and the exclusion of magnetic fields [5, 6]. The first London equation says that a supercurrent $\mathbf{j}_s$ is freely accelerated by an applied voltage, or, in a bulk superconductor with no supercurrent or with a stationary supercurrent there is no effective electric field $\mathbf{E}$. It can be expressed as:

$$\frac{\partial \mathbf{j}_s}{\partial t} = \frac{n_s e^2}{m}\mathbf{E} \tag{1.1}$$

where $m$ is the mass of the electron, $e$ the charge of the electron and $n_s$ a phenomenological constant associated with a number density of superconducting carriers. Taking curl on both sides of Eq.(1.1),

combining it with the third Maxwell's equation (Faradays law of electromagnetic induction) and integrating in both sides assuming the constant of integration to be zero because of the zero resistivity in superconductors, we get the following expression:

$$(\nabla \times \mathbf{j}_s) = -\frac{n_s e^2}{m}\mathbf{B} \tag{1.2}$$

which is the second London equation. It yields the ideal diamagnetism, the Meissner effect, and the flux quantization. If it is altered through the application of Ampere's law then it can be turned into the Helmholtz equation for magnetic field:

$$\nabla^2\mathbf{B} = \frac{1}{\lambda_s^2}\mathbf{B} \qquad\qquad \lambda_s \equiv \sqrt{\frac{mc^2}{4\pi n_s e^2}} \tag{1.3}$$

where $\lambda_s$ is the London penetration depth and the solution of the Eq.(1.3) is the following

$$B_z(x) = B_0 e^{-x/\lambda_s} \tag{1.4}$$

According to this last equation, in the presence of an external magnetic field $B_0$ applied perpendicular to the surface, London theory predicts that the magnetic flux decays exponentially into the bulk of the superconductor, just as depicted in Fig1.2.

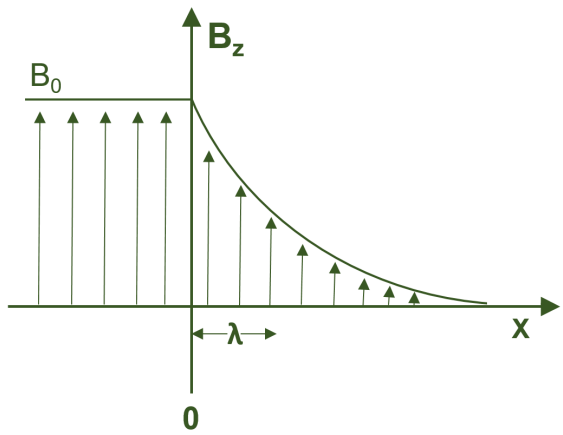



Figure 1.2: Representation of the exponentially decay of the the magnetic flux into the bulk of the superconductor in the x-direction.

Despite the success of this theory in describing several aspects of the electrodynamics of superconductivity, falls short when it comes to determining the surface energy at the interface between the Normal and Superconducting phases [7].

In 1950, V. L. Ginzburg and L. D. Landau introduced a phenomenological model of superconductivity. This model presented a macroscopic theory suggesting that, at the critical temperature, the conductor undergoes a phase transition into the superconducting state. To describe this transition, they introduced a complex pseudo wave function $\psi$, which serves as an order parameter for superconducting electrons [8, 9]. Similar to other second-order phase transitions, the order parameter is non-zero in the ordered phase and becomes zero in the non-ordered phase. They expressed that the free energy density of a superconductor close to the superconducting transition can be represented as

$$f_s = f_n + \alpha|\psi|^2 + \frac{\beta}{2}|\psi|^4 + \frac{1}{2m}\left|(-i\hbar\nabla - 2e\mathbf{A})\,\psi\right|^2 + \frac{|\mathbf{B}|^2}{2\mu_0} \tag{1.5}$$

where $f_n$ is the free energy density in the normal phase, $m$ is the mass of the electron, $e$ the charge of the electron, $\boldsymbol{B}$ the magnetic field, $\boldsymbol{A}$ the magnetic vector potential which represents the action of a constant magnetic field and $\alpha$ and $\beta$ are temperature-dependent parameters. When you minimize the free energy concerning changes in both the order parameter and the vector potential, you reach the Ginzburg-Landau equations:

$$\frac{1}{2m}\left(-i\nabla - \frac{e}{c}\mathbf{A}\right)^2\psi + \beta|\psi|^2\psi = -\alpha\psi \tag{1.6}$$

$$\mathbf{j}_s = -i\frac{e}{2m}\left(\psi^*\nabla\psi - \psi\nabla\psi^*\right) - \frac{e^2}{mc}|\psi|^2\mathbf{A} \tag{1.7}$$

The initial equation, exhibiting intriguing resemblances to the time-independent Schrödinger equation, ascertains the order parameter $\psi$ in relation to the applied magnetic field. Subsequently, the second equation furnishes information about the superconducting current. The Ginzburg-Landau equations yield numerous substantiated findings and

among these, perhaps the most crucial is their anticipation of the presence of two distinct characteristic lengths within a superconductor [10]. The first of these is known as the coherence length $\xi$ which describes the size of thermodynamic fluctuations in the superconducting phase (description of the spatial modulation of the order parameter ($\psi$(x)):

$$\xi = \sqrt{\frac{\hbar^2}{2m|\alpha|}} \tag{1.8}$$

The other one is the penetration depth (analogous as London penetration depth), where $\psi_0$ represents the order parameter's equilibrium value when there is no electromagnetic field present. The penetration depth defines how deeply an external magnetic field can penetrate the superconductor:

$$\lambda = \sqrt{\frac{m\beta}{4\mu_0 e^2|\alpha|}} = \sqrt{\frac{m}{4\mu_0 e^2\psi_0^2}} \tag{1.9}$$

### 1.1.1 Type I and type II superconductors

In terms of temperature, the two superconductor characteristic lengths, $\lambda$(T) and $\xi$(T), have the same dependence [11]:

$$\xi(T) = \frac{\xi_0}{\sqrt{1-\frac{T}{T_c}}} \qquad \lambda(T) = \frac{\lambda_0}{\sqrt{1-\frac{T}{T_c}}} \tag{1.10}$$

The Ginzburg-Landau Parameter, denoted as $\kappa$ and defined as $\kappa$=$\lambda/\xi$, serves as a distinguishing factor between two distinct categories of superconductors. The first family is the Type I superconductors and it happens when $\kappa < 1/\sqrt{2}$. In this case $\xi \gg \lambda$ and the penetration of the magnetic field into the superconducting material is not energetically favourable. By contrary, if $\kappa > 1/\sqrt{2}$ then we have a Type II superconductor which means that $\lambda \gg \xi$ and it is thermodynamically favourable for the magnetic field to penetrate the specimen [12]. Fig.1.3 shows the variation of $H$ and $\psi$ with $\lambda$ and $\xi$ in a normal state / superconductor boundary.

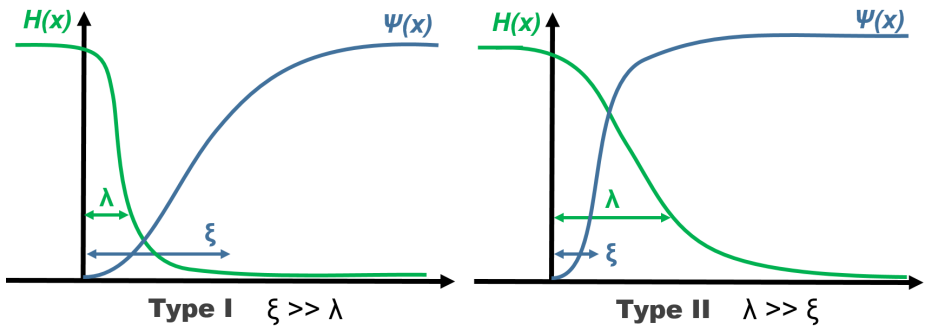



Figure 1.3: Variation of $H(x)$ and $\psi(x)$ where depending on the magnitute of $\xi$ and $\lambda$ a type-I or type-II superconductor is defined.

The Magnetic Field-Temperature (H-T) phase diagram of type I and type II superconductors is shown in Fig.1.4. Type I materials maintain their superconducting state only under relatively weak applied magnetic fields. Once a specific field threshold is surpassed, called critical magnetic field, $H_c$, the material transit to the normal state. These materials display an extremely sharp transition into a superconducting state and demonstrate "perfect" diamagnetism, meaning they have the ability to entirely repel a magnetic field (Meissner state).

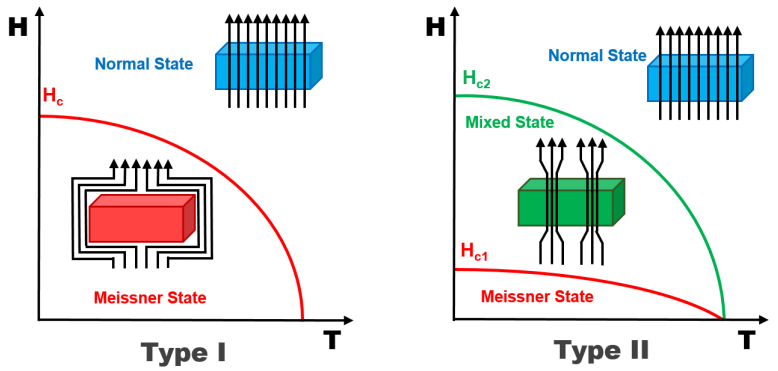



Figure 1.4: Representation of the magnetic field dependence on temperature a) in a type-I superconductor where $H_c$ separates the normal and the Meissner state, b) in a type-II superconductor where a mixed state is defined between $H_{c1}$ and $H_{c2}$.

Type II superconductors allow the penetration of magnetic fields to some extent. Starting from the Meissner state where the magnetic field is repeled, up to a certain critical magnetic field, $H_{c1}$, where above it,

there is the mixed state characterized by regions of normal conductivity interspersed with areas of superconducting current forming quantized cylindrical flux lines called vortices [5]. The mixed state exists up to a second critical magnetic field, $H_{c2}$, where above it the material conducts in the normal state. This attribute allows type II SC to carry larger currents without losing their superconductivity. This behavior has paved the way for the use of superconductivity in high magnetic field applications, leading to the development of magnets used in particle accelerators.

### 1.1.2 Vortices in type II superconductors

Type-II superconductors present an extended region in the H-T phase diagram, called the mixed state, where magnetic field penetrate in form of Vortices. These vortices engage in mutual interactions and have the potential to assume various phases due to the combined effects of the magnetic field, thermal fluctuations, as well as the pinning influence exerted by disorder and defects within the material. Such a vortex comprises a non-superconducting core (radius of the order of $\xi$ = 2 - 100 nm) around which superconducting current circulates (radius of the order of $\lambda$ = 40 - 1000 nm), as represented in Fig.1.5a. The total flux of a vortex is the magnetic flux quantum $\Phi_0$, that corresponds to the minimum unit of the quantized magnetic flux ($\Phi_0 = 2.07 \cdot 10^{15}$ Tm$^2$) [13, 14].

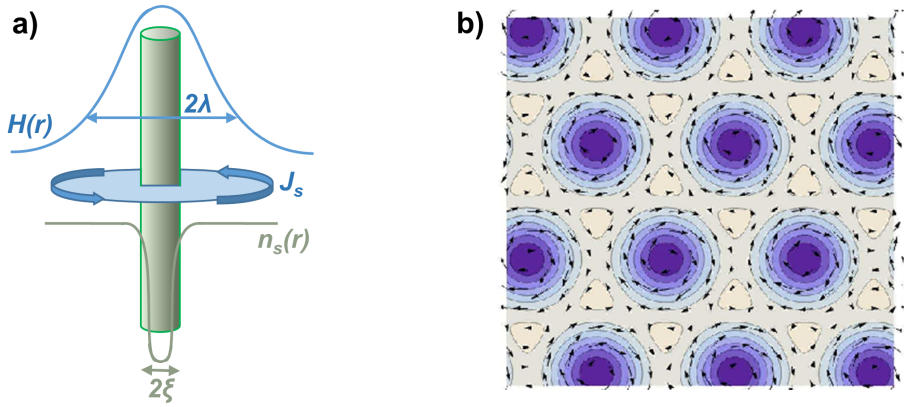



Figure 1.5: Image of a) the structure and characteristic parameters of a vortex, b) superconducting currents around the vortex centers in the hexagonal Abrikosov lattice [15].

In 1957, the Russian physicist A. A. Abrikosov made a groundbreaking prediction about the existence of vortices in type II SC [16, 17]. He accomplished this by examining solutions to the Ginzburg-Landau (GL) equations for $\kappa > 1/\sqrt{2}$, specifically focusing on the scenario where the externally applied magnetic field was just slightly below the critical field $H_{c2}$. In this region, he derived approximate solutions reminiscent of those found in linearized GL equations [6]. These solutions unveiled the emergence of a periodic microscopic magnetic field distribution, oriented perpendicular to the applied field. To be more precise, his work foresaw the formation of a periodic square array of vortices also called fluxons [18].

At the vortex center where the magnitude of the local field is largest, the density of superconducting electrons $n_s$ and hence the order parameter $\Psi(\vec{r})$ is zero. As one moves radially out from the center of a vortex core, $n_s$ increases and the supercurrents screen a greater amount of flux. It follows that the density of the supercurrents is greatest near the edge of the vortex core where the screening of the local magnetic field is at a maximum.

Outside of the vortex core, magnetic field leaks into the superconducting regions of the sample. It is worth emphasizing that Abrikosov's prediction of the vortex state was noteworthy because it initially did not offer any tangible experimental evidence to confirm its existence. He also derived the following relations between $H_c$, $H_{c1}$ and $H_{c2}$:

$$H_{c1} = \frac{H_c}{\kappa}\,(ln(\kappa) - 0.27) \qquad\qquad H_{c2} = H_c\sqrt{2}\kappa \tag{1.11}$$

Vortices repel each other forming an ordered lattice, in order to minimize the system total energy. In absence of defects, they arrange in a regular array forming an hexagonal lattice, known as the Abrikosov lattice (Fig.1.5b). Considering $a_0$ as the vortex distance, can be related with the applied magnetic field as $a_0 = \sqrt{\Phi_0/B}$. In the mixed state, as soon as the flux lines (with a normal core) start to move across the superconductor, energy dissipation appears and it shows a non-zero resistance. Vortices move according to a Lorentz-like Force, $F_L$, that is perpendicular to both applied magnetic field and current, they dissipate the energy when moving under applied currents [6, 10, 12, 19].

In order to avoid dissipation, vortex must be pinned inside the material for technological applications, so a pinning force, $F_P$, opposite to the Lorentz Force must be generated:

$$\left|\vec{F_P}\right| = \left|\vec{F_L}\right| = \left|\vec{J_c} \times \vec{B}\right| \tag{1.12}$$

where $J_c$ is the critical current density and is the maximum current that can flow in the superconductor without dissipation. Below $J_c$ ($F_L < F_P$), no dissipation is obtained, while above, ($F_L > F_P$ ), a voltage drop develops due to vortex motion. Hence, the depinning of vortices and, with that, the upper threshold for lossless current conduction are directly linked to the effective defect landscape that immobilizes vortices.

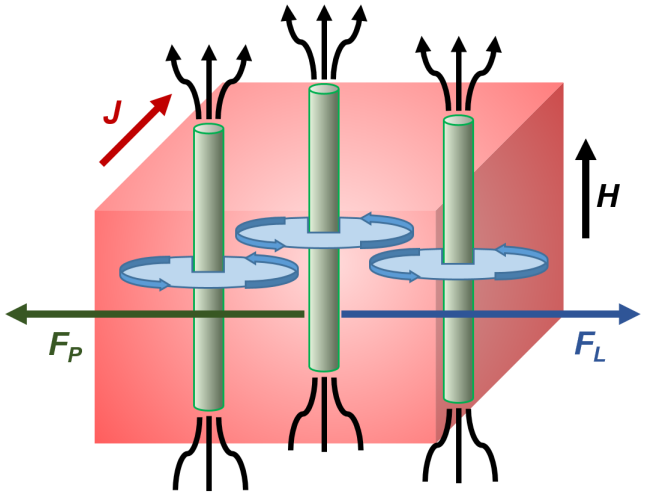



Figure 1.6: Representation of the vortices motion with a Lorentz Force $F_L$ perpendicular to both $J$ and $H$. Also a pinning force $F_P$ in the opposite side in order to pin the vortices and avoid dissipation.

In general vortex pinning is due to the saving in condensation energy associated with the vortex core which arise when it is situated within a non-superconducting inclusion (1.13).

$$\varepsilon_{core} \approx \mu_0 H_c^2 \xi^2 \approx \frac{\Phi_0^2}{\lambda^2} \tag{1.13}$$

The presence of vortices in type-II superconductors leads to a magnetic hysteresis loop(Fig.1.7a), which can be used to calculate the crit-

ical current density through non-destructive inductive measurements. When the material is cooled below its critical temperature in zero magnetic field (ZFC), and an external magnetic field stronger than the lower critical field ($H_{c1}$) is applied, vortices start to enter inside the material and migrate toward the center of the sample with increasing field strength. Due to vortex pinning, the density of magnetic flux lines is more concentrated at the edges of the material and gradually diminishes towards the interior creating a flux gradient (Fig.1.7b).

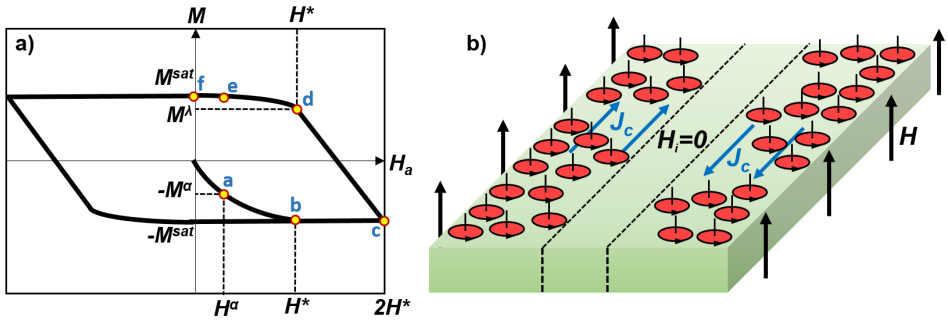



Figure 1.7: Schematics of a) the magnetic hysteresis loop with characteristic points commented also in Fig.1.8 and b) vortex penetration according to the Bean critical state model in an infinite slab.

The Bean's critical state model, which was introduced by C. P. Bean in 1962, provides a macroscopic explanation for the irreversible magnetization behavior in hard type-II superconductors [20]. Bean proposed a simple mechanism of non-homogeneous vortex penetration in the mixed state ($H_{c1} < H < H_{c2}$), attributed to the presence of vortex pinning in the material.

The Bean's critical state model is characterized by a critical current density independent of the magnetic field, with $J_c =$ constant. Considering an infinitely long cylinder, the magnetic hysteresis loop obtained by increasing and decreasing the applied magnetic field (Fig.1.7a) can be described by the magnetic flux and current distribution depicted in Fig.1.8 for different points indicated in the hysteresis loop.

At low applied field (Fig.1.8a) vortices starts to penetrate inside the superconductor with a constant field slope. $J_c$ is assumed to be constant inside the sample (field gradient constant) and in the flux free regions, where no flux gradients are present, $J_c = 0$. When the internal

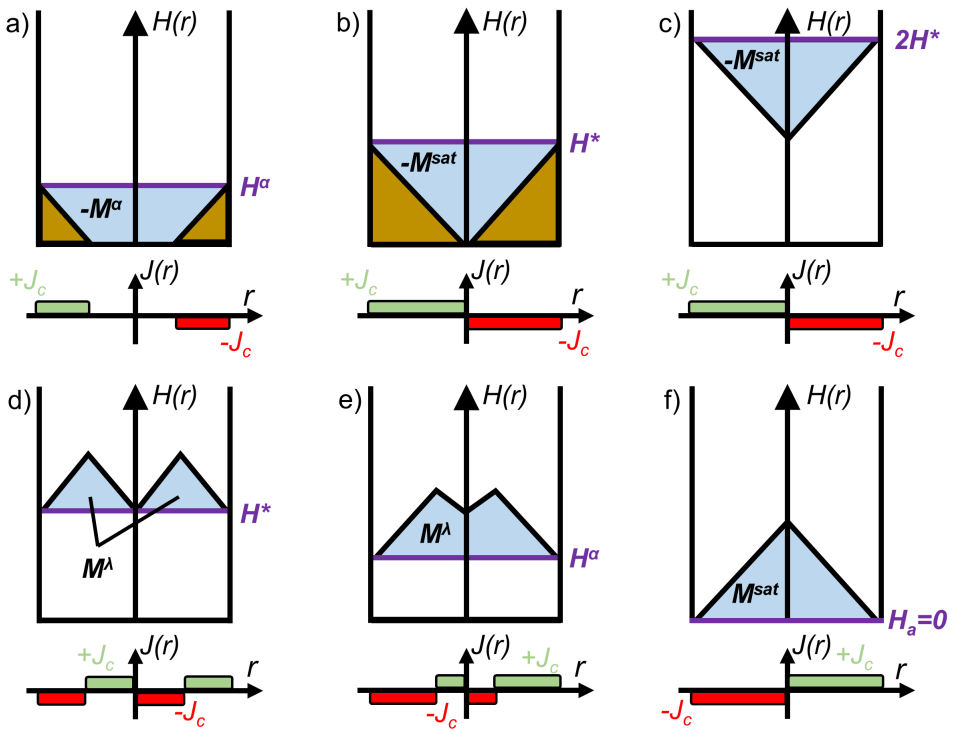



Figure 1.8: Scheme of the magnetic field and current profiles as a function of the applied field of an infinite cylinder of radius $R$, according to the Beam model. The associated points at the hysteresis loop are indicated in Fig.1.7a.

field reaches the centre of the sample there is a full penetration field, where $H^* = RJ_c$. Supercurrents are induced in the whole sample and the magnetization saturates, $M^{sat}$ (Fig.1.8b). The field profile reached at this point stays constant ($M^{sat}$) as the magnetic field is further increased to $2H^*$ (Fig.1.8c).

After this we start decreasing the magnetic field and the supercurrents invert their direction from the superconducting surface (flux lines start to leave from the superconductor by its edges reverting the magnetic flux gradient). The flux is trapped inside the superconductor and the current direction is determined by the slope of $H_i(r)$, if $H_i > H_a$ then we have a positive magnetization (Fig.1.8d). Finally once the magnetic field is completely removed, all supercurrents have changed their direction with a resulting saturated remanent magnetization (Fig.1.8f).

Within the framework of the Bean critical state model, where $R$ represents the cylinder radius and $\Delta M$ stands for the width of the saturated hysteresis loop in the $M$-$H$ curve, the critical current density for an infinitely long cylinder can be determined by utilizing the following expression based on the saturated magnetization value [21–23]:

$$J_c = \frac{3\Delta M}{2R} \tag{1.14}$$

In the case of a real finite superconductor, the critical current density is not constant with respect to the magnetic field, as presumed in the Bean model and moreover it becomes necessary to consider demagnetizing effects [24, 25], which in turn influence the penetration of current within the sample and the profiles of the magnetic field due to edge effects. With regard to superconducting thin films, their geometric characteristics result in the internal magnetic field being nearly identical to the external field. Consequently, when dealing with thin samples, same equation 1.14 can be applied to ascertain the value of $J_c$ while considering the magnetic field's dependence on saturated magnetization, $M(H)$.

### 1.1.3 BCS theory of superconductivity

In 1957 Bardeen, Cooper, and Schrieffer (BCS) put forth a groundbreaking theory that elucidated the microscopic mechanism of superconductivity and had the capability to predict the properties of conventional superconductors with quantitative precision [26, 27]. The pivotal initial step was taken by Cooper, who demonstrated that, at low temperatures, electrons could form pairs, named as "Cooper pairs."

A crucial advancement toward comprehending superconductivity involved the recognition of the existence of a band gap, separating the charge carriers from the normal conduction state. This energy gap aligned with the exponential temperature dependence observed in specific-heat measurements as the temperature neared the critical temperature, as documented in [28]. With rising temperature, there was an exponential growth in the number of particles possessing adequate energy to bridge this gap. Also is important to mention that in 1950,

C.A. Reynols and E. Maxwell observed that the transition temperature of mercury varied depending on the specific isotope used in the sample, strongly implying the involvement of lattice vibrations, known as “phonons,” in the phenomenon of superconductivity [29, 30].

The core of the BCS theory is that, in the superconducting state, electrons can form pairs due to a weak interaction, a phenomenon termed Cooper pairing. The ”glue” that holds electron pairs together, despite their Coulomb repulsion is mediated by the vibrations of the ion lattice, as schematically represented in Fig.1.9). According to the BCS theory, when an electron (red dot) moves through the lattice (blue dots), it induces a slight distortion or ripple in its vicinity due to its attraction to the lattice. Another electron traveling in the opposite direction is then drawn toward this disturbance, forming a connection between the two electrons.

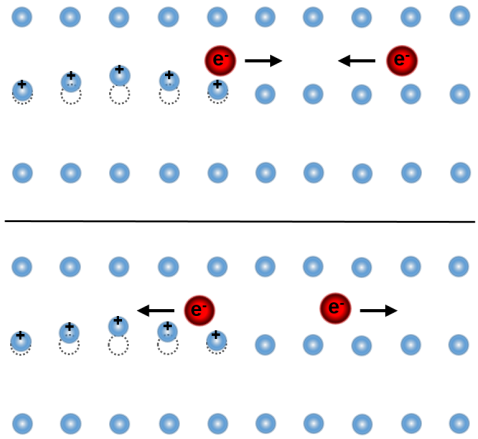



Figure 1.9: Visual representation of the Cooper pair attraction.

One the electrons are coupled as Cooper pairs they condense into the same energy level and behave like bosons, which can move coherently through the lattice without any losses. The Cooper pair condensate can be described by a single coherent wave function with a certain amplitude and phase in which their collective motion is synchronized. An energy gap, typically around several meV, is established above the Cooper pairs, preventing their separation into normal electrons, that would have collision interactions with the lattice responsible for resistivity. For Cooper pairs to form it is essential that the lattice’s thermal vibrations remain sufficiently small.

### 1.1.4 Josephson effect

After the formulation of the BCS theory, another pivotal moment in the field of superconductivity occurred in 1962 when Brian Josephson, at Cambridge University in the UK, made a groundbreaking prediction [31]. He proposed that an electric current could tunnel through a thin insulating or normal metal barrier, connecting two superconductors (Fig.1.10). This phenomenon, recognized today as the Josephson effect, had profound implications [32].

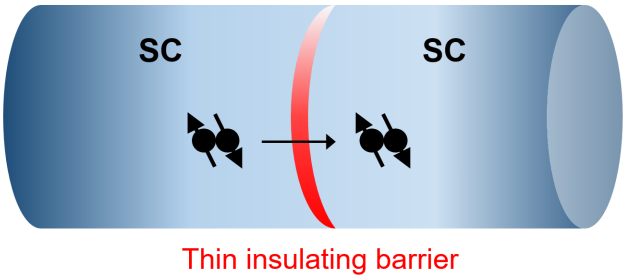



Figure 1.10: Scheme of a Josephson junction. A thin insulator barrier of few nanometers separates the two superconductors (tunnel junction). The overlap of the macroscopic wave functions allows the tunneling of the Cooper pair.

In the DC Josephson effect there is a Josephson current (supercurrent) that manifests itself within a tunnel barrier even in the absence of an applied voltage. This current exhibits a sinusoidal dependence on the disparity between the phase of superconducting waves on either side of the barrier: $I_c = I_{c0} sin(\varphi)$, where $I_{c0}$ is the maximum possible critical current determined by the tunneling of the junction and $\varphi$ the Josephson phase: phase difference of the superconducting wave functions of the two electrodes $\varphi = \varphi_L$ - $\varphi_R$.

On the contrary, in the AC Josephson effect a DC voltage $V_0$ is applied to a Josephson junction and an AC current with frequency $f_J$ proportional to the voltage across the junction occurs [33]. The emitted radiation at this frequency $f_J$ can be precisely measured (Eq.1.15). As a result, Josephson junction devices have evolved into the established standard for voltage measurement.

$$I_s = I_c sin(2\pi f_J t + \varphi(0)) \qquad f_J = \frac{V_0}{\Phi_0} = V_0 \cdot 483.6 \cdot 10^{12}(Hz) \quad (1.15)$$

The discovery of the Josephson effect paved the way for the development of Superconducting Quantum Interference Devices (SQUIDs). These are compact, highly sensitive devices that exploit tunnel barriers and Josephson currents to detect magnetic fields with remarkable precision.

### 1.1.5 Unconventional HTS

In 1986, Georg Bednorz and Alex Müller made a revolutionary discovery when they discovered high-Temperature superconductivity (HTS) in layered copper-oxide perovskites at temperatures exceeding 30 K [34]. Initially, they focused their research on materials comprising barium, copper, and lanthanum. Through meticulous adjustments in the ratios of barium and lanthanum, they systematically altered the electron count within these compounds. Astonishingly, amidst these experiments, they uncovered one particular compound that exhibited superconductivity at a previously unparalleled temperature. What rendered this discovery truly extraordinary was the fact that ceramics typically act as insulators.

Fig.1.11 shows the discovery of superconducting materials, classified in different families, and their critical temperature. The first family discovered, conventional superconductors (represented as green circles) can be explained by the BCS electron-phonon coupling mechanism, and comprehend pure elements, alloys and composite materials. In general this materials have low critical temperatures ($T_c < 30$ K) at atmospheric pressure. Recently discovered hydrogen sulfide belongs to this family of materials, where its superconductivity appears under extreme pressure conditions of 155 GPa and $T_c = 203$ K [35, 36].

In the late 1970s, novel categories of superconductors emerged, such as heavy-fermion superconductors (green starts), followed by unconventional High-Temperature oxide cuprates in the 1980s (blue diamonds). In recent times, additional unconventional superconductors have emerged, including certain carbon-based materials like fullerides (purple triangles) and iron pnictides (yellow squares) [37]. The copper oxide compounds, referred to as cuprates, represent the foremost group of HTS (blue diamonds in Fig.1.11). These materials exhibit superconducting properties at the most elevated temperatures, making them exceptionally intriguing for various applications.

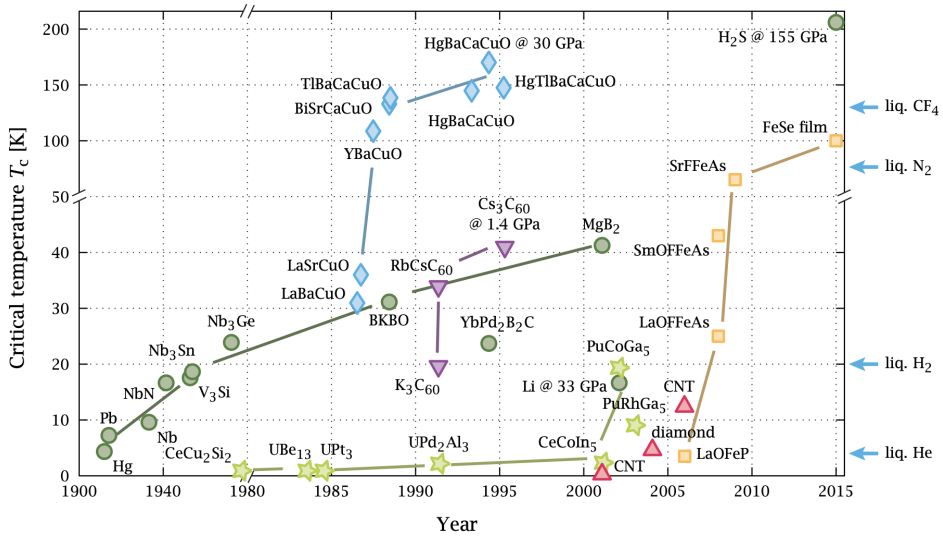



Figure 1.11: Timeline of the discovered superconductors and their critical temperature classified in different families of materials [37].

A shared characteristic among all superconducting cuprates is the existence of two-dimensional planes composed of copper and oxygen, denoted as $CuO_2$ planes, which are interspersed with charge reservoir blocks [38].

Regarding pairing, in contrast to the straightforward that is symmetric s-wave gap observed in conventional superconductors, cuprates exhibit a $d_{x^2-y^2}$-wave gap that is non-symmetric. In terms of doping, these substances function as antiferromagnetic Mott insulators in their pristine, stoichiometric state (without any extra oxygen or dopant atoms introduced).

Despite some decades of rigorous investigation, the source of high-temperature superconductivity remains elusive. It appears that, unlike conventional superconductivity, which relies on electron-phonon attraction mechanisms, high-temperature superconductivity is likely driven by authentic electronic mechanisms, such as those arising from antiferromagnetic correlations. Some exemples of these compounds would be $HgBa_2CuO_{4+\delta}$ (Hg1201), $La_{2-x}Sr_xCuO_4$, $Tl_2Ba_2CuO_{6+\delta}$ and $YBa_2Cu_3O_{7-\delta}$ (YBCO).

In February 2008, Hideo Hosono and his team made a innovative announcement: the revelation of superconductivity at 26 K in an Iron-Based Material [39] (yellow squares in Fig.1.11). Given that elemental iron exhibits strong magnetism, the discovery of high-transition-temperature superconductors based on iron (FeSCs) came as a completely unforeseen development.

Both cuprates and iron-based superconductors share a common structural characteristic as layered materials. In both cases, superconductivity manifests within specific planes ($CuO_2$ in cuprates and FeAs in iron-based superconductors). Additionally, they exhibit analogous phase diagrams, wherein superconductivity only arises subsequent to the introduction of electrons or holes into an antiferromagnetic parent state through doping [40].

However, significant distinctions between them emerge. In the case of cuprates, their parent compound takes on a distinctive identity as a Mott insulator special kind of anti-ferromagnet characterized by strongly correlated electrons. Conversely, in iron-based superconductors, the parent compound assumes the guise of an anti-ferromagnetic semi-metal. Notably, hole-doped cuprates exhibit a "pseudogap" state above $T_c$, a phenomenon conspicuously absent in iron-based superconductors. Furthermore, the symmetry of the pairing wavefunction in pnictides remains a subject of widespread debate, although an extended s-wave scenario currently holds favor.

The perplexing question of how superconductivity arises in HTS stands as one of the foremost unsolved challenges in theoretical condensed matter physics, why the electrons within these crystals form pairs remains an enigma yet to be unraveled.

## 1.2 YBCO cuprate HTS

$YBa_2Cu_3O_{7-\delta}$, or Yttrium Barium Copper Oxide (YBCO) [41], is a ceramic high-temperature superconductor known for its remarkable superconducting properties at relatively high temperatures and magnetic fields. Optimally doped YBCO presents an orthorhombic crystal structure forming a triple perovskite arrangement comprising $CuO_2$ planes oriented perpendicular to the c-axis [42, 43](Fig.1.12a).

The $CuO_2$ planes are where superconductivity occurs as they contain mobile charge carriers responsible for supercurrent flow. These $CuO_2$ planes, where supercurrents flow due to mobile charge carriers, are separated by charge-reservoir layers containing CuO chains, which regulate carrier density within the superconducting $CuO_2$ planes [38]. Optimally doped YBCO present a critical temperature ($T_c$) of approximately 92 K. This is considerably higher than the temperatures at which most conventional superconductors operate, making it suitable for practical applications where liquid nitrogen can be used as a coolant.

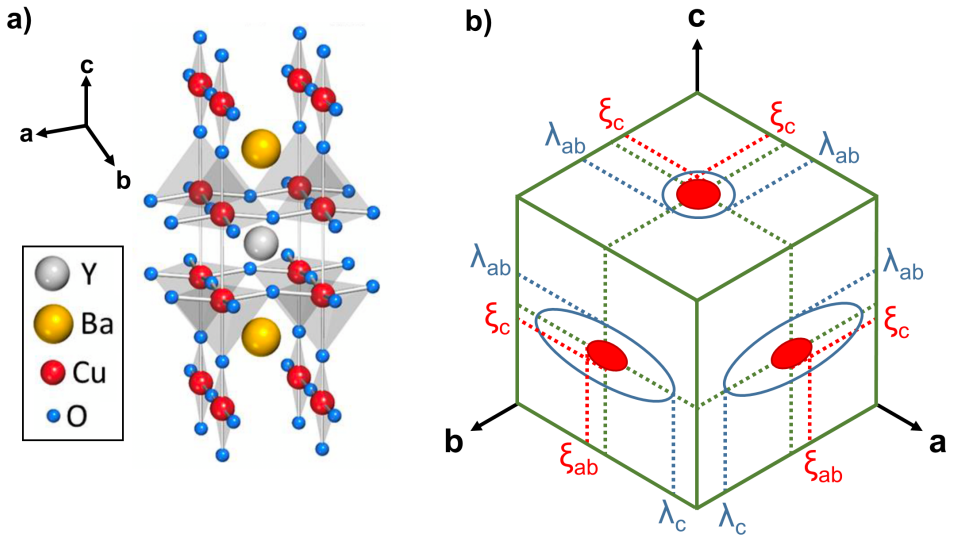



Figure 1.12: Sketches of a) crystal structure of $YBa_2Cu_3O_{7-\delta}$ (YBCO). In the SC state it has an orthorombic symmetry and two $CuO_2$ planes per primitive cell, with the oxygen atoms forming Cu-O chains along the b-axis [44]. b) $\xi$ and $\lambda$ for the different orientations of the magnetic field along the crystallographic axes.

$YBa_2Cu_3O_{7-\delta}$ superconducting properties are highly dependent on its oxygen content ($\delta$ value) where its control and optimization depends on the doping with different oxygen levels [43, 45]. While the anisotropy in YBCO is less pronounced compared to other cuprate superconductors, it still demonstrates superior conduction in the ab-plane, where carriers are predominantly situated within the $CuO_2$ planes, than along the c-axis. This anisotropy, arising from YBCO's layered structure, influences both the effective electron mass and the characteristic lengths of vortices $\lambda$ and $\xi$. Therefore, the nature of vortices undergoes alterations depending on the orientation of the mag-

netic field relative to the crystallographic axes. $\lambda_{ab}$ and $\lambda_c$ represent the penetration depths for supercurrents flowing parallel to the ab-plane and the c-axis. Concerning the coherence length, when the core is aligned parallel to the $CuO_2$ planes or along the c-axis, the radius of the vortex core is determined by $\xi_{ab}$ and $\xi_c$, respectively [46, 47] (Fig.1.12b).

The ratio between characteristic lengths at different orientations defines the vortex anisotropy parameter $\gamma$, which is also equivalent to the square root of the electronic mass anisotropy (Eq.1.16). This ratio remains constant with temperature, making gamma an intrinsic parameter unique to each material. In the case of YBCO $\gamma$ has a value ranging from 5 to 7 according to the literature [47–50].

$$\gamma = \sqrt{\frac{m_c}{m_{ab}}} = \frac{\xi_{ab}}{\xi_c} = \frac{\lambda_c}{\lambda_{ab}} \tag{1.16}$$

Various superconducting parameters such as the critical field ($H_c$) or critical current density ($J_c$) can be normalized into an isotropic contribution, in accordance with the Ginzburg-Landau approximation applicable to YBCO owing to its 3D behavior. As proposed by Blatter [51], this is achieved by employing the angular dependence of an anisotropic factor $\varepsilon(\theta)$. Taking into account that $\theta$ is the angle between the magnetic field and the crystallographic c-axis, then:

$$\varepsilon(\theta) = \sqrt{\frac{sin^2(\theta)}{\gamma^2} + cos^2(\theta)} \tag{1.17}$$

### 1.2.1 Vortex pinning

Diverse phases manifest in the mixed state of high-temperature superconductors arising from the interplay of vortex-vortex interactions, anisotropic behaviour, various forms of disorder and thermal fluctuations. The thermal energy surpasses the energy associated with vortex-vortex interactions at high temperatures, preventing the formation of a solid lattice. This results in a phase transition delineated by a melting line.

For homogeneous, pure crystals, this line represents a first-order thermodynamic transition, while for samples with significant disorder, it takes on second-order characteristics and delineated with the irreversibility line ($IL$). It serves as the demarcation between two regions: one where vortex matter exhibits solid-like behavior [52] and another where it behaves more like a liquid [53]. Despite the material maintaining a superconducting state between $IL$ and $H_{c2}(T)$ with $J_c \neq 0$, vortices cannot be pinned due to their elastic properties.

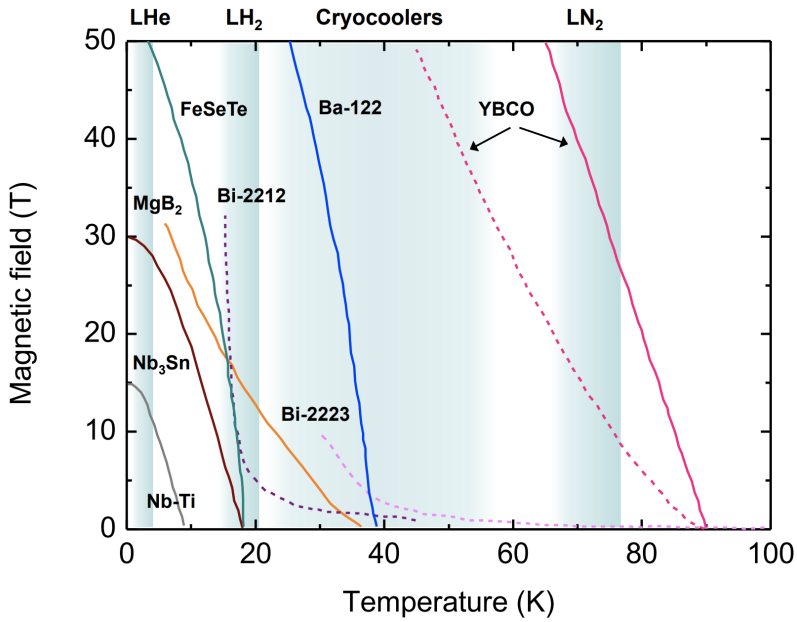



Figure 1.13: Comparative H-T phase diagram for different type of superconductors. The solid lines represent the upper critical field $H_{c2}$(T) and the dashed lines, the irreversibility line ($IL$) parallel to the c-axis. Graph extracted from [54].

Values of $IL$ and $H_{c2}$ for different type of superconductors are represented in Fig.1.13 [48, 55, 56]. YBCO (pink lines) stands out as the superconductor exhibiting one of the highest irreversibly line $IL$, making it the most promising candidate for technological applications. Moreover, The $IL$ can be heightened toward $H_{c2}$ by introducing defects into the system, i.e. increasing the pinning force.

As previously elucidated, in the phase diagram of a type II superconductor, we can observe a magnetically irreversible zero-resistance state known as vortex solid phase and a reversible state with dissipa-

tive transport properties called vortex liquid state. For the solid phase, multiple glassy vortex states have been proposed and a representation of the magnetic phase diagram is shown in Fig.1.14. For instance, in the case of YBCO, an array of disordered vortex solid states has been suggested, contingent upon the type and dimensionality of the defects.

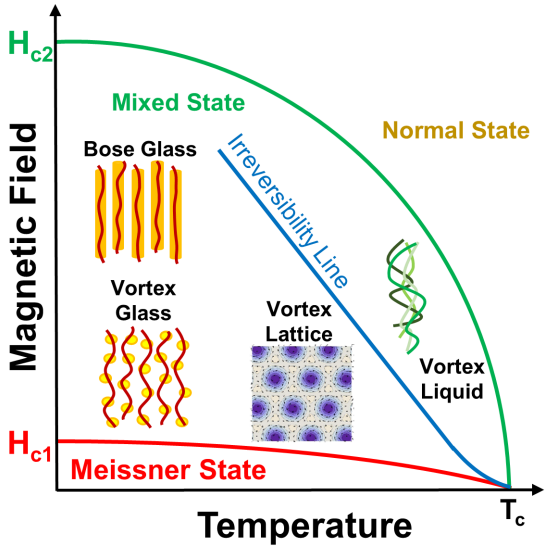



Figure 1.14: $H$ - $T$ phase diagram of vortex matter in YBCO, showing some of the proposed liquid and solid vortex phases and the transitions between them.

The presence of correlated disorder, such as 2D planar defects (twin boundaries), dimensional columnar defects and amorphous defects, is expected to result in a Bose glass phase [57–59]. In contrast, when subjected to isotropic weak random point disorder, such as oxygen vacancies, impurities or electron irradiation, a vortex glass phase is anticipated [60].

Any deviation from the regularity of the crystal lattice is recognized as a defect. Specifically, for laminar type-II superconductors like YBCO, it is crucial to distinguish defects that enhance superconducting performance through vortex pinning from those causing grain discontinuity and a reduction in percolation currents. Given the small vortex coherence length in YBCO (and high-temperature superconductors in general), numerous structural and atomic defects generated during growth can serve as potential pinning candidates.

However, it is essential to ensure complete current percolation and grain connectivity to harness the benefits of such contributions. The challenge lies in finding ways to control and selectively promote the desired type of defect. After years of investigation a range of defects has been identified in YBCO films, spanning from zero-dimensional (0D) to three-dimensional (3D), which are represented in Fig.1.15.

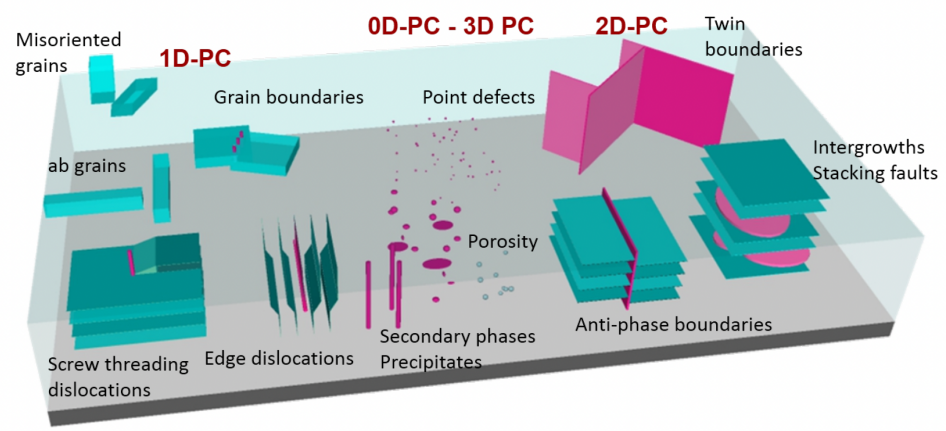



Figure 1.15: Schematic representation of different defects present in YBCO films and nanocomposites. The pink regions represent the nanosized regions able to act as pinning centres. The dimensionality of the pinning centres is also indicated [61].

Starting with 0D defects we have the point defects, that involve disruptions at the atomic scale, such as interstitials, impurity atoms, or the interchange of Y and Ba atomic sites [62, 63]. Examples of 1D defects include dislocations and column defects (nanorods) [64–70], while planar defects like stacking faults (SFs), twin boundaries (TBs) and antiphase boundaries disrupt the superconducting structure in 2D [71–79]. On the other hand, three-dimensional disruptions of the superconducting order parameter include nanoparticles, locally strained regions, porosity, and larger precipitates [80–85].

Both 1D and 2D defects act as anisotropic pinning centers, pinning vortices with angular-dependent forces. In contrast, 0D and 3D defects function as isotropic pinning centers contributing equally in all directions of the magnetic field. Isotropic and anisotropic pinning centers make distinct contributions to the final critical current density for different magnetic field orientations, corresponding to varying vortex orientations. Structural defects are classified into two categories:

natural defects and artificial pinning centers (APCs), depending on whether the defect occurs naturally during growth or is intentionally introduced through other techniques.

For instance, twin boundaries (TBs) and stacking faults (SFs) are natural defects typically arising from strain relaxation and the shift from a tetragonal to an orthorhombic crystal structure during oxygenation. The YBCO layered structure inherently exhibits intrinsic pinning along the ab-planes by confining vortices within these planes. To optimize superconducting performance in specific ranges of the high-temperature diagram and to make the material more isotropic, a lot of material science research has been conducted to generate APCs, obtaining nanostructured YBCO or nanocomposites (NCs) films. The final goal is to tune defect distribution, density and size in order to optimize the pinning landscape of defects and therefore the superconducting properties [61, 68, 86–91].

Vortex pinning depends on temperature, magnetic field intensity and orientation. Consequently, critical current density and other superconducting parameters, such as the pinning force ($F_P$), vary with these physical factors. Various theoretical models aim to elucidate the dependencies of $J_c$, with two distinct approaches proposed for the temperature dependence concerning the pinning strength of pinning centers: weak and strong. The method employed to distinguish between weak and strong pinning centers (PCs) relies on the distinct $J_c(T)$ dependencies exhibited by each contribution. The weak collective pinning model [11] characterizes the behavior of defects, leading to a rapid decay of $J_c(T)$:

$$J_c^{weak}(T) \sim J_{c0}^{wk} exp\left(-\frac{T}{T_0}\right) \tag{1.18}$$

$J_{c0}^{wk}$ represents the weak pinning contribution at 0 K, and $T_0$ is associated with the characteristic vortex pinning energy of weak defects, commonly observed in point defects such as oxygen vacancies with dimensions smaller than the coherence length. While the influence of weak pinning sites in YBCO films is prominent at low temperatures, the applicability of this model extends to temperatures up to 60 K and magnetic fields up to 6 T.

In contrast, the theory developed for vortex pinning in strongly correlated defects [58] predicts a slower $J_c(T)$ decay:

$$J_c^{strong}(T) \sim J_{c0}^{str} exp\left[-3\left(\frac{T}{T_0^*}\right)^2\right] \tag{1.19}$$

$J_{c0}^{str}$ signifies the strong pinning contribution at 0 K, and $T_0^*$ is the corresponding characteristic vortex pinning energy for strong pinning defects. This model successfully describes vortex dynamics in ion-irradiated cuprate superconductors [92] and the temperature dependence of critical current density in high-$T_c$ superconductors with strong pinning sites at intermediate and high temperatures [93, 94].

The contribution of 1D and 2D PCs aligns with this strong pinning schema. While the anisotropic contribution can be fitted using eq.1.19 for anisotropic correlated defects governed by strong correlated pinning, the isotropic contribution needs a combination of weak and strong pinning contributions for an accurate fit. Consequently, $J_c$ can be dissected into three distinct contributions ($J_c^{iso-wk}$, $J_c^{iso-str}$ and $J_c^{aniso-str}$), allowing analysis at different fields and temperatures to construct $H-T$ pinning phase diagrams indicating the relative weight of each contribution. Thus, their simultaneous contribution will be responsible of their final pinning performance [84, 87, 89].

### 1.2.2 Oxygen doping

Oxygen doping in $YBa_2Cu_3O_{7-\delta}$ is a common technique used to control and manipulate the superconducting properties of the material. It is well known that the carrier density (hole doping) can be tuned by the concentration of oxygen vacancies in the crystal lattice. The oxygen doping in YBCO thin films is typically controlled during the fabrication growth process by adjusting the oxygen partial pressure and annealing conditions. Some techniques involve post-processing, where the material is exposed to controlled oxygen atmospheres to achieve the desired doping level. This process is crucial in order to achieve good superconducting properties.

Cuprate superconductors, as strongly correlated materials, present an extremely rich phase diagram with various forms of quantum or-

dered phases, and collective fluctuations originated from the interplay of charge, spin, orbital, and lattice degrees of freedom[95] (Fig.1.16). The superconducting state (red region) occurs at intermediate hole doping and the critical temperature follows a dome-shape dependence where a maximum $T_c = 92K$ is obtained for the optimally doped compound ($p \approx 0.16$) [96, 97].

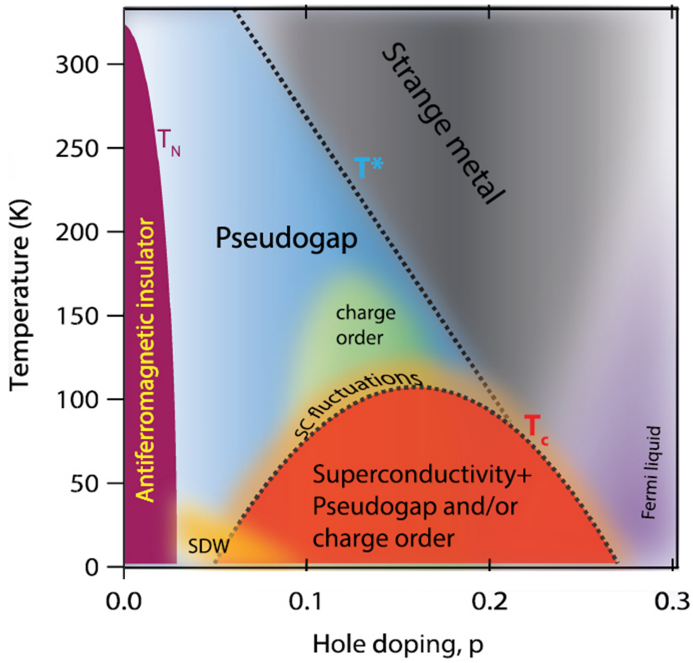



Figure 1.16: Schematic Temperature-doping phase diagram of cuprates from [98].

The region in the phase diagram with a doping less/higher than that of the maximum $T_c$ is the underdoped/overdoped region. At very low doping levels ($p < 0.03$) the material is antiferromagnetic insulator. Transitions between different phases, with dramatically different physical properties, may be induced through external perturbations such as temperature, pressure [99], strain, electric field [100–102] or light [103, 104].

Specifically, room temperature field-induced metal-insulator transitions (MITs) can be exploited to produce non-volatile reversible switching between different resistance states for memory and neuromorphic applications [105]. Various mechanisms are employed to produce field-induced resistive Switching (RS) effects in diverse materials. Examples

include manipulating the tunnelling current in a junction by altering the polarization direction of a ferroelectric domain [106], or the electrochemical metallization mechanism (ECM), where mobile cations create or dissolve a metallic filament as they traverse a solid electrolyte [107]. Among all of them, resistive switching devices, based on strongly correlated oxides, appear as very promising systems since large resistance variations may be induced by small carrier concentration modulations driven by an electric field, enabling the stabilization of non-volatile multilevel analogical states [108].

Although the underlying mechanisms behind the RS phenomena are complex and dependent on the specific materials involved, in oxide systems, the switching behaviour is often associated with the movement of oxygen vacancies [109]. This movement can manifest as a metallic filament embedded within an insulating matrix [109], modification of a Schottky barrier at the contact interface [110], or due to a oxygen vacancy modulation through the material volume [111–115] (see Fig.1.17). This last mechanism, allowing a volumetric RS effect, may be of interest for the design of three-terminal synaptic devices or multi-terminal memristors able to mimic complex neuromorphic functionalities [115].

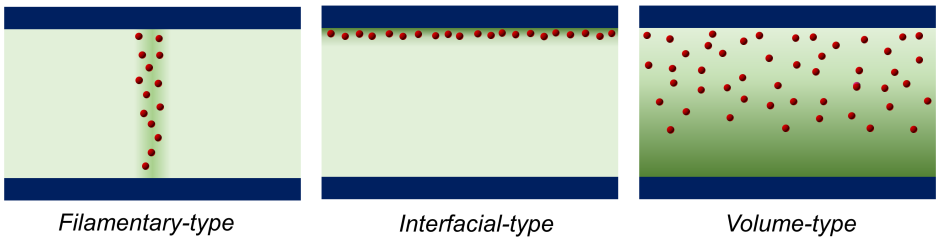



Figure 1.17: Different switching mechanisms for complex oxides.

Beside the restive switching effects induced at room temperature, field-induced hole doping in YBCO films may be used to modulate the superconducting properties of the material. In general this can be achieved by pure electrostatic carrier modulation or through oxygen doping. Electrostatic carrier doping refers to the modification of the carrier concentration in a material using an external electric field, typically through a ferroelectric polarization or by using a dielectric or electrolyte gating [116–122].

This electric field can induce a change in the charge carrier concentration within the YBCO material without introducing any chemical species, although ultra-thin superconducting layers and large electric fields must be used to observe significant carrier modulation (Fig.1.18).

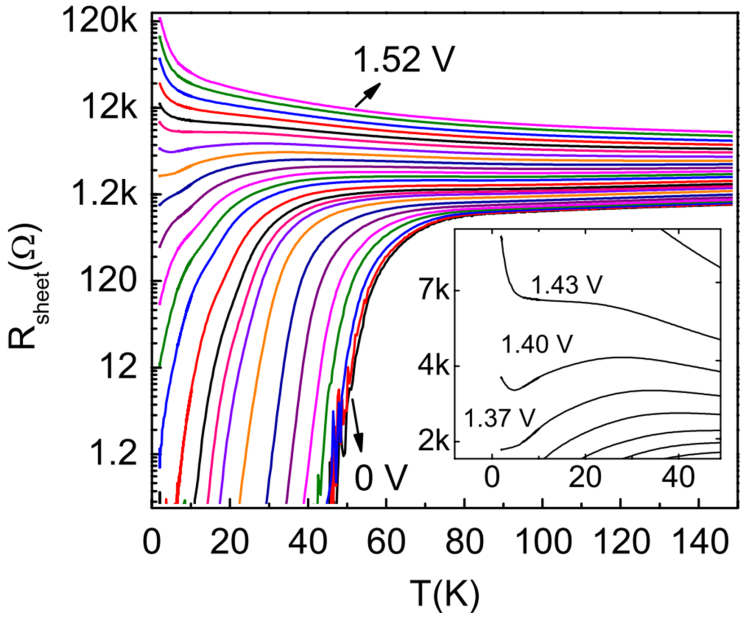



Figure 1.18: Electrostatic control of $T_c$ in ultrathin YBCO films (7 unit-cells) [119].

In the case of electrochemical doping, the carrier modulation is achieved though field-induced oxygen migration which may proliferate to extended regions (hundreds of microns) using moderate voltages (1 - 5 V) [61, 115]. In this way, the superconducting critical temperature can be reversibly manipulated in thicker YBCO films by driving the system from the superconductor to the insulating state [61] (Fig.1.19(a)).

An alternative and promising approach for precise tuning of the oxygen doping, and thus the critical temperature, within a single structure is the electromigration process where diffusion of oxygen atoms is obtained with an applied current [97, 123, 124] (Fig.1.19(b)).

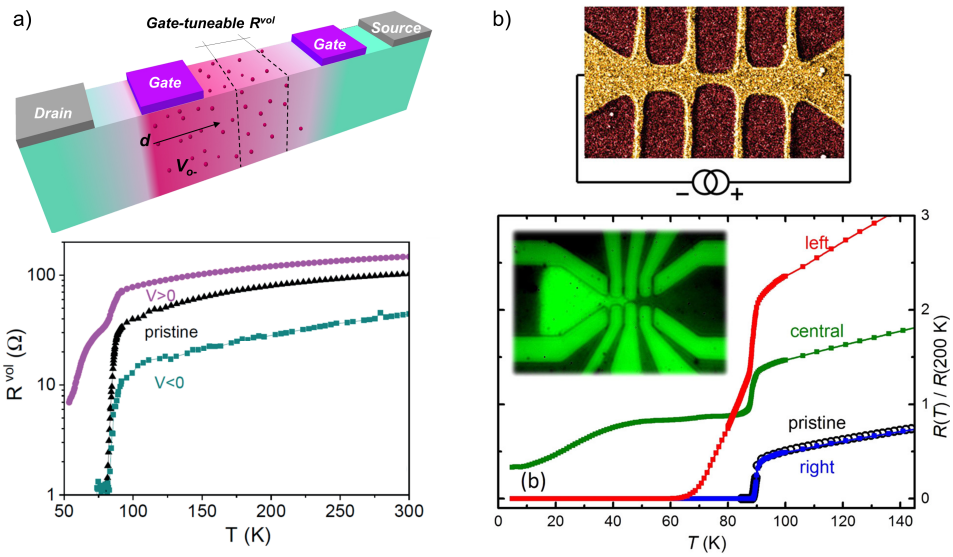



Figure 1.19: Modulation of $T_c$ in 100nm YBCO films through (a) Electric-field induced oxygen doping (b) Electric-current stimulated oxygen migration. Figure adapted from [123, 125].

# Chapter 2

# Experimental methodology

This chapter of the thesis will describe the experimental methodology employed in the research work. Consequently, it will provide a detailed explanation of the growth of the analyzed samples, the patterning using micro -and nano-lithography processes, the procedure to use various structural and physical characterization techniques, and ultimately, the procedure for conducting electrical transport measurements.

## 2.1 YBCO Thin film growth

Throughout the entire study, our focus has been on YBCO thin films, which we fabricate through two distinct processes. Samples described in Chapter 3 were grown using Chemical Solution Deposition (CSD), involving Ba-deficient solutions. Conversely, the samples detailed in Chapters 4 and 5 were grown by using Pulsed Laser Deposition (PLD).

### 2.1.1 Substrates

To obtain the samples, the initial step involves acquiring the substrates. Since we are working with YBCO as the material, it is essential to select a substrate with a closely matching structure for achieving proper epitaxy. The predominant choice for growing the majority of samples has been lanthanum aluminate $LaAlO_3$ (LAO) as the substrate. This is a ceramic oxide characterized by optical transparency and a distorted perovskite structure. However, in some alternative samples, strontium titanate $SrTiO_3$ (STO) has been employed as the substrate having also the perovskite structure.

Both LAO and STO were obtained from Crystec (Germany) and the dimensions were $5 \times 5 \times 0.5$ mm with orientation (001). Before the material deposition they have to be cleaned with acetone and methanol in order to eliminate some dust or possible adsorbents. Afterwards, a thermal treatment is performed, consisting on putting the substrates in an alumina ceramic crucible inside of a quartz tube placed in a furnace. A constant $O_2$ flux of 0.5 L/min, a heating ramp of 15 °C/min until reaching 900 °C, 5 hours dwell time and a cooling ramp of 10 °C/min until room temperature, were used.

### 2.1.2 Chemical Solution Deposition (CSD)

Chemical Solution Deposition is a multi-step deposition technique used for the fabrication of thin films and coatings (particularly for complex materials like ceramics and semiconductors) that is characterized by its simplicity, scalability, versatility and low cost. The process involves the deposition of precursor solutions onto a substrate, followed by controlled thermal treatments to convert the precursors into the desired film or coating. CSD is advantageous for producing thin films with a high level of compositional control and uniformity. It is commonly used in the fabrication of materials like superconductors [126], ferroelectrics [127], and other advanced electronic and optical materials with great success in the epitaxial thin film growth [128–130].

The synthesis of the solutions used in this work are made with a deficiency in the Barium salt by changing the proportions of the reagents to 1:1.5:3 for Y:Ba:Cu salts, respectively and using the low-flourine TFA route. In this chapter we will describe how this type of solutions are prepared and more details on the selection of particular solution and growh conditions will be given in Chapter 3. It is also worth noting that the solutions have been developed following the large background already existing in the group on the subject [131]

#### 2.1.2.1 Solution synthesis

The starting solutions are prepared by dissolving barium and copper acetates, and yttrium trifluoroacetate (low-F) with the ratio of Y/Ba/Cu equal to 1:1.5:3 (Ba-deficient) in a mixture of organic solvents consisting of propionic acid (30 %) and methanol while heating at 30 °C. The choice of short chain carboxylates, such as acetates and

trifluoroacetates, is due to their decomposition behavior, which has been widely studied [132]. The choice of the solvent is based on previous studies performed on YBCO samples grown with TFA solutions [131]. It is important to note, however, that having an alcohol and a carboxylic acid in the reaction mixture favors the formation of water by means of an esterification reaction, which may have a detrimental effect on its superconducting performance [133].

Thus, the solvents are smoothly evaporated until constant weight (approximately 2.5 hours) in a vacuum rotary evaporator at 131 mbar and with a bath temperature of 70 °C to ensure a water content less than 0.6 %. The gelatinous textures obtained are dissolved in small amounts of methanol and homogenized by stirring for 24 h. Afterwards, the solutions are brought to the desired concentration (1.5 M) with additional methanol and filtered through 0.22 $\mu$m filters to avoid impurities and guarantee homogeneity in the final solutions.

#### 2.1.2.2 Deposition

Considering the rheological characteristics of the precursor solutions, including wettability, viscosity, and solvent evaporation rate, the chosen deposition technique is spin coating. This method allows for the efficient and rapid creation of uniform thin films. Minimizing water content in the precursor solution is crucial for achieving highly epitaxial superconducting films. Consequently, depositions take place in laboratories with controlled atmospheric conditions, ensuring that humidity is consistently maintained below 10 %.

Both the spinner and the substrate undergo meticulous cleaning with methanol to ensure the absence of dust or external impurities in the deposition area, as their presence could result in the production of low-quality films. Subsequently, the cleanliness of the substrate is examined through an optical microscope, and if necessary, the substrate is re-washed. Before commencing the deposition, a nitrogen flow is introduced into the spinner cavity to establish a low-humidity environment and the substrate is positioned at the center of the spinner's circular platform. Following this, 20 $\mu$L of the working solution is drawn using a Hamilton syringe and dropped onto the substrate's center. The spinning process is initiated to achieve a uniform distribution of the solution on the substrate. Various parameters govern

this step, including angular acceleration (6000 rpm/s), angular velocity (6000 rpm), and spinning duration time (2 min), which are optimized for YBCO precursor solutions. Once the spinning concludes, the substrate is placed over a crucible on a hot plate (Fig.2.1) set at 70 °C to aid solvent evaporation and achieving a monolayer. Minimizing solvent presence ensures a homogeneous mixture over time by preventing liquid movements.

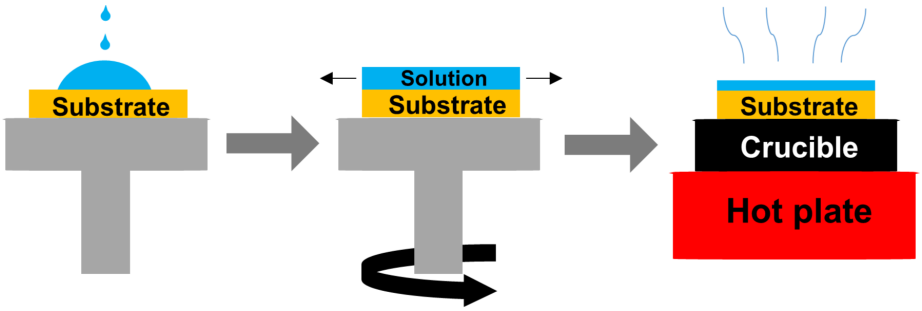



Figure 2.1: Skecth of the spin coating process consisting on three steps: deposition, spinning and evaporation. Grey piece represents the sample holder in the spinner.

#### 2.1.2.3 Pyrolysis

The initial thermal treatment is referred to as pyrolysis, involving the decomposition of all organic compounds within the sample to create the necessary precursors for the growth stage. Pyrolysis occurs in a tubular furnace under a humid oxygen atmosphere. The optimized pyrolysis process comprises distinct stages programmed into the furnace (Fig.2.2). Initially, the sample is placed in the furnace, setting a constant flow of 120 mL/min of $O_2$, and initiating the program.

The furnace undergoes two warm-up ramps. First, the system is heated to 240 °C at a constant rate of 5 °C/min. Humidification of the atmosphere occurs when the temperature surpasses 110 °C to prevent copper salt sublimation. It is crucial not to initiate humidification before 100 °C to avoid water vapor condensing on the sample, which could lead to cracks and inhomogeneities. Subsequently, the furnace is raised to 310 °C at 3 °C/min, maintaining this temperature for half an hour. Finally, the furnace is cooled down to room temperature at a rate of 15 °C/min.

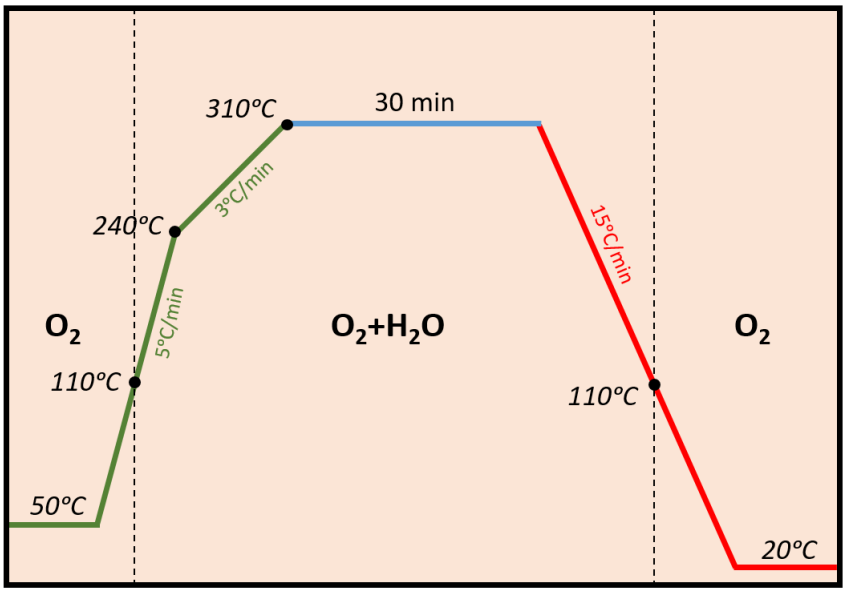



Figure 2.2: Pyrolysis treatment profile.

Throughout the heating ramps, the organic components of the sample undergo decomposition. Methanol and residual propionic acid, not completely evaporated in the rotavapor due to their boiling temperatures of 64.7 °C and 141.2 °C, respectively, are eliminated. Elevated temperatures are attained to facilitate the decomposition of propionates ($\approx$ 300 °C). The deliberate use of slow heating ramps aims to prevent the formation of any morphological or compositional irregularities in the film, which undergoes a substantial shrinkage process during this calcination step.

During the dwell period, decomposition occurs through low-fluorine mechanisms [134]. The C-F bonds of the TFA are cleaved, generating F anions or radicals that subsequently react with the $Ba^{2+}$ ions present in the mixture: $F^- + Ba^{2+} \rightarrow BaF_2$. $Cu^{2+}$ and $Y^{3+}$ ions instead are recombined forming oxides and the general pyrolysis reaction would be: $Ba(Prop)_2 + Cu(Prop)_2 + Y(TFA)_3 \xrightarrow{O_2} CuO + BaF_2 + Y_2O_3 +$ volatile compounds. Then the calcination process generates a homogeneous nanocrystalline film formed by CuO, $Y_2O_3$ and $BaF_2$, which are the precursors of the growth step.

#### 2.1.2.4 Growth and oxygenation

The second thermal treatment is conducted in tubular furnaces and is divided into two phases: the growth process and the oxygenation process. During the growth process, the sample is subjected to high temperatures (700 °C - 810 °C) in a humid mixture of nitrogen (an inert gas) and oxygen atmosphere. The growth mechanism remains a topic of debate [126]. One proposed mechanism suggests a reaction between precursor oxides, followed by the intermediate formed reacting with the remaining precursors (from the pyrolysis step) and water vapor to create YBCO nuclei. Epitaxial YBCO nucleation at the substrate interface (with the c-axis perpendicular to the substrate) is ensured. Extended periods at the growth temperature are employed to promote the sintering process, facilitating the formation of YBCO layers.

The growth treatment involves two distinct methods. The first method is the Conventional Thermal Annealing (CTA), established as the standard for synthesizing YBCO layers [135]. This method is extensively optimized to consistently yield the desired compounds. The second method is the Flash Heating (FH), a novel treatment currently under investigation for YBCO layer synthesis through a very fast procedure [136–138]. This method has been obtimized during this work.

Upon the formation of the YBCO phase, an oxygenation process is initiated. The underlying concept of this procedure is to transform an insulating structure, specifically tetragonal YBCO ($YBa_2Cu_3O_{7-\delta}$ with $\delta \approx 1$), into a superconductive one, with orthorhombic YBCO structure ($YBa_2Cu_3O_{7-\delta}$ with $\delta \approx 0$), as commented in the introduction. This transformation occurs by placing the sample in a dry oxygen atmosphere, leading to the occupation of oxygen vacancies in the YBCO structure.

The CTA method involves a carefully defined temperature profile programmed into the furnace (Fig.2.3), starting from room temperature. Initially, the sample is introduced into the system, setting a flow of 1.2 L/min of nitrogen and 0.24 mL/min of oxygen, and initiating the program. The furnace is then heated to the growth temperature range (730 °C - 810 °C) at a constant rate of 25 °C/min. A wet atmosphere is established when the temperature exceeds 110 °C, necessary for decomposing the $BaF_2$ precursor at higher temperatures. Control-

ling humidity conditions is crucial to prevent water vapor condensation on the sample.

The program maintains the growth temperature for 180 minutes. After 150 minutes of the dwell, water vapor is deactivated, and the atmosphere returns to a dry state. With YBCO nuclei already formed and grown, the sintering process commences. The system is then cooled to 600 °C at a rate of 2.5 °C/min, marking the completion of the growth phase and the initiation of oxygenation. A flow of 0.3 L/min of dry oxygen is introduced. The furnace is brought to 450 °C at 1.3 °C/min, maintaining this temperature for 210 minutes to optimize oxygenation. Subsequently, the system is cooled to room temperature at a rate of 2.5 °C/min.

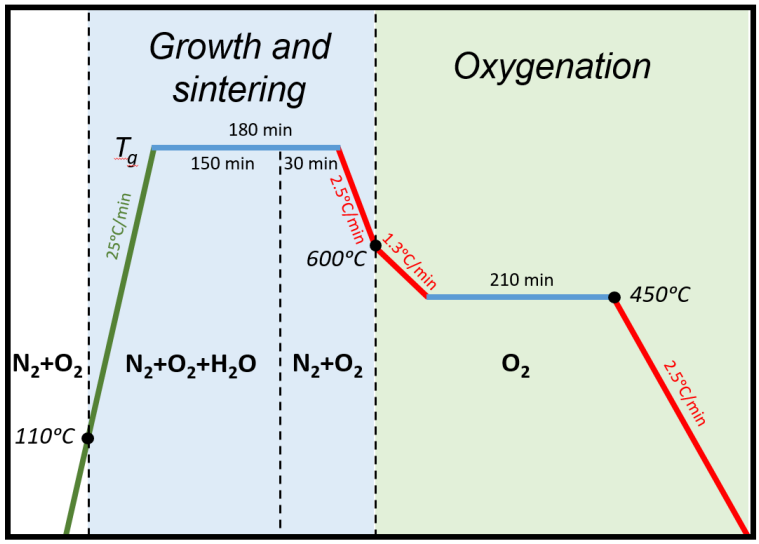



Figure 2.3: Conventional Thermal Annealing method profile.

The FH method involves distinct stages programmed into the furnace, commencing from the growth temperature. Initially, the furnace is heated to the growth temperature range (700 °C - 750 °C), setting a flow of 0.6 L/min of nitrogen and 0.12 mL/min of oxygen, and allowing the system to equilibrate for half an hour. Subsequently, the sample is introduced at the furnace entrance and remains there for 1 minute, a duration believed to be sufficient for the sample to reach a temperature of approximately 110 °C.

After this period, a wet atmosphere is established, and the sample spends another minute at the furnace entrance. Following this, the sample is placed inside the furnace. In FH, the nucleation and growth of YBCO are significantly faster than in CTA due to the high temperature gradient. At this stage, the temperature profile mirrors that of the CTA method. Once the growth phase concludes, a flow of 0.6 L/min of oxygen is introduced, marking the initiation of the oxygenation process.

### 2.1.3 Pulsed Laser Deposition (PLD)

PLD technique is very suitable for growing oxides, and compared with other techniques is particularly useful to obtain films with complex stoichiometry and to grow epitaxial films and heterostructures. Moreover, PLD is highly versatile to optimize the deposition conditions of new materials, and the films can be grown in relatively fast processes.

The application of the PLD technique for YBCO thin film growth has undergone nearly three decades of study [139, 140], demonstrating successful results in scaling the process for the production of kilometric second-generation HTS-coated conductors [141, 142]. Additionally, research has been conducted to enhance vortex pinning, offering potential benefits for specific applications [65, 66, 89].

The pulsed beam of an ultraviolet laser (usually an excimer) is focused on a ceramic target placed in a vacuum chamber. The combination of pulsed irradiation, high photon energy, and high energy density can cause the ablation (etching and emission of material under conditions totally out of the equilibrium) of the material. The plasma created expands fast along the perpendicular direction of the target (see the sketch in Fig.2.4a). A substrate is placed in front the target, and inert or reactive gases are usually introduced during the deposition process. The prepared substrate, previously arranged, is positioned precisely in front of the ceramic YBCO target within a vacuum chamber, maintaining a distance of 52.5 mm. To ensure phase stability, the substrate undergoes heating up to 800 °C in a partial pressure of 0.3 mbar of oxygen. This ambient gas serves a dual purpose by not only ensuring phase stability but also reducing the kinetic energy of the plume particles, facilitating a proper deposition process.

A UV window allows the laser beam to enter the chamber, and a lens focuses it onto the YBCO target, creating a spot area ranging from 1 to 2 $mm^2$. The laser's energy is calibrated to achieve a fluence of 2 $J/cm^2$. The laser operates at a frequency of 5 Hz, and the number of pulses depends on the desired thickness. Based on a prior calibration, a linear relationship of 26 pulses per nanometer is established, applicable to thicknesses within the range of 10 to 250 nm.

Upon completion of the growth process, a cooling ramp is initiated, bringing the temperature down from 800 °C to 600 °C at a rate of 15 °/min. This cooling is performed under a partial pressure of 400 mbar of oxygen, promoting the incorporation of oxygen into the YBCO and yielding well-oxygenated, optimally-doped samples. Subsequently, the sample undergoes direct cooling from 600 °C to room temperature under ambient pressure. Utilizing this method, we successfully generated samples ranging from 10 nm to 250 nm, exhibiting favorable physical properties. The growth of these samples was carried out by the skilled technicians at the PLD facilities within the Thin Film Laboratory at ICMAB (Fig.2.4b).

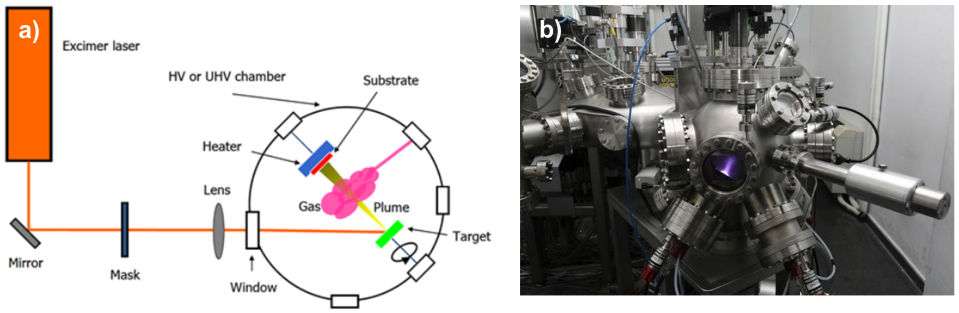



Figure 2.4: a) PLD system in the Thin Film Laboratory at ICMAB and b) sketch of the PLD setup. Both images extracted from Thin Film Laboratory web page.

## 2.2 YBCO thin film characterization

Following the growth of the YBCO films and prior to initiating the microfabrication process for measuring electrical properties, the films undergo a basic characterization to ascertain the composition, crystal orientation, morphology, and superconducting properties, using non-invasive techniques such as X-ray diffraction, dc-magnetometry

or Scanning Electron Microscopy (SEM). Once the samples are patterned, bridge thicknesses are presently assessed using profilometry or Atomic Force Microscopy (AFM) to ensure precision in calculating the critical current density $J_c$.

### 2.2.1 X-ray diffraction

The XRD characterization technique is widely employed to identify the crystalline structure and orientation of samples through the diffraction of X-ray radiation. The X-ray wavelength falls within the same order of magnitude as the interatomic distances present in the crystal structures investigated, typically ranging between 0.1 and 100 Å. The incident radiation interacts with the electrons within the atoms of the structure, leading to scattering. Constructive interference occurs when the optical path difference between the reflected beams equals an integer multiple of the wavelength, satisfying the Bragg condition [143]:

$$n\lambda = 2dsin\theta \tag{2.1}$$

where $d$ is the distance between crystal planes, $\lambda$ the wavelength of the incident light and $n$ is the diffraction order.

The measurements on the samples studied in this thesis were performed by technicians of the X-ray Diffraction Laboratory at ICMAB, using a 2D-XRD Bruker D8 Advance General Area Detector Diffraction System (GADDS), diffractometer operating with $CuK_\alpha$ (Fig.2.5a). This unit is equipped with a centric Eulerian cradle and a VANTEC - 500 area detector, giving the capability to handle tasks such as phase identification and quantification, textural and residual stress analysis, determination of particle size, percent crystallinity, and structural identification.

While performing those measurements, technicians used a $\theta$ - $2\theta$ configuration (Fig.2.5b), an angle step of 0.02 ° from 10 ° to 80 ° and a $CuK_\alpha$ radiation tube with $\lambda = 1.54056$ Å. Measurements yield a 2D pattern that represents $\chi$ (scattering angle on the y-axis) in relation to $2\theta$ (Fig.2.6a). Subsequently, using GADDS software, $\chi$ is integrated over a specified $2\theta$ interval (typically and in our case from 20 ° to 50 °), resulting in a graph depicting signal intensity as a function of $2\theta$ (Fig.2.6b).

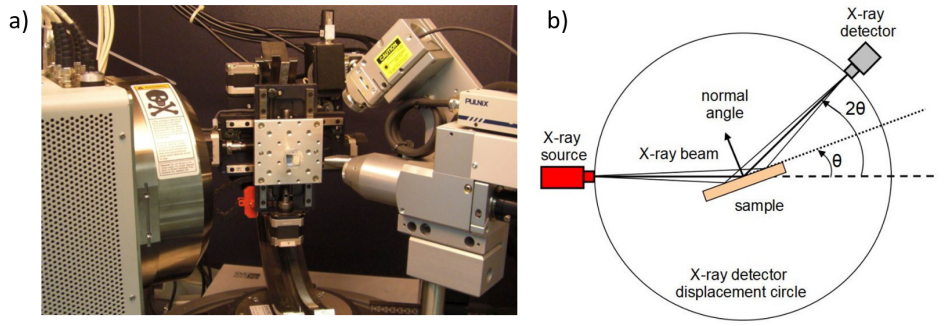



Figure 2.5: a) Bruker D8 Advance (GADDS) and b) sketch illustrating the configuration of the XRD measurements adapted from [144].

The identification of YBCO phases is accomplished by comparing them with their tabulated $2\theta$ values. Consequently, the crystalline structure and orientation of the layers become apparent. In the 2D pattern, monocrystalline (epitaxial) samples manifest spots, indicating that diffracted waves have discrete directions, whereas polycrystalline samples display rings, signifying diffracted waves with multiple directions. In YBCO layers, the presence of a YBCO (103) peak is indicative of poor growth and, consequently, a non-epitaxial sample.

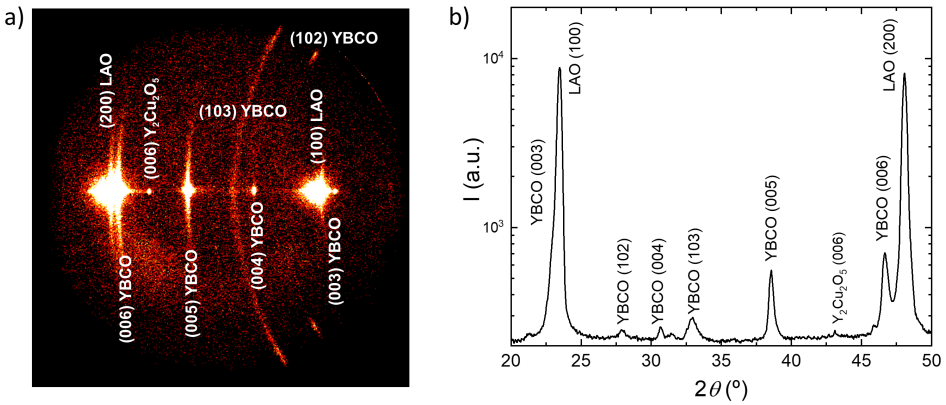



Figure 2.6: Polycrystalline sample analysis showing the a) $\chi$ vs $2\theta$ diffraction patterns and b) intensity vs $2\theta$ diffraction graph.

For samples grown by PLD, their composition is contingent upon both the target composition and the growth conditions. Given the standardized nature of the growth process and the consistent use of the same target, there is no necessity to verify the composition of

each individual sample, as the expected results have consistently been achieved. Conversely, for samples grown by CSD, their composition is influenced by the solution's stoichiometry, so a X-ray diffraction measurement was conducted each time the solution underwent a change.

### 2.2.2 SQUID dc-magnetometry

To characterize the supercondcuting performance of YBCO films before patterning, magnetic measurements were performed by technicians of The Low Temperature and Magnetometry Service in ICMAB. Two magnetometers were used: Quantum Design MPMS-XL and Quantum Design MPMS-3 (Fig.2.7). The first one is a magnetometer based on a SQUID detector that can determine extremely low magnetization signals present in the material under study. This magnetization can be evaluated under several conditions of external magnetic field and temperature.

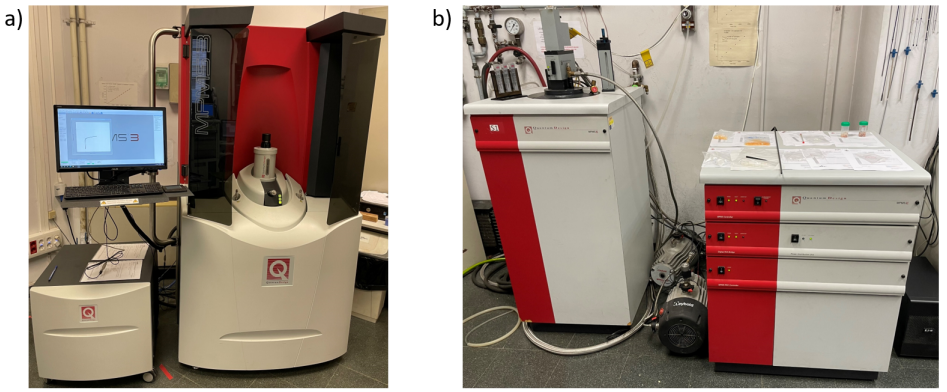



Figure 2.7: SQUIDs in the Low Temperature and Magnetometry Laboratory at ICMAB: a) Quantum Design MPMS-3 and b) Quantum Design MPMS-XL.

The second one offers an enhanced performance of temperature stabilization, magnetic field stability when compared to those exhibited by the MPMS-XL system. This fact reduces the measurement noise, allowing cleaner measurements for those samples with extremely low magnetic moment. In both magnetometers, the core system consists of a superconducting longitudinal solenoid able to generate magnetic fields up to 7 T. The system is also able to precisely control the temperature at the sample space at any value from 2 K to 400 K with a stability condition of less than 0.1% of oscillation.

Inductive magnetic measurements are conducted using the mentioned SQUIDs, allowing for the examination of the electromagnetic response of YBCO superconducting films. The sample is positioned with the c-axis aligned parallel to the applied magnetic field, and the operational temperature range is limited to the region where superconductivity occurs ($< 93$ K). Two types of measurements are executed.

In the first measurement called Zero Field Cooling (ZFC), a low and constant magnetic field (0.2 mT) is applied to the sample at 5 K after cooling from room temperature with no applied magnetic field, generating a specific magnetic moment ($m$). This moment arises from the induced shielding magnetic field produced by the superconductor, which opposes the external magnetic field. Subsequently, the temperature is gradually increased, and the values of $m(T)$ are recorded. Fig.2.8 shows an example of the acquired data, represented as $-m/|m_0|$, where $m_0$ is the value of $m$ at 5K.

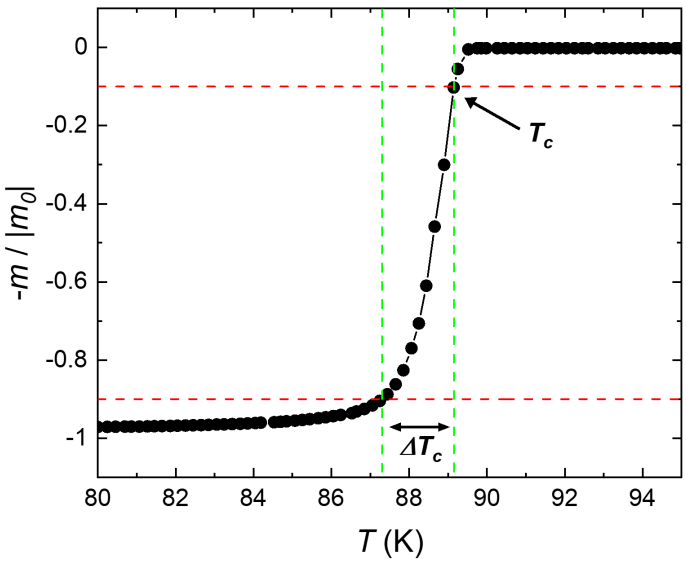



Figure 2.8: Magnetization measurements: $-m/|m_0|$ as a function of temperature obtained for a representative YBCO film used to determine $T_c$ and $\Delta T_c$.

The transition from the Meissner state to the normal state is observed, and subsequently, the on-set critical temperature ($T_c$) is determined, using a criterion of $-m/|m_0|$ = - 0.1. The experimental value obtained for the sample shown in the figure is $T_c = 89.15$ K. Additionally, the sample's homogeneity is assessed using the $\Delta T_c$ parameter,

defined as the difference between $-m/|m_0|$ = - 0.1 and $-m/|m_0|$ = -0.9. A small $\Delta T_c$ value indicates a uniform sample with a sharp transition and a well-defined $T_c$. High-quality samples typically exhibit $\Delta T_c$ values below 3 K.

The second measurement (Field Cooling, FC) involves applying a high magnetic field (3 T) to the sample at hight temperature and then cool down to 5 K to introduce vortices into the material. These trapped vortices generate magnetization, dependent on the applied field, resulting in the formation of a hysteresis loop. Subsequently, the magnetic field is gradually removed in multiple steps. The values of $m(H)$ are then used to calculate $J_c(H)$ using Bean's critical state model [21] through equation 1.14. Fig2.9a illustrates the critical current density as a function of the applied field, obtained for a standard YBCO film. In a similar way, one can determine the critical current density as a function of the temperature (Fig.2.9b), by gradually increasing the temperature at the remanent state.

For the samples grown by PLD, analyzed in chapters 4 and 5, $J_c$ was calculated using the formula of a disk with a diameter equal to the sample size with eq.2.2.

$$J_c(H) = \frac{3\Delta M(H)}{2R} = \frac{6|M(H)|}{a} = \frac{6|m(H)|}{aV} = \frac{6|m(H)|}{a^3 t} \tag{2.2}$$

where $t$ is the sample thickness, $a = 2R$ the side length, and considering $\Delta M(H) = 2|M(H)| = 2|m(H)|/V$.

For the samples grown by CSD (Chapter 3), we used a correction to compensate that the precursor solution is not uniformly distributed in the corners as it is in the center of the sample. This correction has been previously optimized in the group to match the inductive critical current density with the one obtained through transport measurements. In this case we used the following equation using a corrected radius ($R$) of 2.57 mm.

$$J_c(H) = \frac{3\Delta M(H)}{2R} = \frac{3|M(H)|}{R} = \frac{3|m(H)|}{VR} = \frac{3|m(H)|}{\pi R^3 t} \tag{2.3}$$

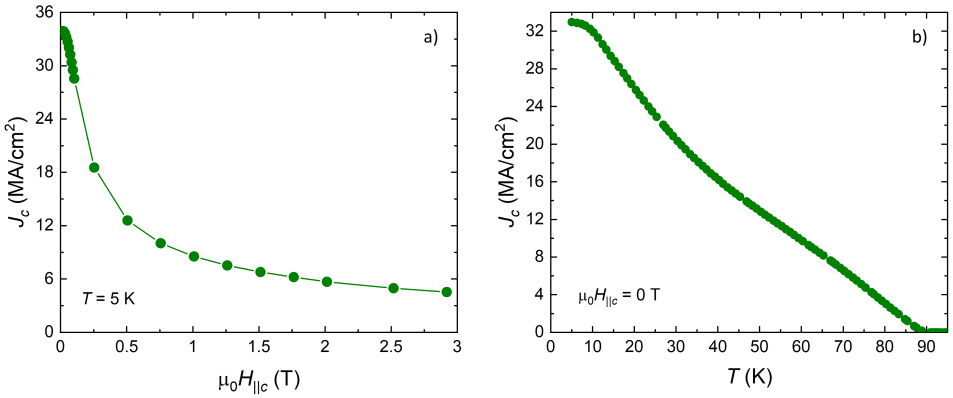



Figure 2.9: Critical current density as a function of the a) magnetic field at 5K, b) temperature. Both graphs extracted from Fieed Cooling measurements in a 200 nm CSD YBCO film.

### 2.2.3 Profilometer

With the intention of properly calculating the critical current density, it is important to know the thickness of our samples. To do so, we used a Profilometer measuring a track in lithographed samples.

We used a Profilometer P16+ from KLA Tencor, located in the cleanroom facilities in ICMAB (Fig.2.10a). The P-16+ stylus profiler is a surface metrology analysis solution that provides excellent vertical resolution, precision, and reliability measurements. This surface analysis solution delivers automated step height analysis, surface contour, waviness and roughness measurements with detailed 2D or 3D analysis of topography for a variety of surfaces and materials.

The machine is equipped with a diamond tip that remains in contact with the sample throughout the entire scan. Despite the expectation that this force should not impact the bridges of our devices, profilometry scans were performed after completing all the necessary experiments as a precautionary measure against potential damage. Typically, multiple scans at various points along the same bridge were conducted to enhance statistical reliability. The scanning procedure is designed such that the tip initiates the scan in an etched part, moves perpendicularly to the bridge, traverses it, and then descends to the etched part on the opposite side of the bridge (Fig.2.10b).

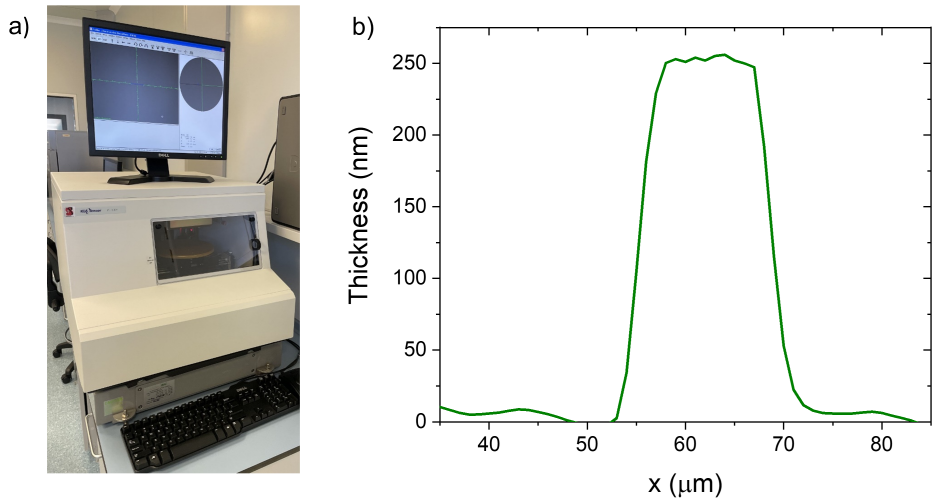



Figure 2.10: a) Profilometer P16+ from KLA Tencor located in the ICMAB cleanroom and b) surface profile of a 250 nm thick and 20 $\mu$m wide YBCO bridge.

### 2.2.4 Atomic Force Microscopy

Atomic Force Microscope (AFM) was used as another tool for measuring the thickness of our samples, particularly for smaller geometries due to its superior precision. Additionally, the AFM provided insights into defects and roughness without causing any damage to the sample, given its non-invasive nature. To ensure statistical accuracy, multiple measurements were conducted in the same area (or bridge), and other regions were examined to validate the consistency of values. In Fig.2.11, the AFM used is depicted along with an example of a 2D scan image obtained for a sample patterned with small triangles, including the profile of the sample along the pattern structures used to obtain the sample thickness.

Moreover, samples studied in Chapter 5 were analyzed with Conductive Atomic Force Microscopy (CAFM), located in Polifab, Politecnico di Milano. It functions similarly to a standard AFM but also captures the current passing through the tip-sample interface when a voltage is applied between the tip and the sample holder while in contact with the surface [145]. Contrary to a typical AFM setup, CAFM requires a conductive tip, as well as a voltage source and preamplifier to convert the analog current signal into digital voltages readable by a computer.

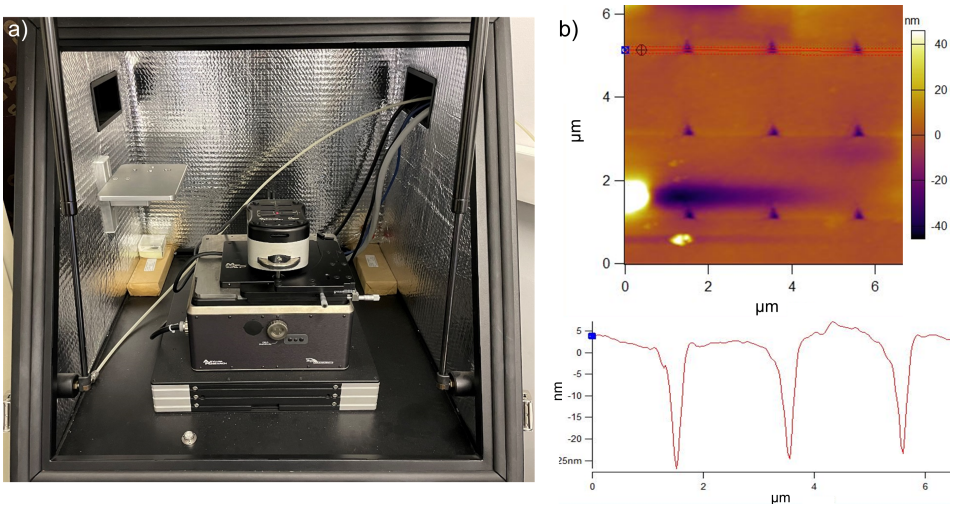



Figure 2.11: a) Atomic Force Microscope used in ICMAB and b) scanned image of a sample with triangle holes in the AFM with their thickness profile.

### 2.2.5 Scanning Electron Microscopy

For structural sample inspection we used a Scanning Electron Microscope (SEM), QUANTA FEI 200 FEG-ESEM, allowing to determine the sample morphology (Fig.2.12a). The microscope is equipped with a field emission gun (FEG) for optimal spatial resolution.

The instrument can be used in high vacuum mode (HV), low-vacuum mode (LV) (water vapour injection), and environmental SEM mode (ESEM). Moreover, the microscope is equipped with an Energy Dispersive X-ray system (EDX) for chemical analysis. Image contrast proportional to the atomic number is also available using an electron back-scattered detector.

The conventional Scanning Electron Microscope (SEM) stands out as one of the most valuable electron optical systems for surface imaging. In the samples studied in Chapter 3 (with CSD), the SEM characterization technique is routinely employed to assess the morphology, including porosity and crystallinity, of the surface of YBCO films grown under different conditions. A series of images at various magnifications (from 500× to 60000×) were acquired.

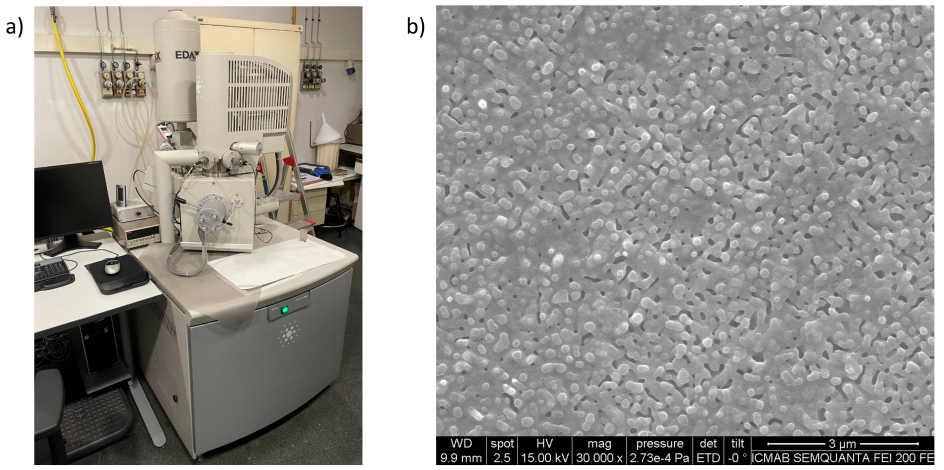



Figure 2.12: a) Scanning Electron Microscope used at ICMAB b) SEM image of a typical YBCO sample.

### 2.2.6 Scanning Transmission Electron Microscopy

In some specific cases, Transmission Electron Microscopy (TEM) was used to analyze the cross section of the films. In particular, we used this technique to characterize some of the samples described in Chapter 3, through a collaboration with Alexander Meledin (Julich, Germany). In this case, High-angle annular dark-field (HAADF) images were obtained with a FEI Titan ChemiSTEM probe Cs-corrected TEM operated at 200 kV [146].

For samples described in chapter 4, aberration-corrected STEM images were adquired using a JEOL JEM ARM200cF operated at 200 kV, equipped with a CEOS aberration corrector and GIF Quantum ER spectrometer, located at Universidad Complutense de Madrid, Spain, in collaboration with Jaume Gazquez and Mariona Cabero.

The STEM images were acquired in high angle annular dark field imaging mode, also referred to as Z-contrast because the brightness associated to each atomic column roughly scales with the square of the atomic number Z [147]. The STEM specimens were prepared using a FEI Helios nanolab 650, at SEM FIB microscopy service of the Universidad de Málaga, Spain.

## 2.3 Micro & Nano-fabrication

YBCO thin films grown by CSD or PLD were patterned in form of different structures which where used to study their superconducting performance. This section will outline these processes in a step-by-step manner. While not all samples follow identical preparation methods, we will provide a general description and specify any differing characteristics. Photo-lithography is the most used technique, although for certain cases, electron beam lithography and thermal scanning probe lithography were also employed.

### 2.3.1 Photolithography

As it was mentioned, after the growth of YBCO and its subsequent morphological and magnetic characterization, the samples were patterned using optical lithography process. The method involves copying a pre-established design from a photo-mask onto a light-reactive substance known as a photoresist on the base material. When exposed to illumination, the photoresist undergoes a chemical modification, permitting the selective elimination or preservation of material during subsequent processing phases.

So, in general the process starts when a thin layer of photoresist is applied by spin coating (1 in Fig.2.13) to the substrate. After that the photo-mask, containing the desired pattern, is placed over the photoresist-coated substrate (exposure). Ultraviolet light is then shone through the mask, exposing the photoresist in specific areas (2). The exposed photoresist is treated with a developer solution (3), causing it to either dissolve (positive photoresist) or remain (negative photoresist) in the exposed regions. Finally you can either deposit some new material (4a and 5a) or etch the material by (4b and 5b) that you have in the areas that are not covered by photoresist using a lift-off process.

The main idea is to conduct transport measurements, so the structures typically take the form of bridges with a width of 10 - 100 $\mu$m and a length of 10 - 500 $\mu$m depending on the sample and the specific measurements to be performed. On either side of the bridge, a pair of electrodes is placed to measure the resistance ($R = V \ / \ I$) or obtain the IV curves (to obtain $J_c$) in a 4 point configuration.

Therefore, as seen in the scheme in Fig.2.14, an electric current is passed between the two furthest electrodes ($I^+$ and $I^-$), and the voltage is measured between the two closer ones on the bridge ($V^+$ and $V^-$).

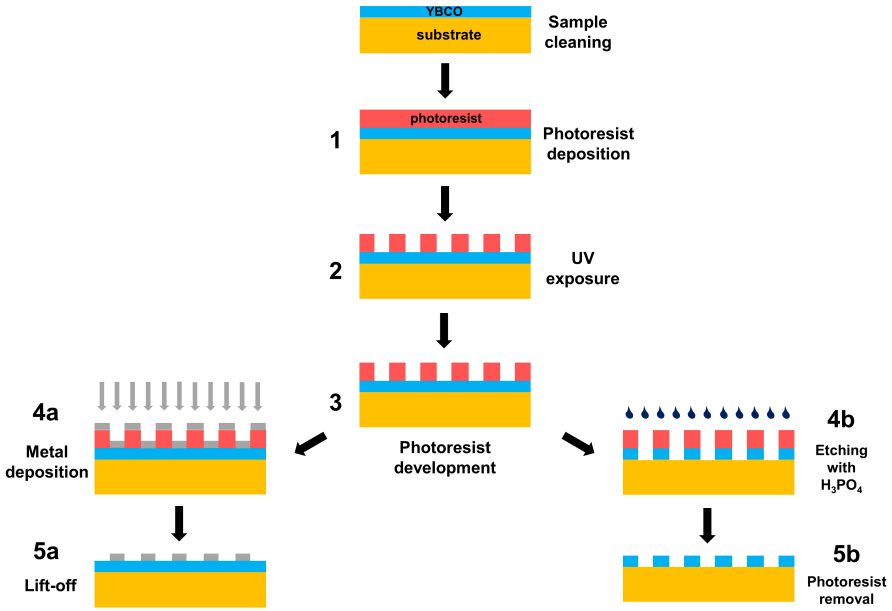



Figure 2.13: Sketch considering all the steps for a device fabrication through photolithography, also with the metal deposition and the etching processes.

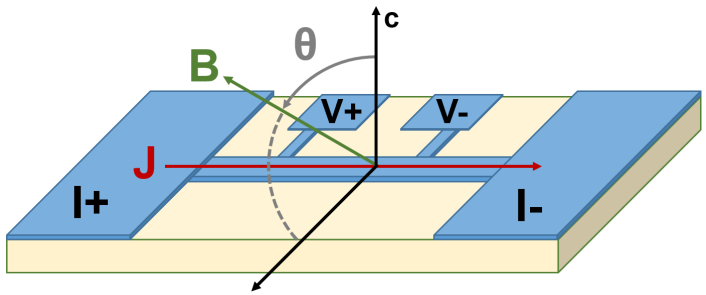



Figure 2.14: Scheme of the 4-point bridge configuration used in the transport measurements. Magnetic field is rotated in a plane perpendicular to the current to be in a maximum Lorentz Force configuration.

Initially, we design the pattern or layout that is intented to transfer to the film. For that we used a specialized software called CleWin5 to create a photomask with the desired pattern. This involves adapting

it to the area of our samples and the dimensions of the devices we wish to study, with micrometric precision. Thanks to this software a *cif* document is created that can be imported to a Microwriter which illuminate the desired regions with ultraviolet light. Fig.2.15 shows an example of a *cif* archive created using this software, where different layers are drawn, which can be illuminated in different conditions on the sample.

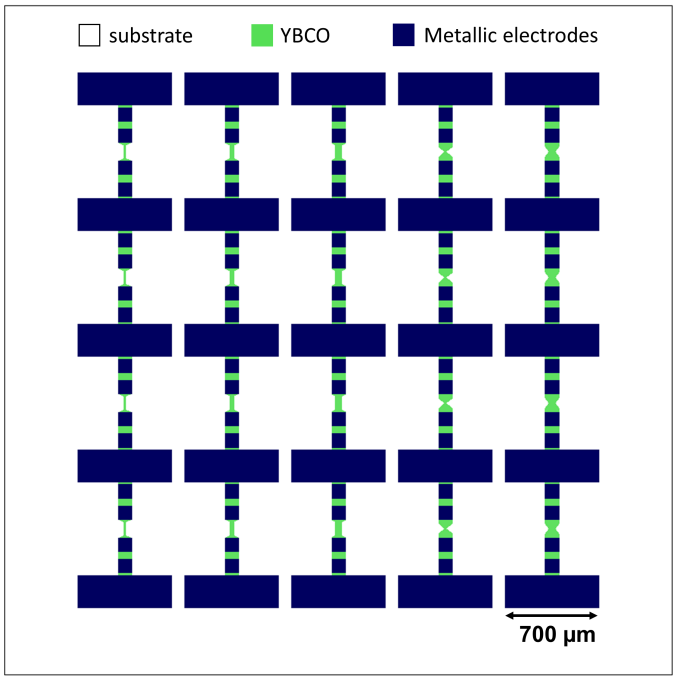



Figure 2.15: Example of lithography pattern or layout designed with CleWin5 where different layers are created to pattern YBCO tracks and metallic electrodes.

Once the mask has been designed it is time to go to the Clean Room. The sample undergoes a meticulous cleaning process with acetone, ethanol and isopropanol and drying it with nitrogen spray gun to eliminate any contaminants, as a cleaner surface enhances the development of the resist. Following this, a SHIPLEY 1813, positive photoresist, is applied using the spin coating technique, with a dropper and the sample positioned within a spinner. This step takes 25 seconds, operating at an angular speed of 5000 rpm, obtaining a uniform photoresist thickness of 1 mm. After that the sample goes on a hot plate for a soft-bake at 90 °C during 1 min to remove the solvents.

The next step is to put the sample into the lithography system, in this case, the Micro-Writer ML3 from Durham Magneto Optics Ltd (Fig.2.16). It is a last-generation miro-writing device which incorporates high-performance laser-assisted (385 nm) technology. The system enables a direct-writing lithography by computer-controlled optics to project the exposure pattern (done by CleWin5) directly onto the photoresist. Marking three corners of the sample, the software can align it and a focus of the writing laser is performed at the center. Subsequently, the designated pattern for transfer is uploaded, and the remaining parameters are adjusted based on the pattern's characteristics. Also before the illumination some focus can be done at certain indicated spots and a local alignment can be used to correct little misalignment's and to optimize the process.




Figure 2.16: Micro-Writer ML3 from Durham Magneto Optics Ltd available at ICMAB clean room.

After the UV light illumination the development takes place. The sample is introduced in a beaker full of a liquid developer, made of tetramethyl ammonium $C_4H_{12}N^+$ diluted in water (2 %), for 1 minute. Afterwards the sample is introduced in distilled water around 30 seconds with the aim to stop the reaction. Once the sample is dried then is checked with the optical microscope (with UV filter light) to see if the photoresist is correctly removed in the wanted areas and if the pattern is correct. If not, then acetone is used to remove the remaining photoresist and we have to start again by cleaning the sample.

After the photolithography process there are two options depending on the purpose: metal deposition and lift-off or etching of the material. If the goal is to achieve some metallic electrodes, then DC sputtering system will be employed for the metal deposition (Fig.2.17). The targets used typically are gold (Au) and silver (Ag), one or another will be used depending on the fabricated devices (this will be specified in each chapter). The sample is affixed to the holder, and the chamber undergo evacuation to achieve the necessary vacuum level ($10^6$ mbar) and plasma conditions.

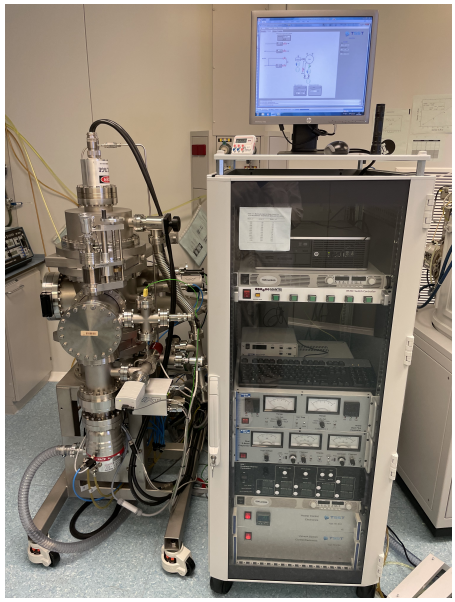


Figure 2.17: Ion Milling/Sputtering/E-Beam from TSST. The system was specially designed to combine the three techniques in the same equipment.

In the sputtering chamber, a metal target is subjected to bombardment by accelerated ions of an inert gas (Ar). The metal atoms are expelled onto the sample, positioned at a specific fixed distance in front of the target and during certain amount of time, with the rate already known and calibrated. The deposited metal makes contact with the surface of the YBCO only in the regions where the photoresist has been exposed to UV light and subsequently developed. Once the metal covered the whole sample surface, lift-off process was performed, where the photoresist and the metal on top of it will be gone, and the desired electrodes will stay on the YBCO. To do so, the sample was introduced in a beaker with acetone and submitted to an ultrasonic bath.

It is important to mention that before the metallic deposition, samples were introduced in a Plasma Cleaner Zepto M2 from Diener Electronics in order to remove any possible photo-resit insuring a proper cleaning of the surface. It consists on a low-pressure plasma technology, where the gas is excited by energy supplied in vacuum. This results in energetic ions and electrons, as well as other reactive particles, which constitute the plasma (in our case 1:1 mL of $O_2$:Ar, during 5 minutes). After that, and before the metallic deposition, the sample was placed into the ion-milling chamber for some seconds (10 - 20) in order remove few nanometers of the surface material. This cleaning processes will help to obtain better quality surfaces in the areas of metallic electrodes and therefore improve the contact resitance.

In the case of the etching of the material, chemical or the physical processes may be used. Physical etching is used in the ion miller located in the same chamber as the sputtering. Under specific vacuum conditions with the presence of an inert gas, Argon in our case, Ar ions are generated from an ion gun and directed towards the sample, thereby removing the material from the surface. Parameters such as pressure, ion flow, and accelerating voltage have been optimized to achieve a specific etching rate for different species. Argon milling was very useful in the case of having small features to be etched or in order to remove some parts of thin insulating material in intermediate photolithography processes performed in some samples (more details are given in Chapter 4).

While the Ar ions may affect the photoresist, its etching rate is considerably slower than that of YBCO or the other materials, providing protection to the layer. However, collisions of Ar ions during milling can generate heat, raising the sample's temperature to levels that may deoxygenate or damage the material. To mitigate this, short runs with breaks of several minutes were implemented to dissipate the heat and a drop of silver paint was used to adhere the sample to the holder, also aiding in heat dissipation.

In the case of the chemical etching, the sample is immersed in diluted orthophosphoric acid ($H_3PO_4$) for a specific duration, depending on the concentration of the solution and the desired etch thickness. Typically the concentration was 1:100 for $H_3PO_4$:$H_2O$ and time range

from 5 seconds in thinner samples (10 - 50 nm) to 15 - 20 seconds for thicker samples (200nm). As this is a highly isotropic method, it is not suitable for very small patterns. However, it proves to be highly effective when defining features larger than 5 $\mu$m, offering simplicity, speed, and cost-effectiveness. To stop the etching process, the sample is then introduced into a beaker with distilled water for a few seconds. The material (YBCO) protected under the photoresist and the resist itself were not affected by the acid solution. Despite the sample being small, when performing the etching it is very visual to see the change of color from YBCO to substrate. However, optical microscopy was used to confirm that all the material was etched away.

### 2.3.2 Electron Beam Lithography

In general, all the patterns required to perform transport measurements were don using optical lithography. However, in some of the samples studied in Chapter 4, where patterns of few microns or even smaller were needed, a higher-resolution technique was necessary. This is where electron beam lithography comes to play. The steps in e-beam lithography are similar to photolithography, namely: mask design using software, preliminary cleaning of the sample, resin deposition, sample illumination, development process, subsequent metal deposition and lift-off or etching of the material, and finally, the removal of the resin and any potential metallic residues. Nevertheless, there are several significant differences in each mentioned step.

Firstly, in the mask design, CleWin5 can be used, but it is better to use the program asociated to the SEM software which works better and save files in gds format. Cleaning the sample can indeed be done in the same way by applying acetone, ethanol, and isopropanol. The resin used is different (PMMA), and therefore, the deposition conditions are also different. PMMA (poly methyl methacrylate), a positive e-beam resist consisting of long polymer chains of carbon atoms which comes in various molecular weights, is applied using the spin coating technique, with a dropper and the sample positioned within a spinner. This step takes 1 minute, operating at an angular speed of 3600 rpm. After that the sample goes on a hot plate for a bake at 180 °C during 1 min in order to remove the solvents.

Then the sample is placed into the SEM and an electron beam is directed onto the coated sample. This beam is controlled with precision using magnetic lenses and deflection systems. The focused electron beam scans across the surface of the sample according to the pattern in the mask. In this case, alignment and focus of the the sample cannot be done in the exposure areas and neither the free movement around the sample because the beam would expose unwanted regions.

So that, a shutter is used when the beam needs to be moved on top of the sample. The problem is that one could be blind and do not find the proper region where the pattern needs to be performed. This can be solved by doing certain marks with photolithography with well known position which can be used as a reference (red crosses in Fig.2.18). In the case of photolithography, this process is much more simple since one can directly image the sample with yellow light.

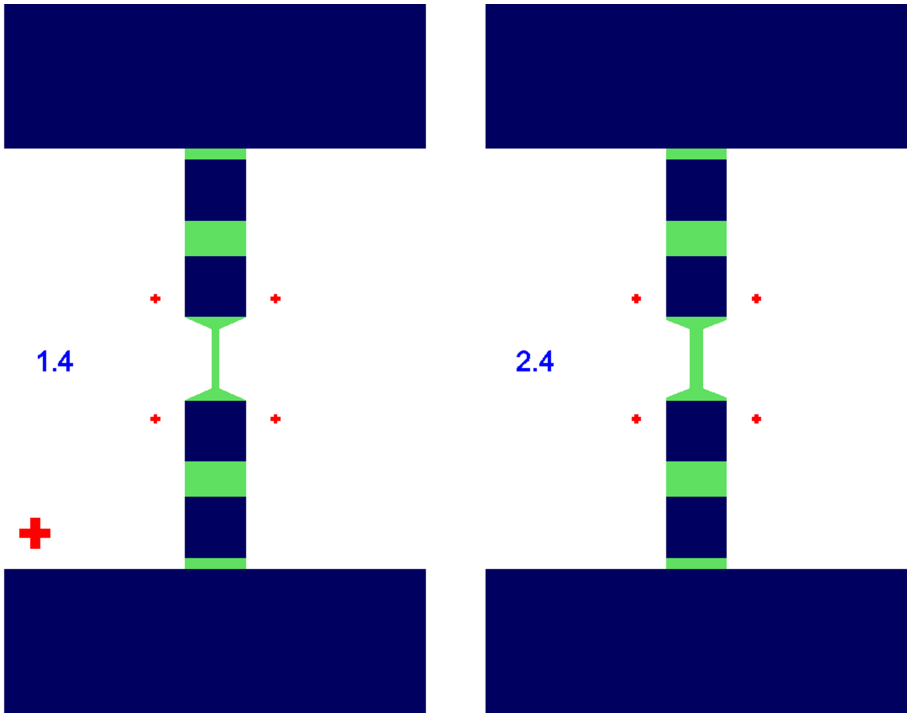



Figure 2.18: Example of a mask design with CleWin5 where the red crosses close to the devices represent the marks used for the e-beam lithography alignment.

So the steps can be the following: go to one mark, give its coordinates, close the shutter, move to the next mark, open the shutter, mark it and so on. Once the sample is already focused and aligned then the electron beam can be exposed above the designed patterns (bridges). After the resist exposure the development takes place. The sample is introduced in a beaker full of a liquid developer, in this case a mixture of MIBK (methyl isobutyl ketone) : IPA (isopropanol) with concentration 1:3 respectively, for 1 minute. Afterwards the sample is introduced in isopropanol for around 30 seconds to stop the reaction. Once the sample is dried, optical microscopy was used to check if the photoresist was correctly removed in the desired areas, and if the pattern was good. If not, acetone was used in order to remove the remaining photoresist and the sample had to be cleaned again.

### 2.3.3 Thermal Scanning Probe Lithography

As it will be seen in Chapter 5, a Direct Laser Writing is used to modulate the oxygen in YBCO samples through temperature. This was possible thanks to the NanoFrazor Explore located in Polifab, a micro and nanofabrication facility of Politecnico di Milano, that I could use, with the help of Dr. Edoardo Albisetti and their students.

The NanoFrazor Explore (Fig.2.19) is a nanofabrication tool that relies on Thermal Scanning Probe Lithography (t-SPL) [148, 149]. With an ultra-sharp heatable probe tip capable of both writing and imaging, it facilitates the creation of intricate, high-resolution nanostructures efficiently. Additionally, it features a laser writer module ($\lambda$ = 405 nm CW fiber laser) to expedite coarser patterning, enabling the rapid generation of both nano- and microfeatures on the same resist in a single fabrication step through a unified software platform.

The heated probe tip creates high-resolution nanostructures by local sublimation of thermally sensitive resists (mainly Polyphthalamide, PPA), so no wet development is required as the resist is removed directly. Laser writing enables fast direct resist sublimation for large-area patterning (contact wires and pads). Thermal probe writing enables high precision and high resolution for the critical parts of the nanodevice [150]. However, in our samples, we have not deposited any resist and the laser beam is closely in contact with YBCO films.

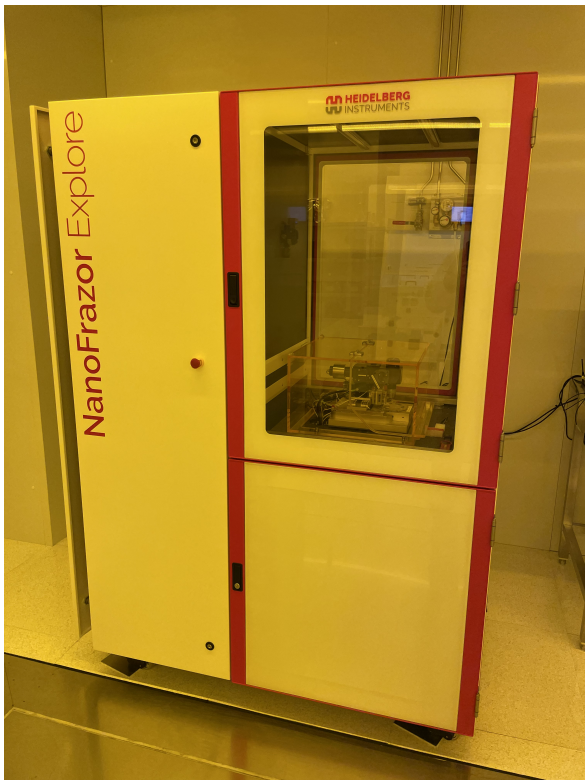



Figure 2.19: NanoFrazor Explore that allows direct laser writing and thermal scanning probe microscopy, located in Polifab. Politecnico di Milano.

YBCO samples are introduced in the NanoFrazor in vacuum or $N_2$ conditions and for optimization of the process, some calibrations were done. After that instructions are given in the software to apply specific parameters such as power, size, time (numbers will be given in Chapter 5). The temperature of the tip can rise up to 1200 °C and the temperature of the laser close to the film, up to 800 °C.

## 2.4 Electrical transport measurements

In this section we will described the techniques used for electrical transport measurements once the YBCO films were characterized and patterned. So we will give details about how we connect the samples to the sample holder, how we measure them, and the techniques, hardware and software we used.

### 2.4.1 Wire bonding

When connecting the samples to a puck (sample holder) for subsequent transfer to the laboratory for measurements, two connection methods have been employed. In the case of the samples from Chapter 3, Al wires with 0.05 mm in diameter were manually connected, placing a drop of silver paint at each end of the wire (one drop on the metallic electrode and the other on top of the puck contacts). Care must be taken to ensure that the silver drop only reaches the electrode and does not spread to other areas of the sample, as it can create a short circuit.

For the other samples used in Chaper 4 and 5 the wire-bonding technique with the Ultrasonic Wire Bonder 4526 from Kuliche & Soffa (Fig.2.20) was used to establish connections between the electrodes and the designated sample holder. This technique involves a needle with an aluminum wire of tenths of microns in diameter being pressed against the electrode and attached through ultrasound vibrations and pressure.

The bonded wire on the sample was extended to the desired pad on the puck and connected there using the same procedure. One can change parameters of the bonding such as force, time and power depending of the electrodes and the sample, because the attaching would be different.



Figure 2.20: Ultrasonic Wire Bonder 4526 from Kuliche & Soffa.

Fig.2.21 illustrates three different type of pucks equipped with various contacts that can be linked to the experimental setup (PPMS or external voltage/current sources) using BNC connectors standard wires. To facilitate the easy reconfiguration of the puck's pins for measurements in different regions and configurations, a switch box (fabricated by previous PhD students) that interconnects between the puck and the electronics of the PPMS or the external source-measure units (SMUs) was used.

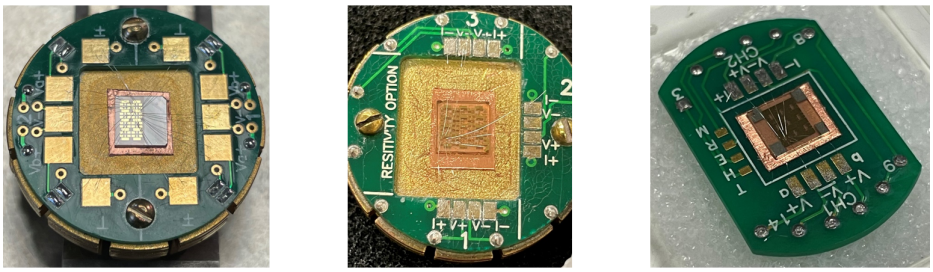



Figure 2.21: YBCO samples mounted and contacted on top of, from left to right, a round ACT puck, a round resistivity puck and a rotating puck.

### 2.4.2 Physical Property Measurement System

Once the sample was bonded on the puck, it was mounted into the Quantum Design Physical Property Measurement System (PPMS) in order to perform the electrical transport measurements. The heart of this system enables the generation of magnetic fields up to 9 T and provides control over the sample space temperature within the range of 1.8 K to 400 K, maintaining a stability condition of less than 0.1% oscillation. While the system offers various measurement options, only two: Resistivity and AC Transport were utilized.

For the resistivity option, the PPMS system is integrated with a current source and a multiplexed voltmeter across three channels. This configuration allows the determination of the resistance of three samples quasi-simultaneously, employing a four-point measurement approach. Automatic and cyclical switching between samples occurs multiple times per second, facilitating the determination of the resistivity and Hall effect of the material under investigation.

In AC Transport, a waveform generator is employed to generate driving signals utilized by the current source for producing alternating currents. The bundled voltmeter gauges the voltage, and the acquired signal undergoes processing through lock-in-based software. The hardware is multiplexed to two channels, enabling the simultaneous measurement of two samples during a single session. The associated software is configured for measuring sample resistivity, I/V characteristics, Hall effect and superconducting critical current.




Figure 2.22: Quantum Design Physical property measurement system (PPMS), in this case together with the switch box and Keithley 2450.

Depending on the sample and type of measurement resistivity or AC Transport were chosen. For instance, for Hall measurements in uniform YBCO films (not patterned) the resistivity option is better. On the contrary, with the aim to get I/V curves and extract the critical current density the AC Transport option was used. But if the goal is to measure the resistivity (resistance) or Hall effect in patterned YBCO devices both options can be employed. The software utilized for the PPMS measurements was provided by the manufacturer and fulfills all our requirements. Thanks to this software various sequences given specific orders of scans in temperature, magnetic field or orientation with determined parameters, can be created, facilitating the automation of the procedure.

#### 2.4.2.1 $T_c$ and $J_c$ measurements

The measurement of resistance as a function of temperature is conducted to identify the transition from normal to superconducting states under various applied magnetic fields. The rates of temperature variation and the acquisition of values are adjusted based on the resistance gradient across different temperature ranges. For instance, from 300 K to 95 K is scanned at the highest speed, using a ramp of 20 K/min and measuring the resistance every 5 K. Near the critical temperature ($T_c$), the temperature ramp was decreased to 1 K/min to ensure temperature stabilization, with resistance measurements taken at intervals of 0.2 K. This ensures consistency in measurements whether the temperature is increasing or decreasing.

As commented previously, the resistance values are obtained dividing the measured voltage $V$ by the applied current $I$. In most of the cases an AC current of 0.01 mA and frequency 33 Hz was applied. Sometimes higher current was required when the signal was too low, always with a compliance current of 0.1 A. In Fig.2.23, it is represented the resistance of a YBCO device as a function of the temperature. The criterion to achieve the critical temperature, $T_c$, is at the temperature when the normalized value $R\ /\ R(300K) = 10^{-3}$, as marked in the graph.

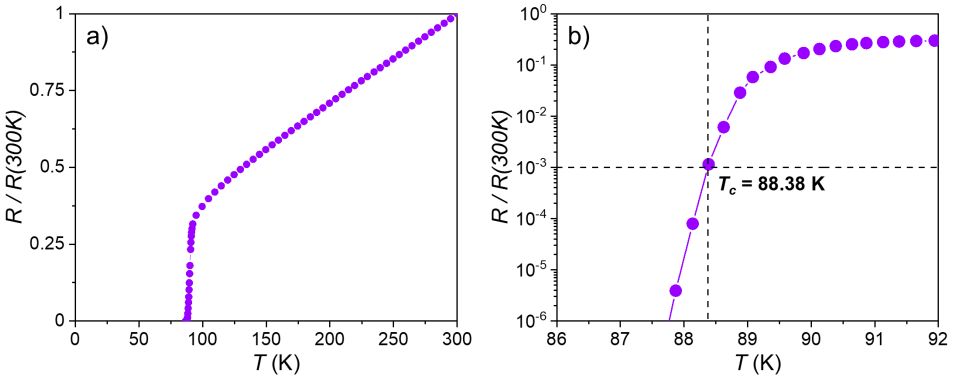



Figure 2.23: Normalized resistance dependence on the temperature in a) linear scale, b) log scale and showing the criterion for obtaining $T_c$.

In the I/V curves, the measurement of voltage drop as a function of applied current is conducted to ascertain the critical current density of our samples. The electrical current is incrementally raised from

0 to a certain $I_{max}$ in 256 steps. It is very important to do a previous calibration avoiding more heat, starting with low current and then increasing it until the typical behavior of the IV characteristics is obtained (Fig.2.24).

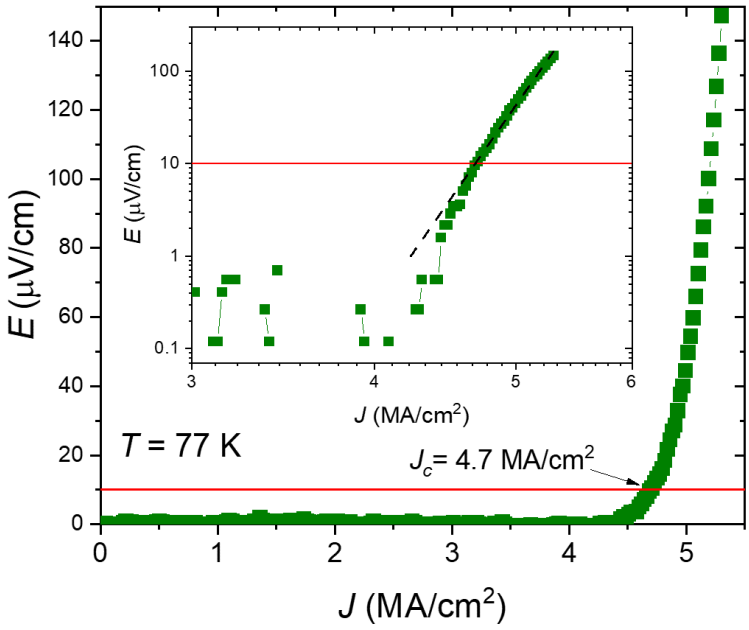



Figure 2.24: $E(J)$ curve of a YBCO thin film at 77 K and self field showing a critical current density of 4.7 MA/cm$^2$. Inset shows the log-log representation of the $E(J)$ curve at 77 K and 0 T.

Ideally, as it was explained in the introduction chapter, the critical current ($I_c$) is defined as the maximum current that the superconductor can sustain without dissipation, but in experimental scenarios, voltage drops at the nanometric scale are always measured due to offset-measurement devices. Therefore, a criterion must be applied to determine $I_c$. Considering that the electric field is given by $E = V/l$, and $l$ is the distance between voltage connections, a criterion of 10 $\mu$V/cm was employed.

### 2.4.2.2 Hall measurements

The Hall effect is observed when an out-of-plane magnetic field is applied to a wire carrying charges (Fig.2.25. Due to the Lorentz force law, which states that the magnetic force exerted on the charges is

perpendicular to both the magnetic field and their velocity (therefore also the electric current $I$), the charges are displaced to one side of the conductor, resulting in the generation of a transverse voltage or Hall voltage ($V_H$).

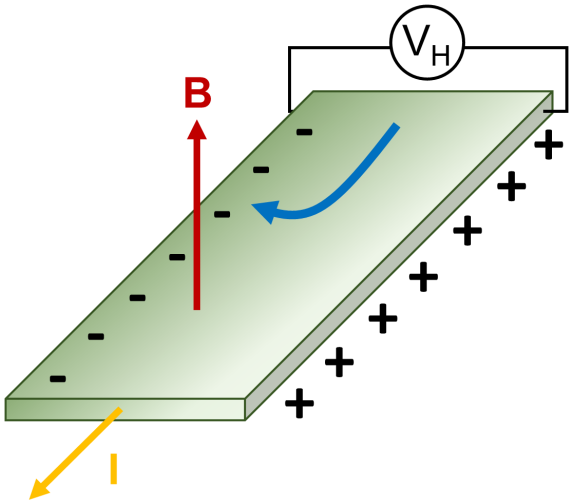



Figure 2.25: Sketch of the Hall effect with the characteristic parameters involved.

The experimental measurement of the Hall voltage allows the deduction of the velocity of charge carriers and their concentration. This is because, once a stationary situation is reached, the electric force acting on each charge balances with the magnetic force. It follows that the Hall voltage is directly proportional to the electric current and the magnetic field, and inversely proportional to the number of carriers per unit volume ($n_H$). Considering that $t$ is the thickness and $q$ is the charge of the carriers:

$$V_H = \frac{IB}{n_H q t} = R_H \frac{IB}{t} \tag{2.4}$$

Then we can define the Hall coefficient as $R_H = 1/qn_H$, so if this last parameter is obtained by specific measurements, the carrier concentration can be extracted with:

$$n_H = \frac{1}{qR_H} \tag{2.5}$$

Hall measurements are performed in the PPMS at room temperature applying a magnetic field ramp from -9 T to +9 T (sometimes from -5 T to +5 T) along the c-axis (perpendicular to the sample) and obtaining the resistance values using two different configurations depending on the samples. For uniform samples that were not patterned, a Van der Pauw configuration [151] is used, so four wires are bonded with silver paint in the four corners (example depicted in Fig.2.26a).

Then at a given magnetic field, a current is applied between two contacts diagonally ($I_{24}$) and in the other two the voltage is measured ($V_{13}$) (see left scheme in Fig.2.26a) and therefore the resistance can be calculated ($R_{13,24} = V_{13}$ / $I_{24}$). Afterwards, the same measurement is performed but changing the configuration of the contacts (see right scheme in Fig.2.26a) and therefore $R_{24,13} = V_{24}$ / $I_{13}$. The total resistance contribution can be obtained averaging the two different contact configurations along the full field range ($R = (R_{13,24} + R_{24,13})$ / 2)). That way, offset contributions resulting, for instance, from contact misalignment and sample inhomogeneities can be averaged out.

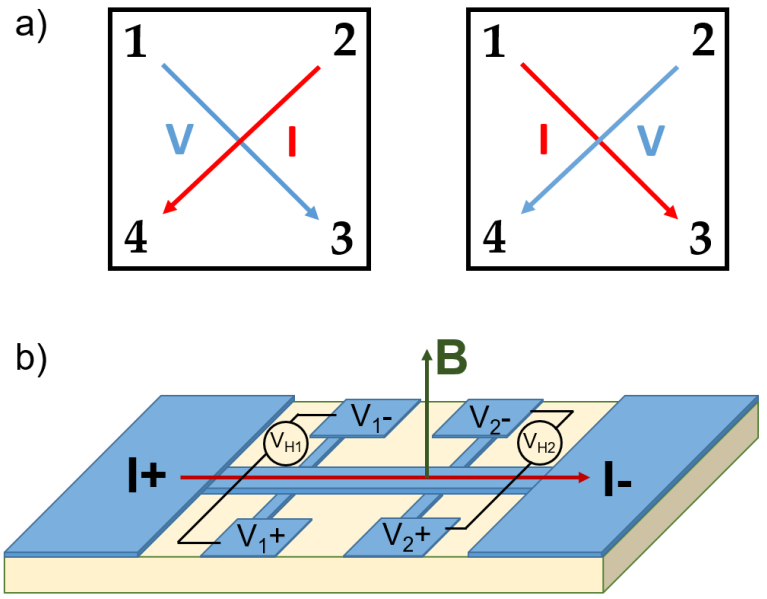



Figure 2.26: Scheme of the contacts configuration in order to calculate $n_H$: a) Van der Pauw for not patterned samples and b) 4-point configuration for patterned samples.

A linear behaviour is obtained and the slope value, that represents the Hall coefficient $R_H$ [96] divided the thickness $t$ of the sample (eq.2.6), can be extracted. Once the Hall coefficient is obtained it follows the calculation of the $n_H$ value with the charge of the carriers $q$ thanks to the eq.2.5.

$$R = \frac{R_H}{t} B \tag{2.6}$$

In the case of samples patterned with Hall voltages in a 4-point configuration, a current between the larger and more distant contacts (always from + to -) was applied and the voltage between the smaller contacts was measured. In this way, two channels were obtained and therefore the number of carriers at two different points on the bridge (Fig.2.26b) can be evaluated. In this case, the slope of the total resistance can be directly obtained.

### 2.4.3 Source Measure Unit (SMU)

In Chapter 4, we use a contact gate to study field-induced oxygen motion effects. In this case, resistive switching (RS) loops were induced by using an external Keithley 2450 SourceMeasure Unit (SMU) implemented at the PPMS (Fig.2.27). The external source was used to apply votage through the gate while the PPMS cryostat was used to measure the sample resistance under controlled magnetic field and temperature.




Figure 2.27: Keithley 2450 SourceMeasure Unit (SMU) implemented to the PPMS to obtain resistive switching loops.

Voltage sweeps (Fig.2.28) consisted of 100 total points, progressing from 0 V to the desired voltage (positive or negative) and then back to 0 V, with a compliance current of 0.1 A. The duration of the sweeps depends on the NPLC (number of power line cycles) parameter of the SMU, determining the integration time for power line-induced AC noise at each applied voltage. While reducing the NPLC increases the measurement speed, it comes at the cost of accuracy. After testing different values, we found high accuracy with voltage sweeps of 100 total points, total time length of 11 seconds and time per pulse of 0.11 seconds. This time could slightly increase when applying high voltages (above 10 V).

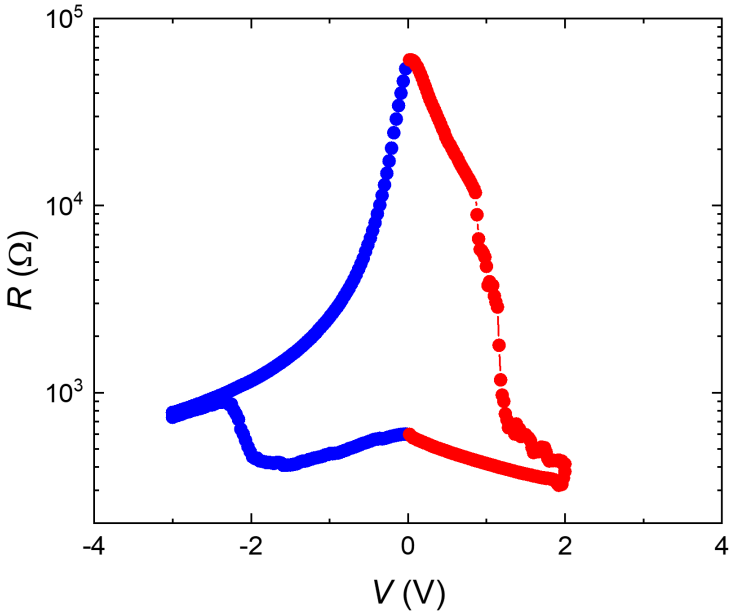



Figure 2.28: Voltage sweeps (positive in red and negative in blue) performed to obtain the Resisitve Switching effect.

# Chapter 3

# Ba-deficient solutions for high-performance superconducting YBCO films

HTS cuprate materials, in particular $YBa_2Cu_3O_{7-x}$ (YBCO), has attracted most of the attention of researchers because its superconducting features make it a good candidate for the fabrication of high-current cables and power devices based on YBCO-coated conductors [48, 152]. $YBa_2Cu_3O_{7-x}$ possesses exceptional capabilities to carry high critical currents even at elevated magnetic fields, rendering it a highly promising material for high-temperature superconducting (HTS) wires.

These wires, based on second-generation coated conductors, hold significant potential for various power applications and magnet technologies [48, 63, 153]. Additionally, there is a growing interest in high-frequency applications driven by the escalating performance requirements of accelerating cavities [154]. This interest extends to emerging fields such as the search for galactic axions [155] or electromagnetic screenings in the future deployment of particle colliders [156].

To enhance the performance of YBCO under high magnetic fields necessary for practical applications, considerable efforts have been directed towards nanoengineering the defect landscape of YBCO by introducing artificial vortex pinning centers [83, 84, 89]. Various strategies have been proposed to introduce nanodefects in YBCO thin films grown by different methods. One successful approach involves the in-

corporation of non-superconducting secondary phases [157]. In particular, for vacuum-based growth techniques like pulsed laser deposition (PLD), chemical vapor deposition (CVD), or hybrid liquid phase epitaxy (HLPE), simultaneous growth of the YBCO superconductor and secondary phases can be controlled to form self-assembled nanostructures such as columnar nanorods along the c-axis, with coherent or semi-coherent interfaces with the YBCO matrix [89, 158]. Recent advancements have shown excellent magnetic flux pinning at 77 K with remarkably high irreversibility fields ($> 10$ T) in YBCO films grown by PLD with $Ba_2YNbO_6$ (BYNO) [159], also $Ba_2YTaO_6$ (BYTO), and mixed BYNO + BYTO (BYNTO) nanorods [79, 160].

Conversely, chemical solution deposition (CSD) routes have progressed towards cost-effective production of YBCO films for various applications [161–163]. In recent years, significant effort has been devoted to preparing CSD-based YBCO nanocomposite thin films with a variety of nanoparticle compositions. These compositions, including $BaZrO_3$, $Ba_2YTaO_6$, $Y_2O_3$, $BaCeO_3$, $BaSnO_3$, and $BaHfO_3$ (BHO), are either achieved through the in-situ spontaneous segregation of nanometric oxide secondary phases during the YBCO conversion [84, 164] or by adding preformed nanoparticles from colloidal solutions [137, 165, 166].

Incorporating nanoparticles substantially alters the $YBa_2Cu_4O_8$ (Y124) intergrowth landscape [137, 166, 167], resulting in increased nanocomposite nanostrain. These nanocomposites exhibit enhanced isotropic pinning contributions across a broad field and temperature region [83, 84, 167], even approaching the irreversibility line [61, 168].

In this chapter a Ba-deficient low-fluorine TFA route to grow YBCO thin films, characterized as straightforward, inexpensive, eco-friendly and high-performing, is optimized. We have carefully analysed the morphology and the superconducting performance of these samples as compared to pristine and nanocomposite YBCO films, to elucidate the nature and strength of pinning centres naturally induced when growing at low temperatures. The influence of the precursor solution and growth temperature on the doping level of the films has also been evaluated

## 3.1 Barium-deficient solutions

The technologies to grow YBCO thin films can be divided into physical and chemical methods. On the one hand, vacuum methods comprise the most widely studied techniques like pulsed laser deposition (PLD) [139], physical vapor deposition (PVD) [169], and metal-organic chemical vapor deposition (MOCVD) [170, 171]. They require ultra-high vacuum systems, which raise production costs and cause difficulties in scaling up the length of the process. On the other hand, representative non-vacuum methods are chemical solution deposition (CSD) techniques, which are currently in an advanced development stage [131, 163, 172].

The recent progress made on CSD YBCO growth and the feasibility of adapting this approach to large-scale production processes has led this procedure to be considered as a low-cost, reliable and long-lasting coated conductor fabrication technique. Furthermore, CSD offers additional advantages such as an accurate control of the stoichiometric composition, a high deposition speed even on large areas, and a high homogeneity of the deposited layer, limiting the formation of non-superconducting phases.

The most widely employed methodology among CSD growth routes of YBCO is metal-organic decomposition (MOD) [173], in which the organic matrix that surrounds the metal ions is removed by thermal decomposition. Several metal-organic salts have been successfully used: acetylacetonates [128], acetates [174], propionates [134], and trifluoroacetates [175], etc. Among them, the most widespread procedure for YBCO deposition is the one involving trifluoroacetate (TFA) salts [176].

However, the TFA-MOD method has several disadvantages such as the extreme sensitivity to humidity in air and the high concentration of fluorine in the starting solutions, which leads to a non-eco-friendly route [177]. Nevertheless, the presence of fluorine is essential for the growth of the superconductor if one wants to avoid alternative routes using fluorine-free precursors, which have $BaCO_3$ decomposition as an intermediate phase [176, 178, 179]. Thus, a reduction of the fluorine content to that strictly necessary to form $BaF_2$ as a sub-product from the pyrolysis was investigated [134, 180, 181].

The stoichiometric composition of the precursor solutions has been proven to have a remarkable influence on the final properties of the samples [182]. The ratio of the metalorganic salts of Y/Ba/Cu = 1:1.5:3 (Ba-deficient) has been shown to be effective for obtaining YBCO films with higher critical current density ($J_c$) than that obtained for YBCO layers fabricated with the standard ratio Y/Ba/Cu = 1:2:3 [183]. However, there is little knowledge on the mechanism of influence of the starting solution composition on the superconductive properties of YBCO films.

A first hypothesis links the improvement of transport properties to a denser, more homogeneous microstructure with reduced porosity and segregation of secondary phases [184]. Moreover, the growth temperature plays an important role on the amount and nature of the pinning defects induced within the YBCO matrix, and the associated pinning anisotropy and strength [140, 185]. So, growth temperature can be used to naturally tune the defect-pinning landscape of YBCO films without the need to incorporate additional secondary phases.

The starting solutions were prepared by dissolving barium and copper acetates, and yttrium trifluoroacetate (low-F) with the ratio of Y/Ba/Cu equal to 1:1.5:3 (Ba-deficient). The growth processes were carried out through two different methods: conventional thermal annealing (CTA) and flash heating (FH, see section 2.1 for more details). The idea was to study the influence of the heating ramp in the pinning landscape originating within the films and, therefore, in the final superconducting properties.

## 3.2 Patterning of YBCO films for transport measurements

In order to be able to perform transport measurements samples were patterned with current and voltage contacts in a four-probe configuration. That means that an electric current was applied between two big electrodes and the voltage was measured between another two electrodes through a bridge. Typically, in each sample, four devices (four bridges with the respective electrodes) were patterned (Fig.3.1a), in order to have statistic measurements and in case some of the bridges could be damaged during measurements. To do so, photolithography

combined with sputtering and lift-off were used to deposit 200 nm thick silver contacts on top of large paths which were used to apply current (650 $\mu$m $\times$ 1750 $\mu$m) and measure voltage (785 $\mu$m $\times$ 550 $\mu$m). In order to assure good contact resistance, samples were annealed at 450 °C during 1 h. Photolithography and wet etching were used to pattern YBCO tracks of 10, 20, 30 and 50 $\mu$m width and 500 $\mu$m length. An example of a patterned device (30 $\mu$m width) with the described geometry is shown in Fig.3.1b.

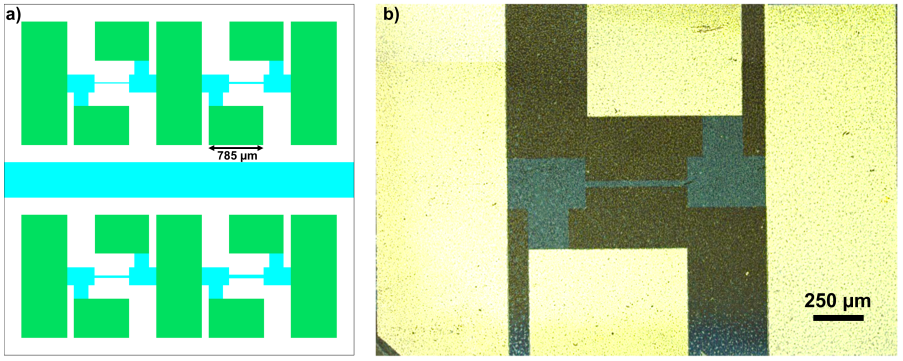



Figure 3.1: a) Template of the 4 patterned devices in a four-probe configuration, b) Optical image of a device, where it can be seen the YBCO track (grey), the substrate (black) and the four silver annealed electrodes (yellow).

## 3.3 Microstructural characterization

The surface morphology of the YBCO films was investigated using a scanning electron microscope (SEM). In Fig.3.2 and 3.3, SEM images of YBCO layers grown at different temperatures using FH and CTA methods are shown, respectively (see section 2.1 for growing conditions of the two methods). As a general tendency, it can be observed that the higher the temperature, the lower the porosity. However, several holes can be observed on the CTA sample grown at 810 °C (Fig.3.3d), generated through a temperature-induced dewetting phenomenon [186]. Regarding the samples grown with the CTA method, no *ab* grains are present in the working temperature range (730 - 810 °C). Concerning the samples grown with the FH annealing, some *ab* grains (identified as elongated needles at 90° in the SEM images) are detected in the temperature range 700 - 730 °C, and their density decreases with increasing temperature. No *ab* grains are observed in any of the films for

the samples grown above 730 °C. Thus, SEM images suggest that the minimum temperature to assure *c*-axis nucleation for both CTA and FH is 750 °C.

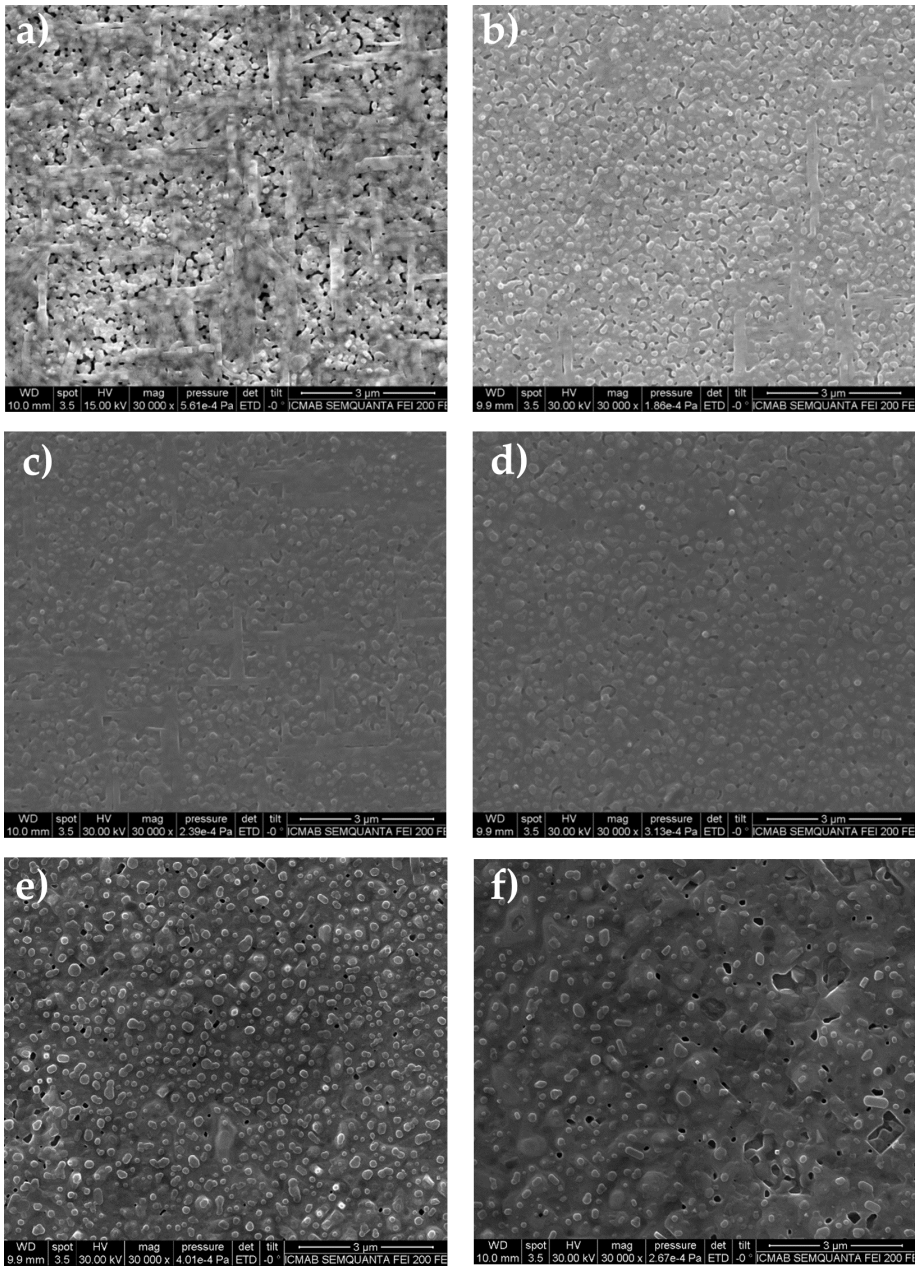



Figure 3.2: SEM images of different samples grown with the flash heating (FH) method at: (a) 700 °C, (b) 720 °C, (c) 730 °C, (d) 750 °C. (e) 780°C and (f) 810°C

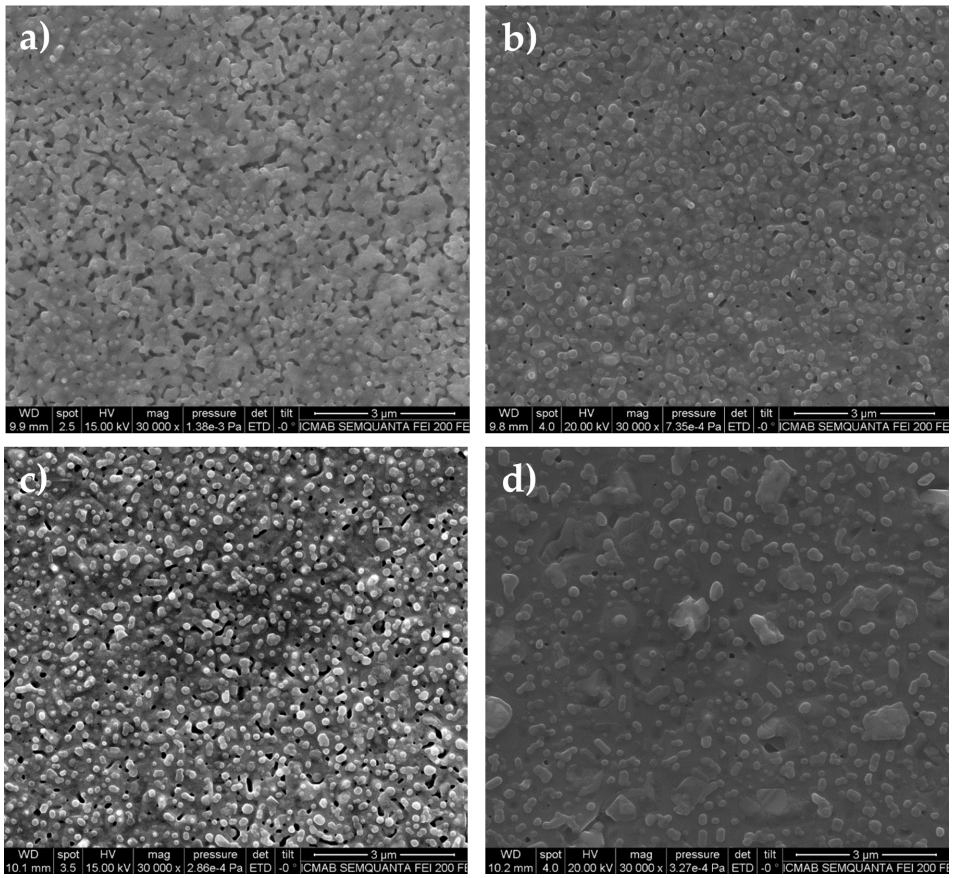



Figure 3.3: SEM images of different samples grown with the conventional thermal annealing (CTA) method at: (a) 730 °C, (b) 750 °C, (c) 770 °C, and (d) 810 °C .

The crystallinity of the samples was studied through X-ray diffraction (XRD). Fig.3.4 shows as an example the 2D-XRD frames obtained for an epitaxial CTA sample grown at 750 °C and an FH sample grown at a very low temperature (700 °C) where non-fully epitaxial YBCO was obtained. In the first case, a highly epitaxial, i.e., *c*-axis oriented, YBCO film was attained, with the YBCO (00l) peaks (YBCO (003), YBCO (004), YBCO (005) and YBCO (006)) clearly identified. One can also see a spot with less intensity that corresponds to the K$\alpha$ peak of LAO. In the case of the FH sample grown at 700 °C, shown as an example of a non-fully-epitaxial sample, one can clearly identify the polycrystallinity of the YBCO film with two spots associated with YBCO (102) (*ab* grains) and a ring associated with YBCO (103) (random orientation).

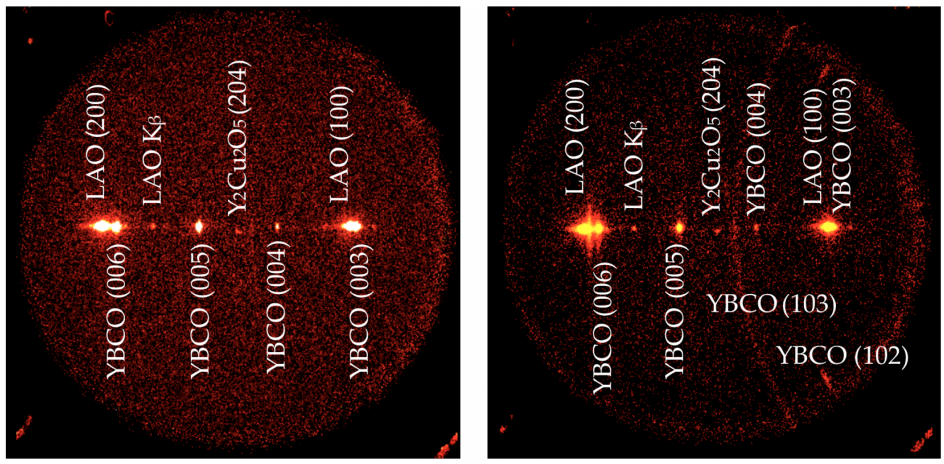



Figure 3.4: Two-dimensional XRD frames ($\chi$ vs. $2\theta$) from a sample grown at 750 °C with the CTA method (left) and 700 °C with the FH method (right).

In order to better complete the XRD analysis, the integrated 2D-XRD patterns of samples grown at different temperatures through both the CTA and FH methods are shown in Fig.3.5.

Regarding CTA samples (left column), we can see that at all four growth temperatures evaluated (730, 750, 770, and 810 °C) we obtain epitaxial films with *c*-axis YBCO (00l) peaks. It should be noted that, regardless of the growth temperature used, a very small contribution of $Y_2Cu_2O_5$ (with (211) and (204) reflections) can be identified, which is consistent with the barium deficiency imposed by the stoichiometry of the solutions.

Regarding FH samples (right column), we can see that at 730 and 750 °C we observe the same epitaxial YBCO (00l) peaks as those obtained for the CTA samples and also a small contribution of $Y_2Cu_2O_5$ (211). It is important to mention that for the FH samples grown at lower temperatures (700 and 720 °C), apart from YBCO epitaxial peaks we can also observe different polycrystalline reflections $Y_2Cu_2O_5$ (211), YBCO (103) CuO (11-1) and $Y_2O_3$ (113), where the YBCO (103) peak indicates a certain percentage of randomly oriented grains (see also Fig.3.4) in the films.

Fig.3.6 shows the (103) YBCO phi-scan ($\phi$-scan) and (005) YBCO rocking curve ($\omega$-scan) obtained for CTA and FH samples grown at

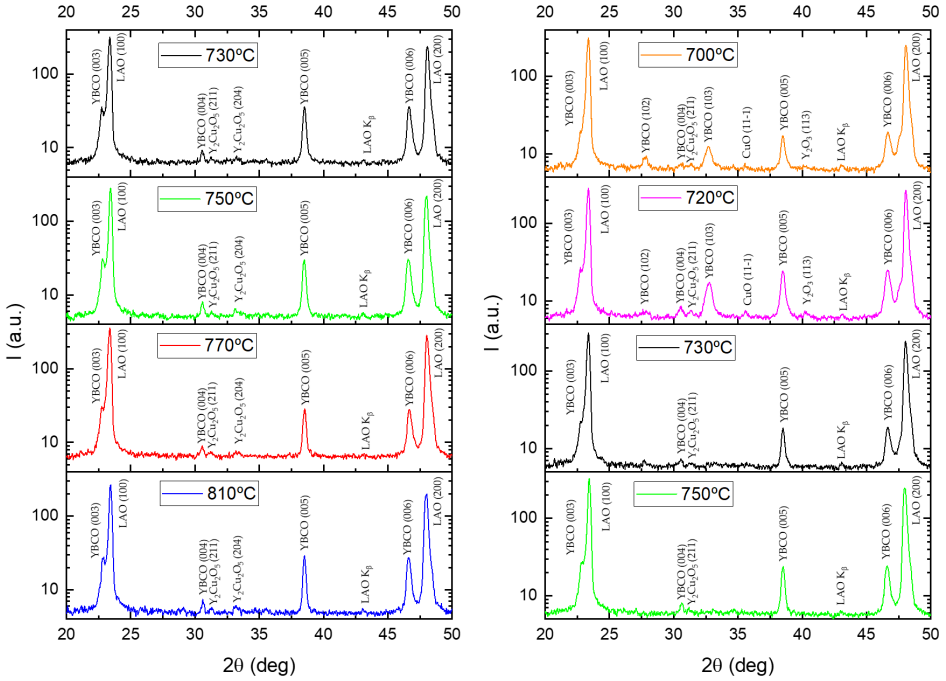



Figure 3.5: Integrated X-ray diffraction patterns obtained from eight YBCO films grown at different temperatures. The (left) panels correspond to the samples grown with the CTA method and the (right) ones to the samples grown with the FH method.

750 °C, which reveal the in-plane and out-of-plane texture quality of both films ($\Delta\phi = 0.2$ ° and $\Delta\omega = 0.58$ ° for CTA, $\Delta\phi = 0.42$ ° and $\Delta\omega = 0.48$ ° for FH). It should be emphasized, therefore, that films with a fairly good texture quality and a high purity are obtained at temperatures as low as 750 °C when Ba-deficient solutions are used.

This result is reminiscent of what has been previously observed in YBCO films including a certain amount of Ag in their composition where an extended growth window was identified [131, 187]. The main reason for being able to grow *c*-axis oriented YBCO films at lower temperatures in the TFA process is associated with a modified nucleation behavior, very likely due to a shift of the stability line of YBCO with Ba-poor compositions towards a lower temperature, which then also shifts the crossover temperatures from *c*-axis to *ab*-axis nucleation [188, 189].

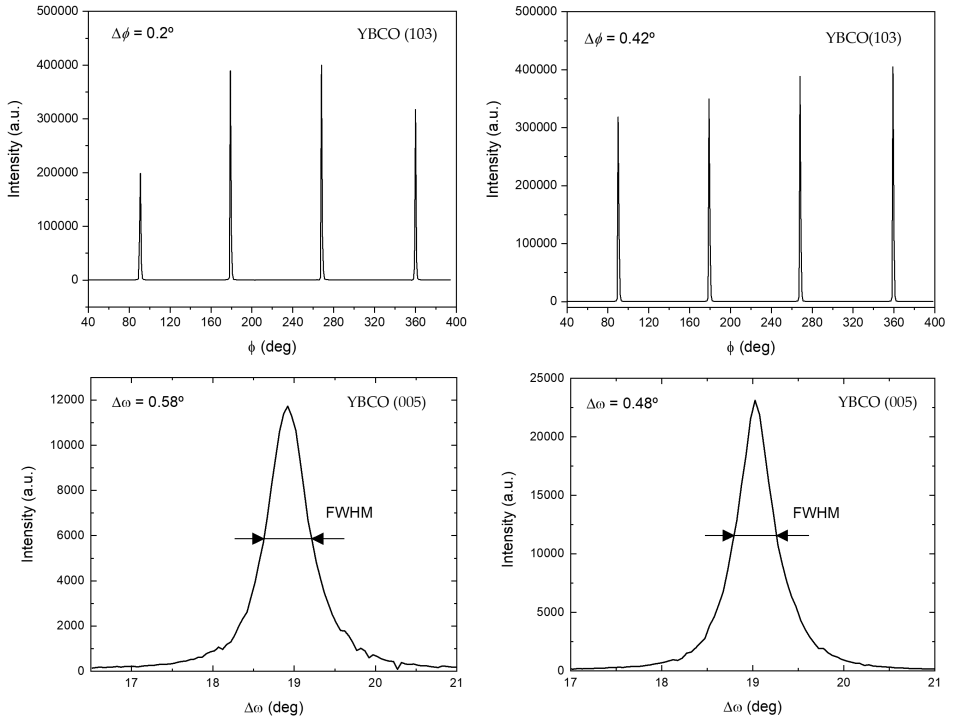



Figure 3.6: $\phi$-scan (103) YBCO and $\omega$-scan (005) YBCO obtained for YBCO films grown at 750 °C with the CTA (left) and FH (right) methods.

## 3.4 Influence of growth temperature on the superconducting performance

The self-field critical current density, i.e., $J_c$ measured at zero external field ($J_c^{sf}$), was evaluated for several samples grown at different temperatures, $T_g$, to compare their superconducting properties. $J_c^{sf}$ values obtained as a function of $T_g$ at 5 K and 77 K for both CTA and FH methods are represented in Fig.3.7, where certain tendencies can be identified. First, $J_c^{sf}$ increases with $T_g$ until the growth temperature reaches a value of 750 °C, where optimal nucleation and epitaxial growth are already achieved (trend shown with dashed red lines). For $T_g$ above 750 °C, the $J_c^{sf}$ values show an opposite trend (dotted blue lines). In this region, the increase of $J_c^{sf}$ with decreasing growing temperature is associated with an enhancement of pinning defects as shown in the following.

Therefore, competition between good percolation and pinning performance gives us an optimal $T_g$ of 750 °C, where very high critical current values were obtained, with maximum values of $J_c^{sf}$ (77 K) = 6.6 and 6.9 MA/cm$^2$ for CTA and FH samples, respectively. The behavior shown in the superconducting performance of Ba-deficient samples grown at different temperatures is clearly different to the one observed on conventional stoichiometric YBCO films. In the former a $J_c^{sf}$ peak is observed, while in the latter $J_c^{sf}$ increases until a plateau of optimal epitaxial growth is reached [187].

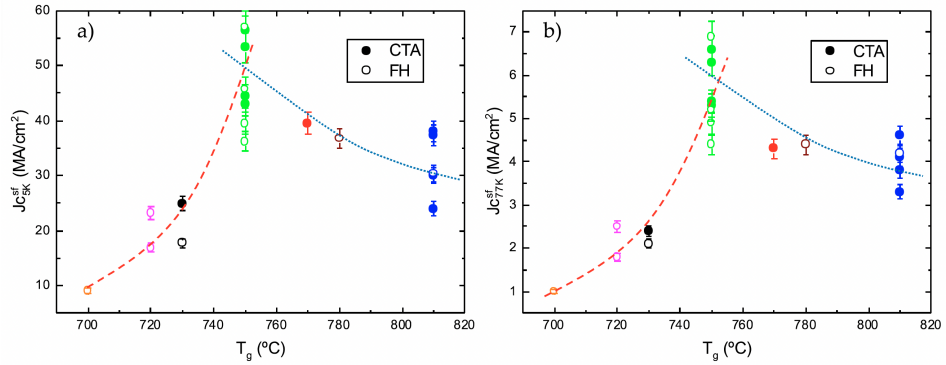



Figure 3.7: Self-field $J_c$ as a function of the growth temperature for samples grown by CTA (closed symbols) and FH (open symbols) at (a) 5 K and (b) 77 K. The wider scattering of data points at 750 °C and 810 °C comes from the fact that a large number of samples were tested at those temperatures. Dashed and dotted lines are provided as a guide.

It is important to note, moreover, that in order to obtain high $J_c^{sf}$ values in the range of 5 MA/cm$^2$ with standard (non-Ba-deficient) precursor solutions, a much higher $T_g$ (810 °C) is needed [131, 190]. We can thus conclude that Ba-deficiency solutions enable to grow very high critical current density films at reduced temperatures of 750 °C on LAO substrates. This seems to indicate that the percolating currents along the low angle grain boundary network of the YBCO films are optimized at lower temperatures in Ba-deficient YBCO films [182].

The magnetic field dependence of $J_c$ at 5 K for samples grown at different temperatures is plotted in Fig.3.8(a). It is well-known that the log–log plot of the $J_c(H)$ dependence of YBCO thin films shows two different regions [72]. At low fields, where the number of vortices is less or equal to the number of defects, there is a plateau of $J_c$ as-

sociated with the single vortex pinning regime. At intermediate fields, where the number of vortices is equal to or greater than the number of defects, the vortex–vortex interactions become relevant, resulting in a decrease of $J_c$, and a collective vortex motion is governed by a power law regime. The transition from single vortex to collective pinning regimes is defined by the crossover field $H^*$, which in our case was determined at 90 % of self-field $J_c$.

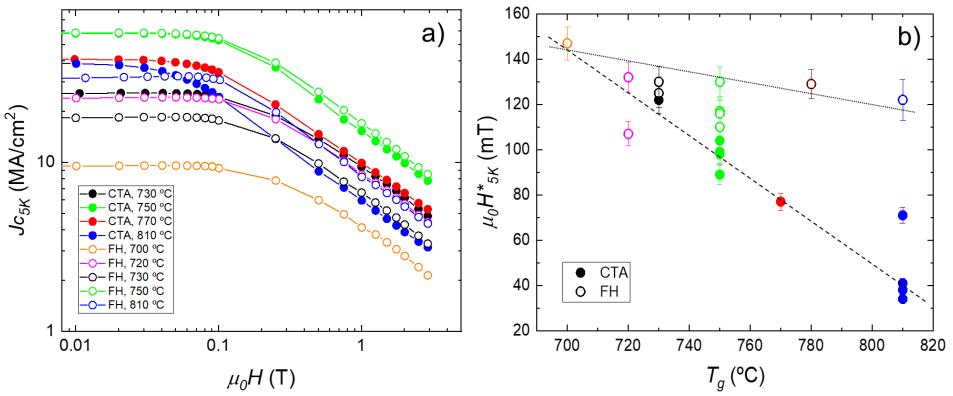



Figure 3.8: $J_c$ behavior with magnetic field for samples grown with the CTA method (closed symbols) and the FH method (open symbols): (a) $J_c$ as a function of the magnetic field at different growth temperatures, (b) $\mu_0 H^*$ values determined at 5 K as a function $T_g$.

Fig.3.8b shows the $\mu_0 H^*$ values obtained for the different films as a function of $T_g$. Samples grown by the CTA method show a clear trend with a continuous enhancement of $\mu_0 H^*$ by reducing the growth temperature, indicating that more pinning centers are induced as we decrease $T_g$. In the case of FH films, although a slight enhancement of $\mu_0 H^*$ is observed at low $T_g$, a clear tendency cannot be identified. For those samples, the value of $\mu_0 H^*$ is already very high at $T_g = 810$ °C, thus pointing out that the higher nucleation rate of FH process also helps to induce pinning defects within the matrix, which are not present with CTA growth [138].

The effect of rapid annealing on the defect structure and final properties of different functional materials has also been reported [61, 191]. Fig.3.9a shows the temperature dependence of $J_c^{sf}$ for CTA and FH YBCO layers grown at different $T_g$. The $J_c(T)$ curves have been used to evaluate the contribution of strong and weak pinning centers, by

fitting their expected $J_c(T)$ dependences [58] (see section 1.2). Strong pinning shows a smooth decay with temperature (Eq.1.19) [11], while weak pinning is characterized by a fast $J_c$ decay with temperature (Eq.1.18) [83].

Fig.3.9b shows the contribution of $J_c$ associated with strong pinning defects at 0 K, obtained by fitting equations 1.18 and 1.19 in the curves depicted in Fig.3.9a. We observe that samples grown at 810 °C show a similar weight of strong and weak contributions ($\sim$ 50 - 60 % of strong pinning). However, when reducing the growing temperature, the contribution of strong pinning increases, completely dominating the pinning landscape in samples grown at 700 °C (90 % of strong pinning).

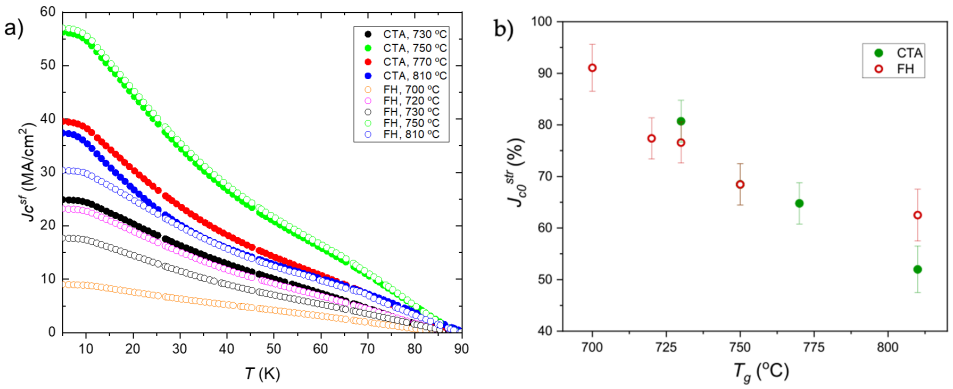



Figure 3.9: a) Self-field critical current density $J_c$ values as a function of the temperature for samples grown with the CTA method (closed symbols) and the FH method (open symbols) (b) Percentage of strong pinning contribution to $J_c$ at 0 K, determined by fitting the $J_c(T)$ curves shown in (a) with equations 1.18 and 1.19.

These results indicate that, as previously observed in the $J_c(H)$ dependence, the growing temperature strongly affects the pinning landscape generated within the YBCO matrix. Considering the results obtained in other CSD films and nanocomposites studied in the group, an enhancement of $\mu_0 H^*$ and isotropic strong pinning contribution can be correlated with the presence of stacking faults and associated nanostrain [83, 137, 138, 192]. In order to elucidate the nature of pinning centers in Ba-deficient films grown at low temperature we have performed angular field dependent $J_c$ measurements at different temperatures together with an advanced TEM micro-structural imaging.

## 3.5 Pinning landscape of YBCO thin films grown at low temperatures

In this section we will study the angular magnetic field and temperature dependence of $J_c$ on patterned samples using the template shown in Fig.3.1. We compare four YBCO films; two stoichiometric YBCO samples (a pristine standard film (Stoich-810) and a nanocomposite (Stoich-NC-810) both grown at 810 °C), and two Ba-deficient samples grown by CTA (a film grown at 810 °C (LowBa-810), and another one grown at the optimized temperature of 750 °C (LowBa-750)).

A comprehensive discussion of artificially engineered pinning sites induced in YBCO nanocomposites with different nature and amount of nanoparticles (BHO, $BaZrO_3$, $Ba_2YTaO_6$ and $Y_2O_3$) can be found in [193]. In this work we aim to analyze the superconducting performance and associated pinning landscape in pristine Ba-deficient YBCO films grown at low temperatures. We use a stoichiometric pristine and a typical nanocomposite film grown at 810 °C for comparison purposes.

### 3.5.1 Magnetic field dependence of $J_c$ at $H//c$

Fig.3.10 shows the critical current density as a function of the magnetic field $H//c$ for these four samples at 77 K, 65 K, 50 K and 5 K, in a log-log scale. The first thing that one can observe is that the $J_c(H)$ curves obtained for pristine stoichiometric and the Ba-deficient sample grown at 810 °C are almost identical in all temperatures, indicative of a minor effect of the precursor solution used. It should be noted however that the growth temperature has a strong effect on the pinning performance.

LowBa-750 shows a smoother $J_c(H)$ dependence at all four temperatures, similar to what we obtain in the nanocomposite film grown at 810 °C by introducing artificial pinning centres (BHO nanoparticles). So, we observe that efficient pinning sites can be naturally induced within the YBCO matrix by reducing the growth temperature, without the need to artificially introduce secondary phases. It should be noted that although both Stoich-NC-810 and LowBa-750 samples show similar performance at 77 K, 65 K and 50 K, there are crossovers of the $J_c(H)$ curves at 0.378 T, 0.385 T and 0.287 T, respectively. LowBa-750 shows a better self-field critical current density but a slightly faster

$J_c$ decay with the magnetic field, indicating that different defects are induced in the two samples.

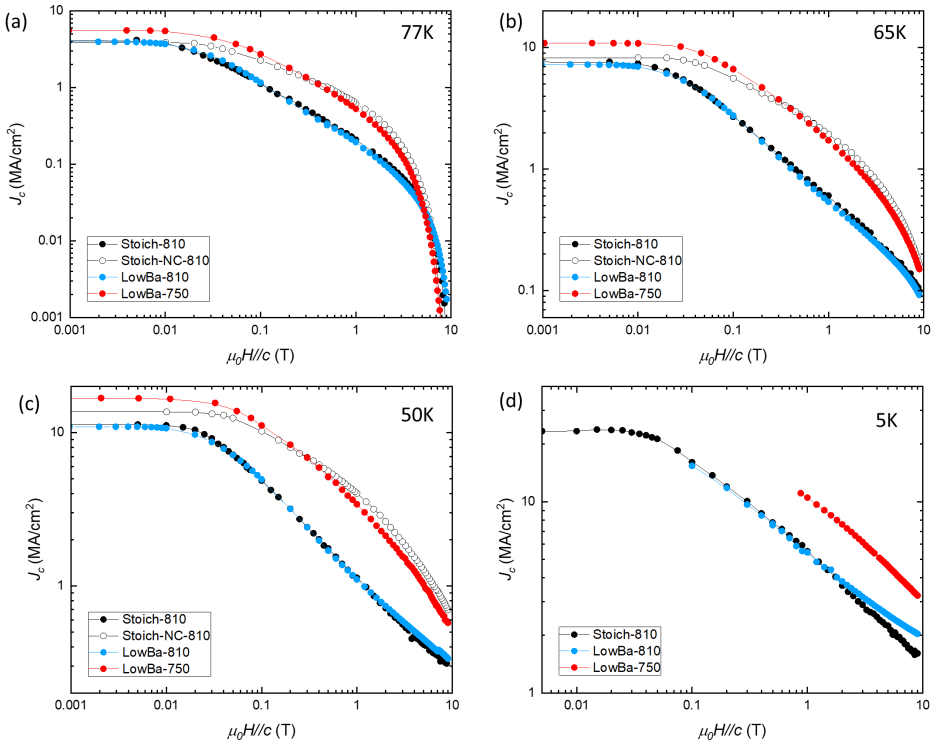



Figure 3.10: Critical current density values as a function of the applied magnetic field $H//c$ for samples: Stoich-810 (closed black dots), Stoich-NC-810 (opened black dots), LowBa-810 (closed blue dots) and LowBa-750 (closed red dots) at different temperatures: a) 77 K, b) 65 K, c) 50 K and d) 5 K.

### 3.5.2 Angular magnetic field dependence of $J_c$

Fig.3.11 shows the angular dependence of $J_c(\theta)$ obtained at different magnetic fields and at 77 K, 65 K and 5 K, for Stoich-810, Stoich-NC-810 and LowBa-750. By comparing the nanocomposite and the pristine sample grown at 810 °C (black open and closed symbols, respectively) we observe that effect of adding nanoparticles results in a broader *ab*-peak ($\theta = 90°$), attributed to the anisotropic pinning of stacking faults and higher values of $J_c$ in the whole $\theta$ range, with a reduction of the anisotropy associated with the isotropic pinning of nanostrained regions induced at the partial dislocations at different

fields and temperatures [61, 83, 194]. The $J_c(\theta)$ curves obtained for the pristine Ba-deficient sample grown at 750 °C (red symbols) show similar characteristics than that of the nanocomposite but with even much broader *ab*-peaks in all graphs.

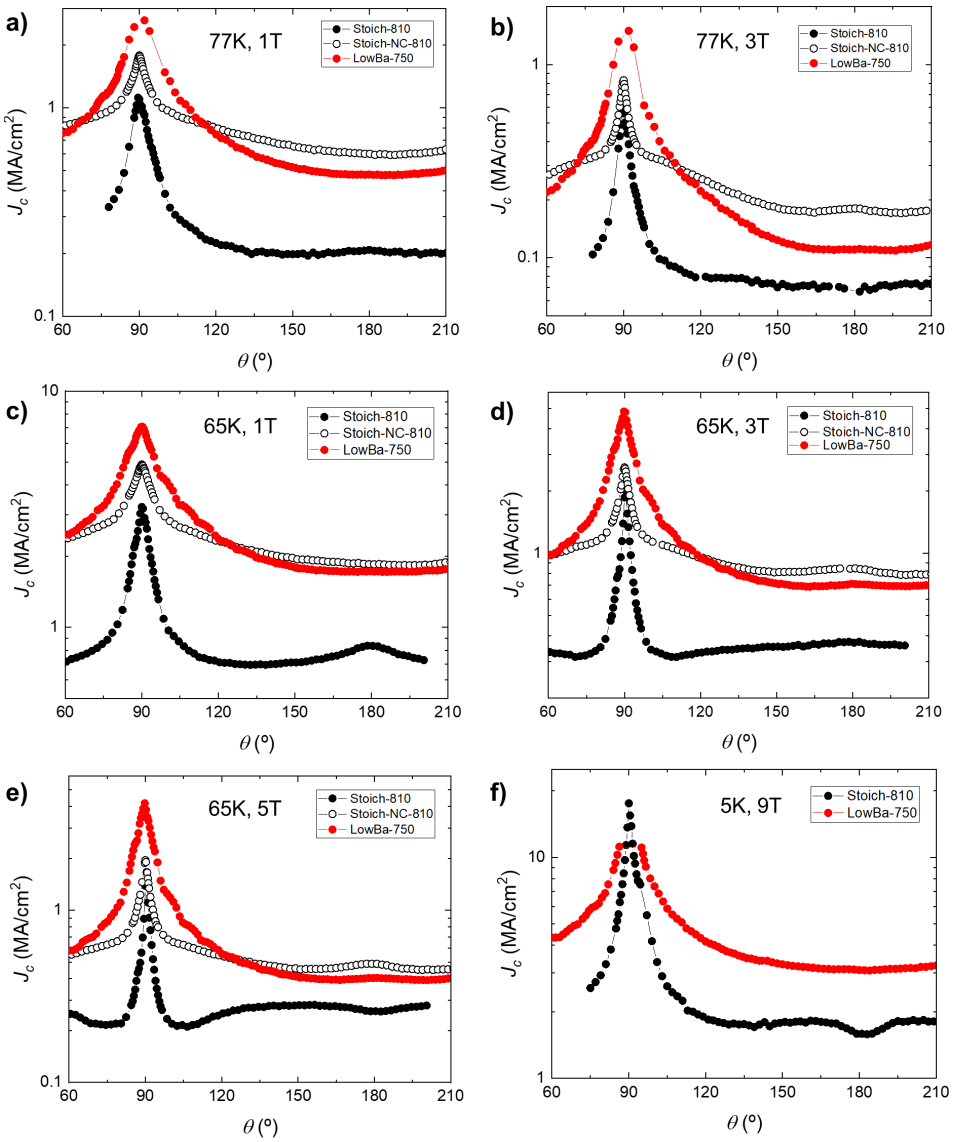



Figure 3.11: Angular dependence of the critical current density for samples Stoich-810 (closed black dots), Stoich-NC-810 (open black dots) and LowBa-750 (closed red diamonds) at a) 77 K and 1 T, b) 77 K and 3 T, c) 65 K 1 T, d) 65 K and 3 T, e) 65 K and 5 T, and f) 5 K and 9 T.

In general, in YBCO films the anisotropic pinning at $H//ab$ mainly comes from the interplay between intrinsic pinning and stacking faults. The width of the $J_c(\theta)$ $ab$-peak can be associated to the trapping angle $\theta_T$ that limits the staircase regime where vortices accommodate to the anisotropic defects with kinks and parallel segments [195, 196]. Beyond $\theta_T$ vortices will be straight and take the direction of the applied field, thus being unaffected by the correlated nature of the anisotropic pinning. In all temperatures, LowBa-750 sample shows higher $J_c$ values at $H//c$ than Stoich-810 and similar to the Stoich-NC-810 sample.

Fig.3.12 shows the normalized ab-peak measured at different magnetic fields and temperatures for the LowBa-750 sample. Note that the width of the peak decreases as the field increases tending to a saturation at high fields in all temperatures.

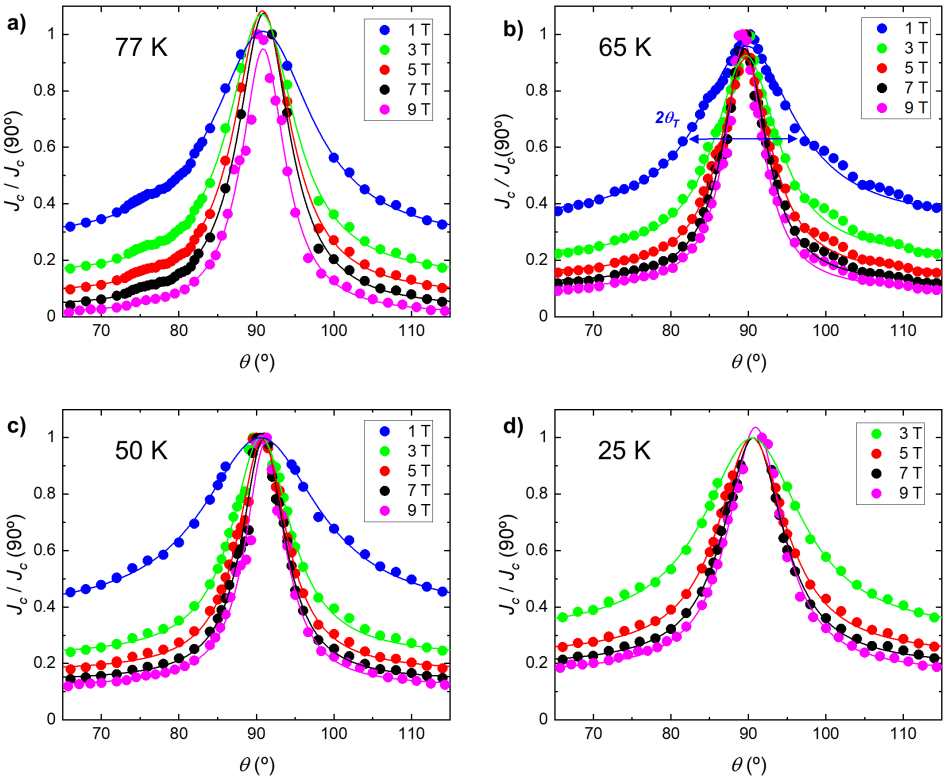



Figure 3.12: Angular dependence of the normalized critical current density for different magnetic fields of the LowBa-750 sample at 90° and a) 77 K, b) 65 K, c) 50 K and d) 25 K.

Solid lines are fits with the shape of Lorentzian peak function, with bell shape and much wider tails than Gaussian function. It is expressed as:

$$y = y_0 + \frac{2A}{\pi}\frac{w}{4\left(x - x_c\right)^2 + w^2} \tag{3.1}$$

where $w = 2\theta_T$ is the full with half maximum (FWHM), $A$ is the Area, $x_c$ is the center and $y_0$ is the offset. The FWHM has been used to evaluate the trapping angle, $\theta_T$ (see Fig.3.12b).

Field dependence of the trapping angle obtained for Stoich-810, Stoich-NC-810, and LowBa-750 at 77 K and 25 K is shown in Fig.3.13. For both temperatures, the values of the trapping angle obtained for Stoich-NC-810 and LowBa-750 samples are much higher than those for Stoich-810, indicating that one can promote the formation of stacking faults either by introducing nanoparticles in a nanocomposite film or by reducing the growth temperature in a pristine film.

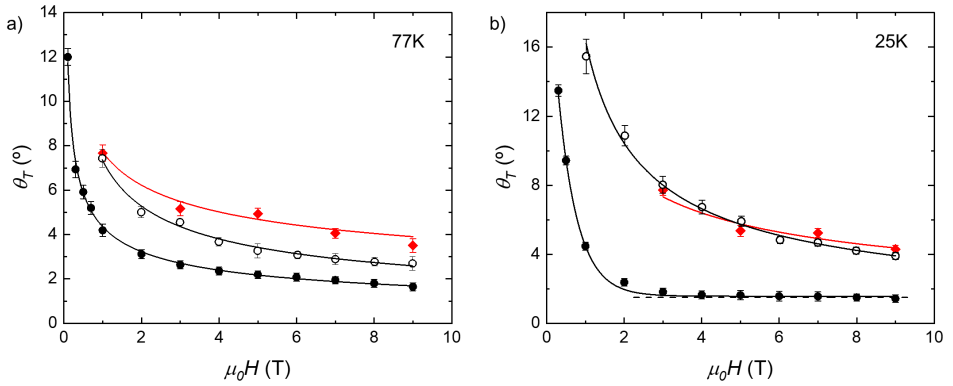



Figure 3.13: Magnetic field dependence of the trapping angle ($\theta_T$) of different samples: Stoich-810 (closed black dots), Stoich-NC-810 (open black dots), LowBa-750 (closed red diamonds) at a) 77 K and b) 25 K. Dashed line is a guide to the eye to highlight the field independent $\theta_T$ region.

It is worth noting that at lower temperatures (Fig.3.13b) the pristine stoichiometric sample grown at 810 °C (Stoich-810) shows a fast $\theta_T$ decrease with $H$ and becomes constant above $\sim 4$ T (at 25 K). Field independent $\theta_T$ can be associated with a single vortex pinning regime mainly dominated by intrinsic pinning with a very large matching field

[195]. Samples with a high number of staking faults (Stoich-NC-810 and LowBa-750) do not reach the $\theta_T$ saturated region fingerprint of an extension of the pinning region dominated by stacking faults.

### 3.5.3 Nature and strength of pinning centres

To better elucidate the nature and strength of pinning sites induced in the Ba-deficient pristine YBCO film grown at 750 °C we analyse the contribution of different types of defects at different regions of the $H$ - $T$ phase diagram. A first classification of pinning centres may be performed considering their temperature dependence of the critical current density, $J_c(T)$ (see Fig.3.8 and associated text).

Another classification may be performed considering their shape. Isotropic pinning sites, with a pinning length that does not depend on the magnetic field orientation, and anisotropic pinning sites which are correlated along a certain field direction. These two kinds of defects may be identified through angular magnetic field $J_c$ measurements, by using the Blatter scaling approach on a series of $J_c(\theta, H)$ curves plotted as a function of the effective magnetic field, $H^{eff}$ (eq.3.2 [51].

$$H^{eff} \sim H\varepsilon(\theta) = H\sqrt{\frac{sin^2(\theta)}{\gamma^2} + cos^2(\theta)} \tag{3.2}$$

where $\theta$ is the angle between the magnetic field and the $c$-axis and $\gamma$ the anisotropy parameter.

By combining eq.1.18 – 3.2 and adjusting angular, field, and temperature dependence of $J_c(H, T, \theta)$, assuming a direct summation of pinning centres, one can determine and quantify three different pinning contributions as commented in Chapter 1: isotropic-weak (I-W), isotropic-strong (I-S), and anisotropic-strong (A-S) [90].

Fig.3.14 plot log $J_c$ versus $T^2$ at $\mu_0 H//c = 1$ T, $\mu_0 H//c = 9$ T and $\mu_0 H//ab = 9$ T. Linear fits to these plots correspond to strong pinning centres (eq.1.19) which control $J_c$ in the intermediate temperature regime. At low temperatures, for $H//c$ the $J_c$ values of Stoich-810 and Stoich-NC-810 deviate from the linear fit below $\sim$ 30 K at 1 T and 20 K at 9 T pointing out a region dominated by weak pinning defects [61].

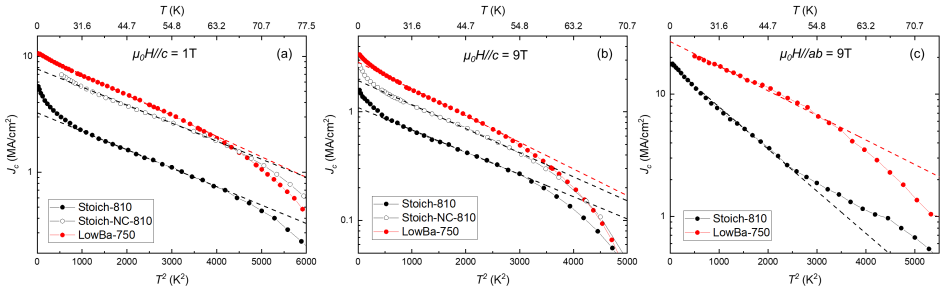



Figure 3.14: Log $J_c$ versus $T^2$ at a) 1 T, $H//c$, b) 9 T, $H//c$ and c) 9 T, $H//ab$, measured for Stoich-810, Stoich-NC-810 and LowBa-750.

In the case of LowBa-750, the linear dependence is observed down to lower temperatures, indicating that strong pinning centres control the pinning performance in a wider temperature region: 5 K – 60 K at 1 T and 15 K – 55 K at 9 T. At this low-intermediate temperature regime, this sample shows the best $J_c$ performance. At high temperatures, a fast decay of $J_c$ is obtained in all the samples due to thermal fluctuations close to $T_c$. As pointed out above a crossover of the $J_c(T)$ curves of Stoich-NC-810 and LowBa-750 is obtained at 68 K – 1 T and 65 K – 9 T $H//c$ which may be associated to a slightly higher irreversibility line of the former [61].

In Fig.3.15 we show the weights of the three basic pinning contributions of $J_c(T)$ for LowBa-750. At intermediate fields, $\mu_0 H//c = 1$ T, the most important contribution comes from I-S pinning which can be associated to nanostrain induced to accommodate the stacking faults [83]. At higher fields, $\mu_0 H//c = 9$ T, we observe that an important contribution of I-W defects appears at low temperatures.

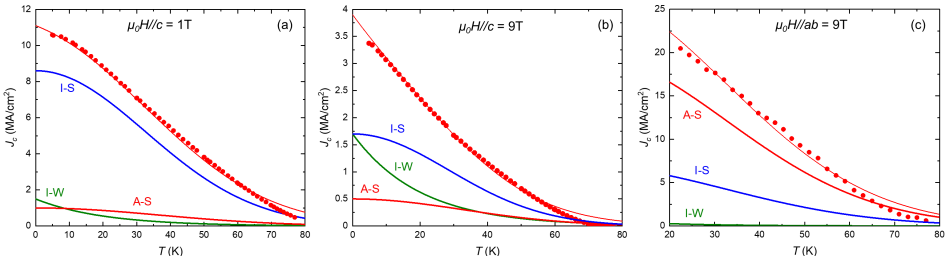



Figure 3.15: a), b), and c) show the temperature dependence of the weight of anisotropic-strong (A-S), isotropic-strong (I-S) and isotropic-weak (I-W) critical current density contributions for the LowBa-750 sample, respectively.

These defects may be associated to Cu–O cluster vacancies appearing at the intergrowths [197]. At $\mu_0 H//ab = 9$ T the A-S contribution coming from stacking faults is clearly governing the pinning performance.

Fig.3.16 shows cross-section HAADF STEM images obtained for LowBa-750 at different magnifications, where we clearly observe the presence of a huge density of stacking faults as compared with a stoichiometric pristine film, where for a $200 \times 200$ nm$^2$ cross-section image less than 20 stacking faults are found [61]. These images confirm that the defects naturally created by reducing the temperature are stacking faults.

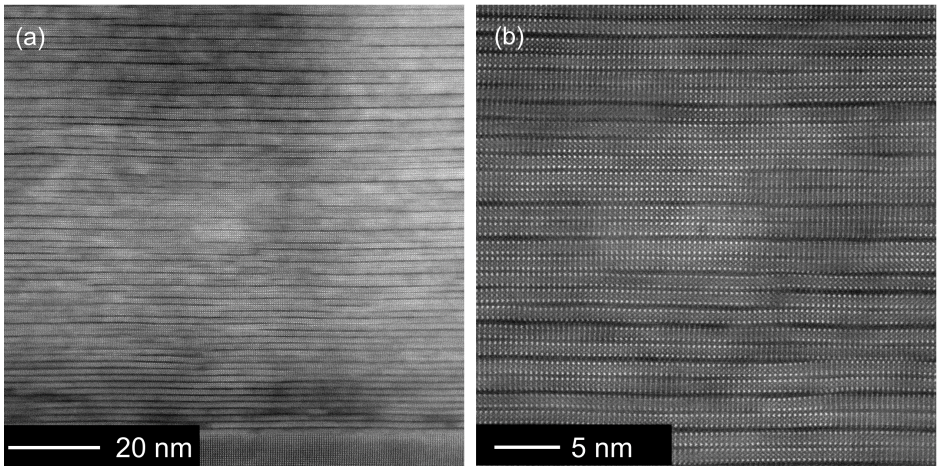



Figure 3.16: HAADF-STEM cross sections obtained for LowBa-750 at different magnifications. The dark horizontal stripes in the images correspond to stacking faults (Y124 intergrowths).

## 3.6 Influence of the carrier density on Jc

In addition to the effect of the vortex pinning landscape, the superconducting properties of cuprates, strongly depend on the carrier concentration. In particular, the critical current density can be significantly enhanced by achieving the overdoped state due to an increase in the condensation energy [96, 198].

Fig.3.17b shows the average values of the self-field critical current density as a function of their carrier density, $n_H$, obtained for several pristine stoichiometric films grown at 810 °C (four samples) and Ba-deficient films grown at 810 °C (three samples) and 750 °C (four samples). The $n_H$ value obtained for standard films grown at 810 °C with stoichiometric TFA solution with $J_c^{sf} \sim 4$ - 5 MA/cm$^2$ is the one expected for optimally doped films $n_H \sim 8{\cdot}10^{21}$ cm$^{-3}$ [199]. Three examples of the slopes obtained through Hall measurements to calculate $n_H$ of each type of sample, are shown in Fig.3.17a.

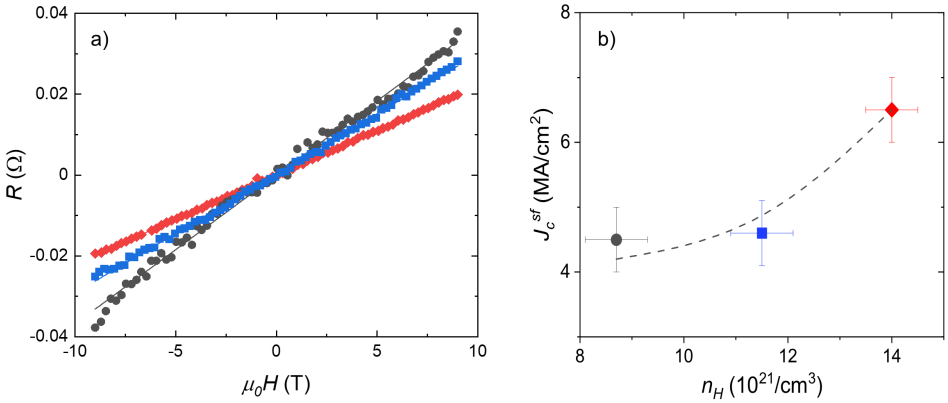



Figure 3.17: a) Hall resistance as a function of the magnetic field obtained at 300 K for pristine stoichiometric films (closed black dots), Ba-deficient films grown at 810 °C (closed blue squares) and Ba-deficient films grown at 750 °C (closed red diamonds). b) Self-field critical current density values at 77 K as a function of the carrier density obtained for same samples.

For the films grown with Ba-deficient solution however, we observe that the values of $n_H$ appear at the overdoped region. Films grown at 810 °C show similar $J_c^{sf}$ values than those obtained for standard stoichiometric but slightly higher $n_H \sim 11{\cdot}10^{21}$ cm$^{-3}$. Interestingly, Ba-deficient films grown at 750 °C show the highest charge carrier density with $n_H \sim 14{\cdot}10^{21}$ cm$^{-3}$ and large values of $J_c^{sf} \sim 6 - 7$ MA/cm$^2$ can be obtained. The enhancement of the carrier density, and associated $J_c^{sf}$, can be correlated with a high density of stacking faults, suggesting that the induced disorder and nanostrain within the YBCO matrix may enhance the oxygen diffusion thus allowing to easily achieve an overdoped state.

## 3.7 Conclusions

In this chapter, we evaluated the effect of the growing temperature on the superconducting performance of YBCO films grown by Ba-deficient low-fluorine solutions using two different approaches, conventional thermal annealing (CTA) and flash heating (FH). The obtained results demonstrate that in both cases, substantial improvements can be obtained by using Ba-deficient solutions, which allow us to reduce the growth temperature of YBCO films.

Samples grown at lower $T_g$ show smoother $J_c(H)$ dependencies, with higher $\mu_0 H^*$ values, and strong pinning contribution, which indicate that a higher density of defects is achieved in the YBCO matrix. A good compromise between epitaxial growth, with optimized current percolation, and pinning performance gives us an optimum $T_g = 750$ °C, where high self-field $J_c$ values are obtained (7 MA/cm$^2$ at 77 K). The use of lower growth temperatures, as compared with stoichiometric YBCO films, may be also helpful when growing on top of technical substrates, preventing chemical reaction with substrate buffer layers.

The pinning performance of Ba-deficient samples grown at low temperature (750 °C) has been characterised through transport measurements and compared with a standard pristine film and a nanocomposite with BHO nanoparticles grown at a higher temperature (810 °C). The results show that by reducing the growth temperature very high self-field critical current density values are obtained with smooth $J_c(H)$ dependences similar to those obtained in nanocomposites.

By measuring the temperature, field, and angular dependence of $J_c$ we have found that a highly effective pinning landscape is induced in the films grown at 750 °C mainly associated to the formation of a large number of stacking faults, observed by TEM images. Moreover, those films show very high values of $J_c^{sf}$ which may be associated to a large carrier concentration at the overdoped state.

Consequently, the use of Ba-deficient solutions showing a large $c$-axis epitaxial YBCO growth window appears as a very appealing way to tune both the pinning landscape and the carrier density of YBCO pristine films and thus maximize their superconducting performance. It is worth pointing out that the addition of nanoparticles in the YBCO

matrix not only generates pinning due to induced stacking faults and the associated strain but it is also possible to achieve a synergetic effect, with additional pinning coming from small nanoparticles [137, 200]. Thus, the combined effect of Ba-deficient precursor solution, low temperature growth and the addition of small nanoparticles may boost the pining performance of the films.

# Chapter 4

# Electric field-induced oxygen doping in YBCO films

Today advances to store and analyse massive information offer huge opportunities and unprecedented benefits in business, healthcare, security, or society, but require to explore novel technologies for information storage and processing in a sustainable way. Among many different approaches, strongly correlated oxides are particularly interesting materials for emerging electronic devices due to their rich phase diagram with transitions between competing phases showing dramatically different electronic and magnetic properties [95].

In particular, metal–insulator transitions (MITs) can be exploited to induce a non-volatile reversible switch between different resistance states induced by an electric field [105]. In simple terms, resistive switching (RS) devices based on strongly correlated oxides display significant resistance variations caused by small carrier concentration modulations driven by an electric field, enabling the stabilization of non-volatile multilevel analogic states [108].

Although the underlying mechanisms behind RS phenomena are complex and dependent on the specific materials involved, in oxide systems, the switching behaviour is often associated with the movement of oxygen vacancies [109]. This movement can manifest as a metallic filament embedded within an insulating matrix [109], modification of a Schottky barrier at the contact interface [110], or due to a homogeneous switch through the material volume [111–114].

Particularly interesting is the modulation of the non-volatile MIT in cuprate superconductors $YBa_2Cu_3O_{7-\delta}$ (YBCO) where both the normal state resistance and the superconducting critical temperature can be reversibly manipulated in confined active volumes by field-induced electrochemical oxygen doping [115, 125] or electromigration effects [97, 123, 124, 201]. Fine-tuning of the oxygen doping through voltage pulses of electric current allows to explore the electrical transport properties of complex phases appearing in the doping phase diagram of cuprates [97, 123, 125].

In this work, we use field-induced resistive switching effects to study the critical current density performance of YBCO films at different oxygen doping levels. The effect of oxygen doping on the magnetic field and angular dependence of the critical current density may be of great relevance for the optimization of flux pinning through microstructural modification [43, 96, 198]. Here we are able to selectively tune the doping level of superconducting tracks by applying voltage pulses.

Moreover, YBCO films of different thicknesses are studied to see the contribution of the critical temperature, the pseudogap temperature and their corresponding oxygen doping. It is important to analyze these parameters to try to complete, enhcance, and understand more all the phases involved in the phase diagram of cuprate superconductors.

The effect of field-induced oxygen doping is studied by measuring the critical temperature, carrier density, and critical current density at different doping levels. Transmision electron microscopy experiments performed at low and high resistive states indicate the generation of a large amount of $YBa_2Cu_4O_7$ (Y124) intergrowths with a high density of oxygen vacancies. A clear correlation between the microstructure with the magnetic field and angular dependencies of the critical current density is obtained.

## 4.1 Oxygen doping in YBCO films of different thickness

In this first section, we will analyze YBCO layers of different thicknesses by measuring the critical temperature and the carrier concentration $n_H$. Epitaxial $YBa_2Cu_3O_{7-\delta}$ (YBCO) thin films of thicknesses of 10 nm, 15 nm, 20 nm, 30 nm, 50 nm, 100 nm, and 250 nm were grown by pulsed laser deposition (PLD) on (001)-$LaAlO_3$ (LAO) single-crystal substrates. Substrates were heated up to $T$ = 800 - 810 °C, with an $O_2$ partial pressure of 0.3 mbar during the deposition and a fixed target-substrate distance of 52.5 mm. A high fluence laser (around 2 J/cm$^2$) working at a frequency of 5 Hz was used. During the cooling ramp, we increase the P($O_2$) in the chamber in order to obtain well-oxygenated samples. The thickness of the film is mainly determined by the number of pulses considering 26 pulses for 1 nm and checked in the profilometer. For these samples, we obtained the mentioned thicknesses using 260, 390, 520, 780, 1300, 2600 and 6500 pulses, respectively.

YBCO devices were patterned with specially designed contact paths depicted in Fig.4.4 and explained in detail in the next section. First, the resistance dependence on the temperature was measured using the 4-point configuration method. Figure 4.1 shows the linear and log-scale normalized (at 300 K) mentioned dependence for each thickness.

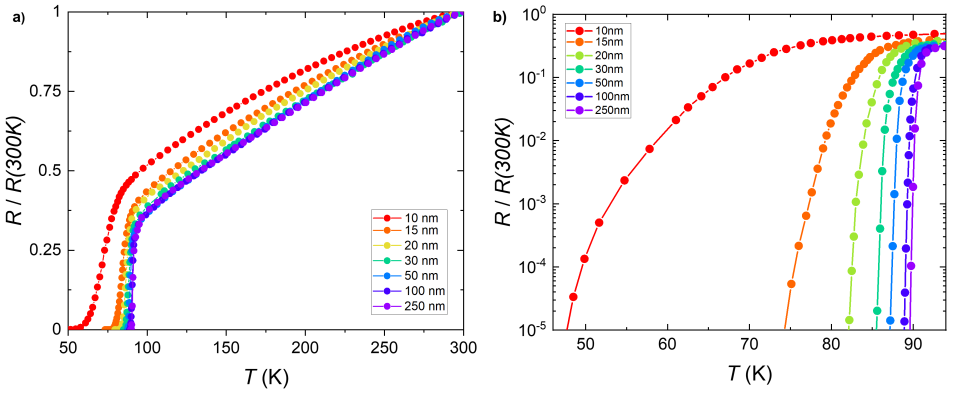



Figure 4.1: a) Linear and b) log-scale normalized resistance as a function of temperature from different thickness samples ranging from 10 nm to 250 nm.

As the thickness is reduced we clearly see that the linearity of the values from 100 K to 300 K is also reduced. Besides, the transition to the superconducting state is sharper and narrower as the thickness is increased, meanwhile for the 10 nm sample this transition is broader.

We chose a criterion of $T_c$ when $R\ /\ R(300K) = 10^{-3}$, as explained in section 2.4. The carrier concentration at 300 K for these samples was obtained through Hall measurements as commented in the same section in Chapter 2. Graphs showing the relation of $T_c$ and $n_H$ for different thicknesses, $t$, are displayed in Fig.4.2.

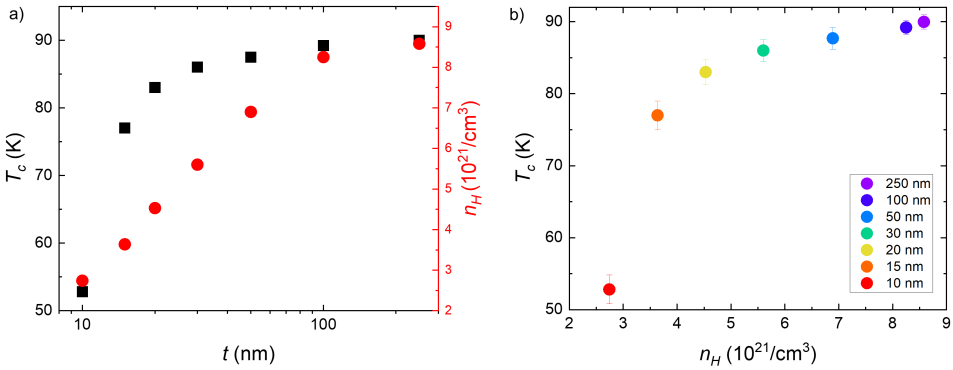



Figure 4.2: a) thickness dependence of the critical temperature, $T_c$ (black squares, left axis), and carrier density $n_H$ (red dots, right axis). b) $T_c$ vs. $n_H$ for samples of different $t$.

A clear trend is observed where $T_c$ decreases with decreasing the thickness. Samples with $t$ = 250nm, 100nm are optimally doped samples with $T_c \approx 90$ K. As we reduce he thickness we observe that both $T_c$ and $n_H$ decrease reproducing the superconducting dome expected for underdoped samples (Fig.1.16). It should be noted that values of $T_c$ close to 80 K are obtaned for samples of 15 nm indicating a very good epitaxial growth. Samples with 10nm are highly underdoped ($n_H$ = 2.72 $\cdot 10^{21}$ cm$^{-3}$) showing low values of $T_c$ = 52.8 K.

The obtained thickness dependence may be related with the strain induced through the substrate, which would be higher as the thickness is reduced, meanwhile dislocations and other growth defects generated in the film could relieve this strain [202, 203]. For the thinnest film, the low $T_c$ obtained can also be due to a lose in the interlayer coupling [204, 205]. In addition, epitaxial strain may contribute to cation disorder

and cause a $T_c$ decrease that would not be present in well-annealed bulk material.

Another parameter that we can extract from the previous measurements is the pseudogap temperature, $T^*$. Considering the phase diagram of cuprate superconductors, it represents the crossover line between the pseudogap region and the still poorly understood strange metal phase (see Fig.1.16). Since the latter one is characterized by a linear dependence of the resistance versus temperature, $T^*$ can be inferred by the departure from the linear $R(T)$ behavior [206], that means the temperature at which the behaviour loses linearity starting at 300 K .

In Fig.4.3a it is shown the linear normalized resistance dependence with the temperature for two different thicknesses (10 nm and 250 nm). As commented before, thicker samples, that have higher $T_c$ values, have more linearity between 100 K and 300 K (fitted lines). Therefore the extracted values of $T^*$ are higher for thinner samples, as it is expected for underdoped samples.

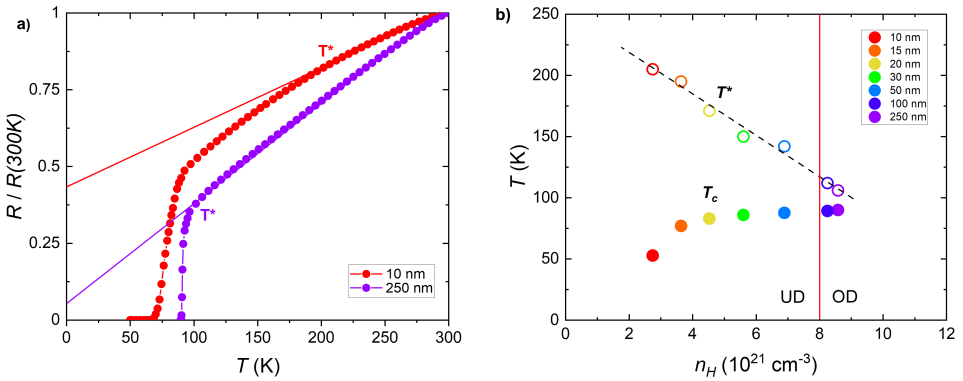



Figure 4.3: a) Linear normalized resistance as a function of temperature from different thickness samples. Added lines shows the linear behaviour where $T^*$ can be extracted. b) Phase diagram for YBCO showing the values of $T_c$ and $T^*$, as a function of $n_H$.

Fig.4.3b shows the values of $T_c$ and $T^*$ obtained for samples of different thickness as a function of $n_H$ to get the Temperature-Doping phase diagram of the films which is in qualitative agreement with the expected for cuprate films (Fig.1.16).

## 4.2 Device fabrication

YBCO devices of different thicknesses were patterned with specially designed contact paths enabling the modulation of oxygen doping in a localized parts of a track through a gate contact ($G$ in Fig.4.4a).

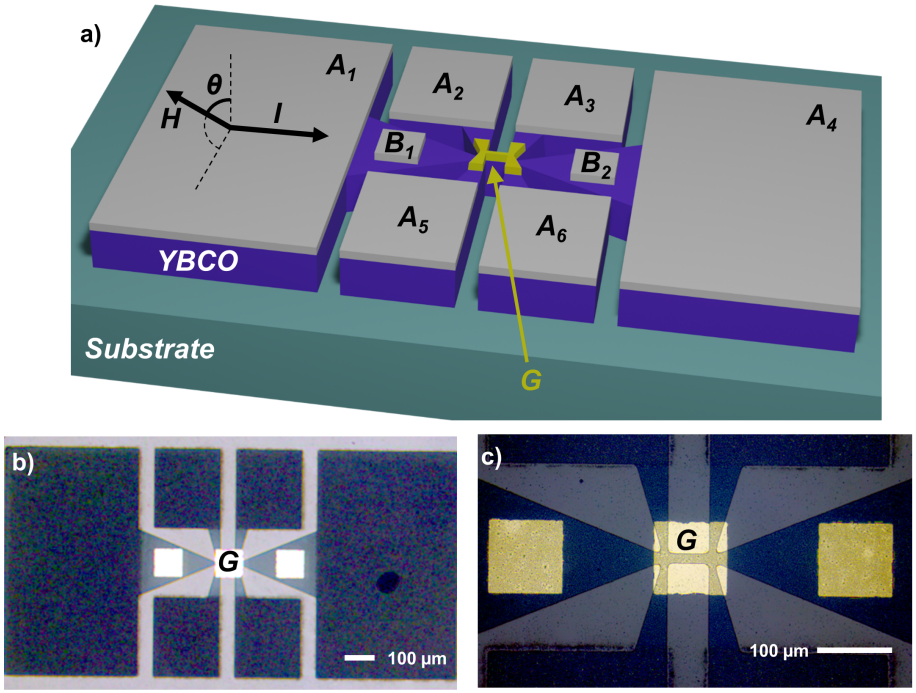



Figure 4.4: a) Schematic representation of the measurement configuration. Gate contact (G) used to induce the switching effect is depicted in yellow. b) and c) Optical images of a YBCO device with uniform gate covering the whole YBCO track.

Photolithography combined with sputtering and lift-off were used to deposit 200 nm thick silver contacts on top of large paths which were used to apply current ($A_1$ and $A_4$ of 500 $\mu$m $\times$ 850 $\mu$m) and measure longitudinal and transverse voltage ($A_2$, $A_3$, $A_5$ and $A_6$ contacts, of 250 $\mu$m $\times$ 300 $\mu$m). To ensure good contact resistance, samples were annealed at 450 °C for 1 h. Photolithography and wet etching were used to pattern YBCO tracks of different dimensions, typically width $w \sim$ 10 - 30 $\mu$m and length $l$ = 100 $\mu$m. After the patterning, 50 nm thick small silver contacts ($B_1$, $B_2$) of 100 $\mu$m $\times$ 100 $\mu$m were deposited by sputtering and lift-off.

Finally, a gate contact ($G$) was deposited on top of the YBCO track. Figs.4.4b,c show optical images of one of the measured devices with a top gate of 100 $\mu$m $\times$ 100 $\mu$m.

Additionally, we fabricated gates with different areas by using two different approaches. The first one is by using lines of different dimensions directly sputtered on the track. In order to contact this lines we used 100 $\mu$m $\times$ 100 $\mu$m contacts sputtered at both sides of the track, as shown in Fig.4.5. To avoid damaging of the small central patterns, bounding of the sample was performed at this two connected silver patterns on top of the substrate. As this patterns were done by photolithography we had a resolution limitation and the minimum width of the lines was 5 $\mu$m.

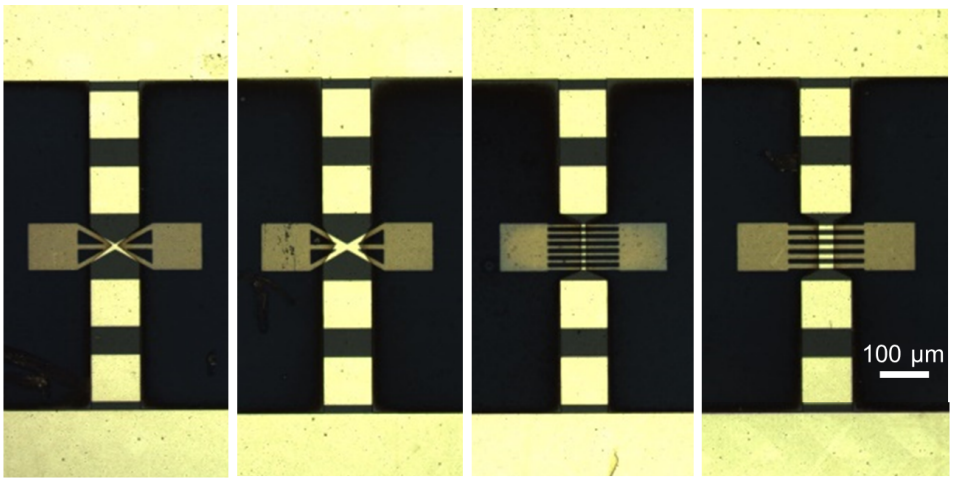



Figure 4.5: Optical images of YBCO devices with different patterned Ag gates on the YBCO track. Dimensions of the lines were 5 $\mu$m and 10 $\mu$m.

The second approach was by adding an intermediate insulating mask of $Al_2O_3$ of 30 nm which was patterned by Electron Beam Lithography, with an array of dots of the desired dimension (Fig.4.6). A top 50 nm silver contact of 300 $\mu$m $\times$ 100 $\mu$m was deposited by sputtering on top of the patterned $Al_2O_3$. In this way, silver only contacted with YBCO in the holes of the insulating layer. Silver was also deposited on the substrate so lateral contacts were used to avoid damaging of the patterned insulating buffer layer while bounding the sample.

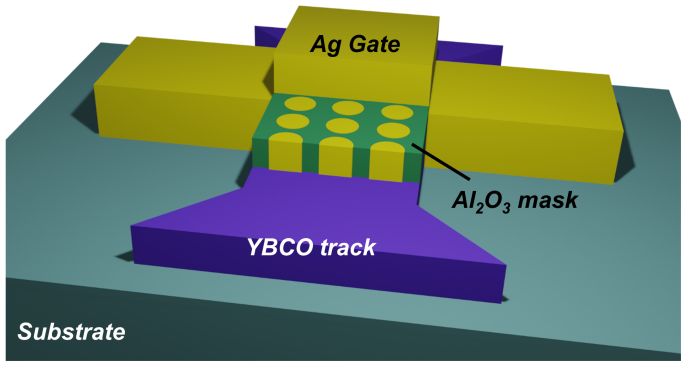



Figure 4.6: Scheme of gate preparation using an insulating $Al_2O_3$ mask on the YBCO patterned device.

Different geometries were patterned in the insulating mask by EBL such as dots, triangles or lines. Figs.4.7a–e show scanning electron microscopy images of $Al_2O_3$ masks patterned with those geometries of different dimensions. Fig.4.7f shows patterned lines, the image was obtained before the insulating film deposition, so it shows the developed resist pattern. The objective of writing these different designs was to see the effect of the area and shape on the switching performance.

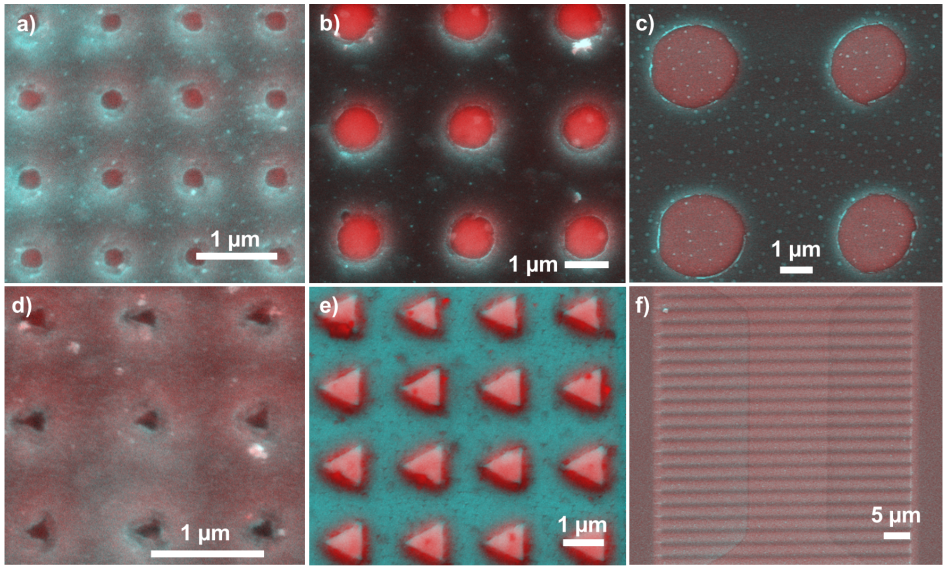



Figure 4.7: SEM images of $Al_2O_3$ masks patterned with a) dots of $d = 300$ nm, b) dots of $d = 1$ $\mu$m, c) dots of $d = 2.5$ $\mu$m, d) triangles of $l = 300$ nm, e) triangles of $l = 1$ $\mu$m and f) resist lines of $w = 2$ $\mu$m separated 1 $\mu$m.

## 4.3 Gate modulation of the RS effect

We first study the resistive switching performance of the YBCO devices at room temperature by applying voltage pulses at gate $G$ by using one of the lateral contacts $B_1$ or $B_2$ (Fig.4.4a) to measure the gate resistance in a two-point configuration, $R^G$. Fig.4.8a shows several $R^G$-$V$ curves obtained in different devices by changing the size of the gate contact. Non-volatile bipolar resistive switching behaviour is found where a transition from a low resistance state (LRS) to a high resistance state (HRS) occurs by applying a negative voltage. The system can be reversibly switched back to the LRS by applying positive voltage.

The main mechanism responsible for the resistance change is the oxygen doping modulation (tunning of $\delta$ in $YBa_2Cu_3O_{7-\delta}$) through field-induced oxygen diffusion [125]. The obtained hysteresis loops are asymmetric with a higher voltage needed to drive the system from the LRS to the HRS than that required to go from the HRS to the LRS, as theoretically predicted considering an asymmetry in the oxygen motion [125]. It is also observed that in general, a progressive resistance change from HRS to LRS is obtained when oxygen is incorporated into the system while a fast transition is produced by oxygen migration.

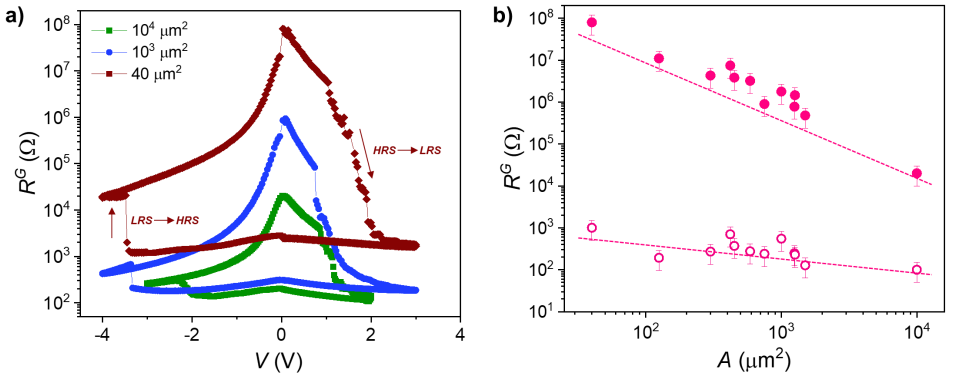



Figure 4.8: Bipolar resistive switching loops of YBCO devices. a) $R^G$-$V$ characteristics of YBCO devices with different gate area. Arrows show the voltage sweep direction in one of the hysteresis loops. b) Evolution of HRS and LRS, obtained measuring at 0.1 V, as a function of the contact area. Error bars correspond to variations of resistance state after different hysteresis loops.

It should be noted that the hysteresis is strongly increased by decreasing the gate area as expected for a volume metal-insulating transition homogeneously occurring below the gate [125]. A very high resistance ratio up to $10^5$ can be obtained in devices with a gate area of 40 $\mu$m$^2$ with a relatively low operation voltage $\sim$ 2–3 V (Fig.4.8b). This ratio, particularly important for memory applications, should be further increased by reducing the gate dimension at the nanoscale.

As commented in the device fabrication section, two approaches were used to reduce the area of the gate. We show several normalized RS loops obtained using both methods in Fig.4.9. They look very similar and both show the expected area dependent behavior.

It is worth mentioning that in the case of using an insulating mask patterned by EBL one can reach higher resistive switching ratios ($\approx 10^5$) since low areas could be patterned. Although a clear trend with the contact area have been obtained, no clear differences were detected by using gates patterned with different shapes.

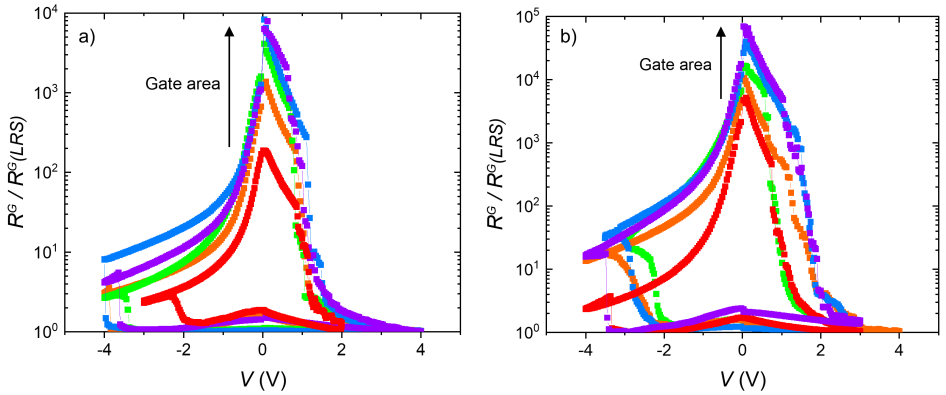



Figure 4.9: Bipolar resistive switching loops, normalized at the LRS obtained for YBCO devices with gates of different areas a) patterned on top of the track and b) using an insulating mask.

Fig. 4.10, shows three consecutive $R$–$V$ hysteresis curves, to illustrate the reversibility characteristics of the switching effect.

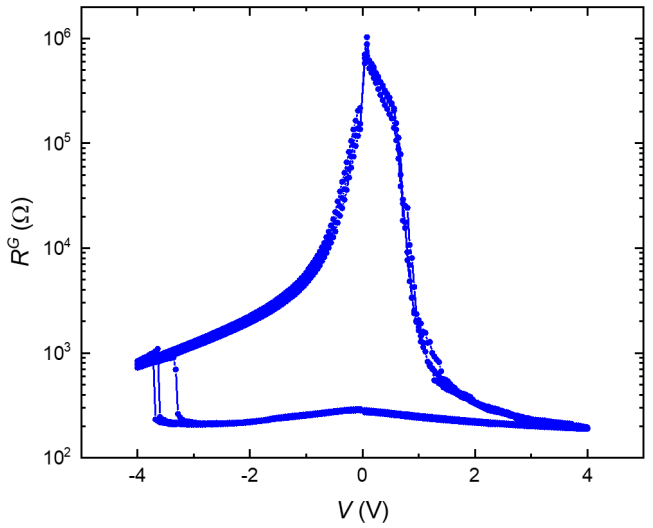



Figure 4.10: Three consecutive Resistive switching loops measured for a sample with a micrometer gate

## 4.4 Gate modulation of the YBCO bridge resistance

An important advantage of generating volume metal-insulating transition homogeneously occurring below the gate is the possibility to design multi-terminal transistor like-devices where the gate may be used to modulate a drain-source channel. In this section we will evaluate the gate-induced resitance change of a YBCO bridge at 300 K, by using a 4-point configuration (Fig.4.11a). To do so, voltage pulses were applied at the gate $G$ by using a lateral contact $B$. Changes in the resistance below the gate after each pulse where tracked by using $A_1$ and $A_4$ to inject the current and measuring voltage between $A_2$ and $A_3$.

In Fig.4.12a we show an example of the percentage change in resistance values across the bridge, after the application of several positive and negative voltage pulses. The resistance variation is determined using eq.4.1, where $R_n$ represents the resistance after a specific voltage pulse, and $R_i$ denotes the initial low state resistance measurement.

$$\Delta R = \frac{R_n - R_i}{R_i} \times 100 \tag{4.1}$$

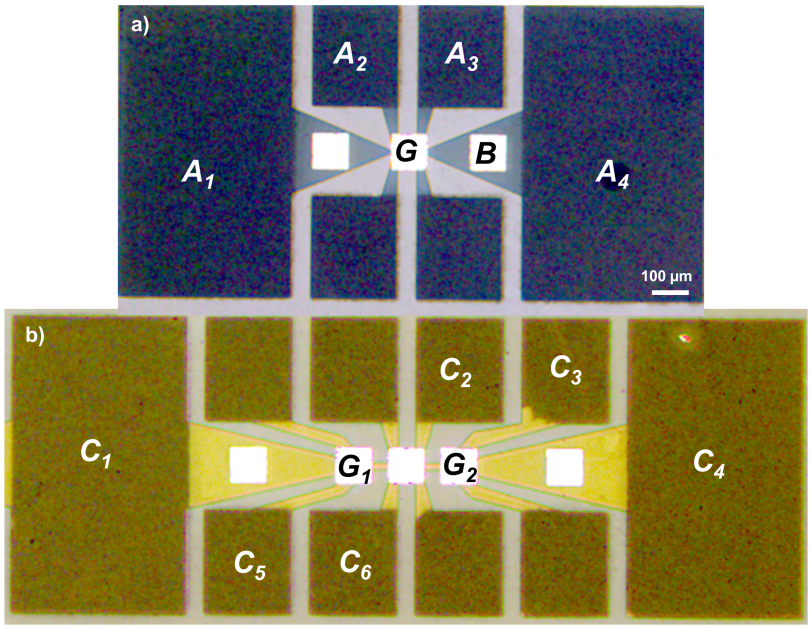



Figure 4.11: Optical images of a YBCO device fabricated with a) one track and one gate, and b) different tracks with several gates.

Fig.4.12a) shows the switching obtained for a device with one single gate. We observe clear and reproducible reversible changes in resistance when applied voltages of different polarities. Positive pulses drive the system to the LRS while negative pulses produce a switch to the HRS. Variations of 22 % are obtained by applying ±4 V. 30 % with 8 V and up to to 47 % with 12 V.

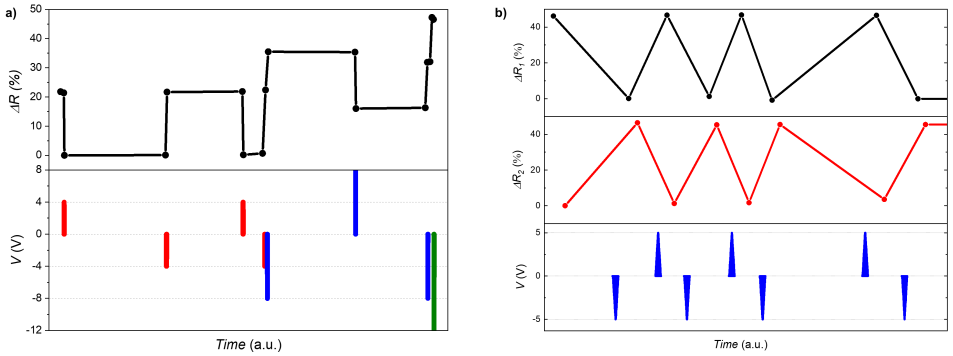



Figure 4.12: Percentage of variation of the resistance $R$ measured with a 4-point configuration after different gate voltage pulses a) one channel device, in b) two channel device.

Fig.4.13 shows a schematic representation of gate-induced oxygen motion in a device with one gate. When a positive pulse is applied, an accumulation of negatively charged oxygen ions (green) occurs under the gate $G$. To compensate, positively charged oxygen vacancies (red) are diffused to the sides (it is expected to have a higher accumulation of oxygen vacancies in the direction of the electrode used to switch the gate, $B$). Therefore, the value of the 4-point resistance $R$ measured below the gate (depicted with black dashed lines) decreases.

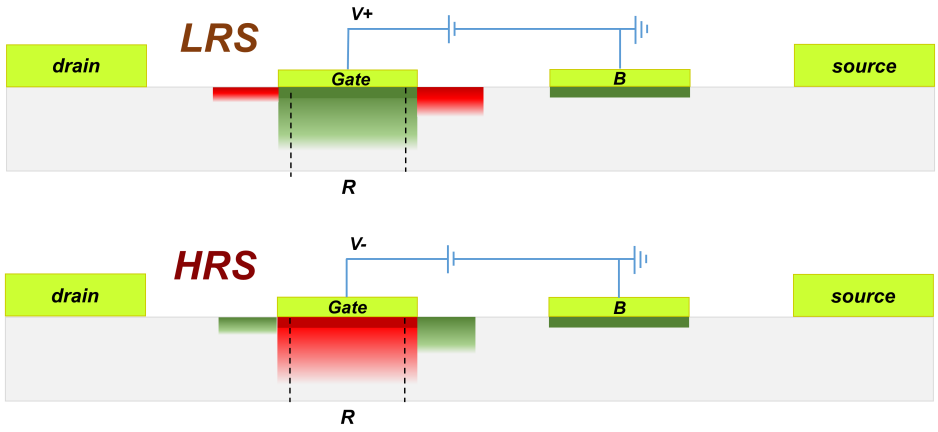



Figure 4.13: Sketch illustrating the redistribution of oxygen and oxygen vacancies in a YBCO device when applying positive (top) and negative (bottom) voltages to a gate using an external electrode $B$. Red and green represent regions in HRS and LRS respectively. Dashed lines show the region evaluated by 4-point contact configuration.

In a reversible way, when a negative pulse is applied to the gate, oxygen vacancies (red) are accumulated under the gate and oxygen ions diffuse at both sides of the gate. The possibility to completely switch the whole volume below the gate would depend on the applied voltage and the YBCO thickness.

Fig.4.12b) shows the switching performance obtained in a device with two gates (Fig.4.11b). In this example the resistance of two bridges are tracked by applying current from $C_1$ to $C_4$ and measuring the voltage between $C_5$ and $C_6$ or $C_2$ and $C_3$. A complementary switching behaviour is observed with one of the bridge going to the HRS and the other one to the LRS and vice-versa.

Reversible changes in the resistance in both bridges are obtained with variations of 45 % applying ±5 V indicating that the oxygen can be reversibly displaced through the channels. Fig.4.14 shows a schematic representation of oxygen motion in a two-gate device illustrating the oxygen and oxygen vacancy regions generated below each gate by applying voltage pulses of different polarities.

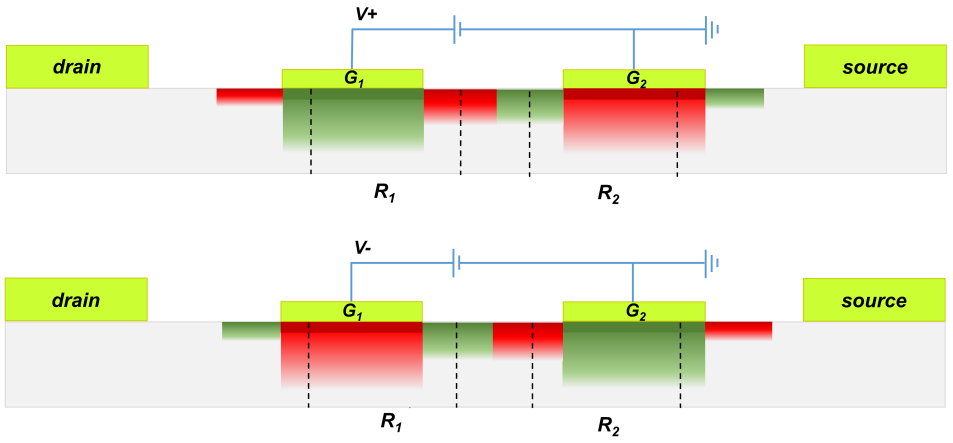



Figure 4.14: Sketch illustrating the redistribution of oxygen and oxygen vacancies in a YBCO device when applying positive (top) and negative (bottom) voltages between two closely gates ($G_1$ and $G_2$).Red and green represent regions in HRS and LRS respectively, which thickness is in relation with the percentage of change of the resistance.

## 4.5 Gate modulation of the SC performance

In order to elucidate the effect of field-induced oxygen doping in the superconducting properties, we have measured the critical temperature, and the magnetic field dependence of the critical current density, $J_c$, at different resistance states (doping levels), and correlate it with microstructural changes induced by the switching process. To do so, voltage pulses were applied at 300 K on patterned YBCO films of different thicknesses, using a large gate contact of $A = 100\ \mu\text{m} \times 100\ \mu\text{m}$ covering the whole track (Fig.4.4b,c). After each switch we measured the change in the volume resistance and carrier density of the track using transversal and lateral voltage contacts ($A_2$, $A_3$, $A_5$ and $A_6$ in Fig.4.4).

### 4.5.1 Impact of field-induced oxygen doping on $T_c$

Fig. 4.15 shows that a systematic decrease of $T_c$ and increase of Hall resistance, $R$, (decrease of the carrier density, $n_H$) is obtained when applying successive negative voltage pulses to the 50 nm sample inducing transitions to different HRS levels.

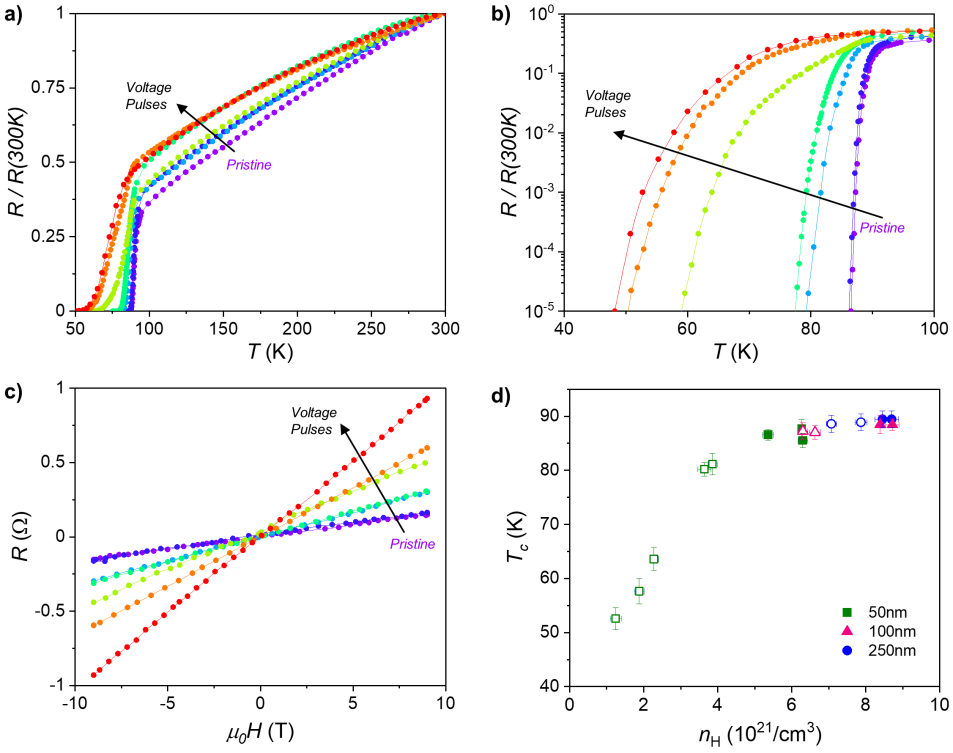



Figure 4.15: Critical temperature and carrier density at different oxygen doping levels. (a) Linear and (b) log-scale normalized resistance as a function of temperature, for a 50 nm sample at the pristine LRS and after several consecutive voltage switches at -1.8 V, -2 V, -2.5 V, -3 V, -4 V and -5 V. (c) Evolution of the Hall resistance vs magnetic field at 300 K with the applied voltage switch. (d) Superconducting critical temperature, $T_c$, as a function of the carrier density, $n_H$, obtained for YBCO tracks of different thickness at the LRS (closed symbols) and after applying several negative voltages switches at different HRS (open symbols). Green squared points correspond to samples shown in (a–c).

From the sharp and narrow superconducting transition obtained in the pristine state, we were able to deoxygenate the sample through voltage pulses, obtaining broader transition and therefore, a reduction of the critical temperature values. Fig.4.15d shows $T_c$ as a function

of $n_H$ for samples with different thickness in the pristine LRS state (closed symbols) and after being switched to different high resistance states (open symbols).

A continuous modulation of the carrier density to different underdoped states and associated $T_c$ reduction is observed for the thinnest sample ($t = 50$ nm). Many different resistance levels may be obtained by changing the applied gate voltage as it can be clearly observed in the different green open squares (50 nm). As expected, the variation obtained for thicker samples is much lower since in this case not all the track thickness under the gate has been switched to the high resistance state [125].

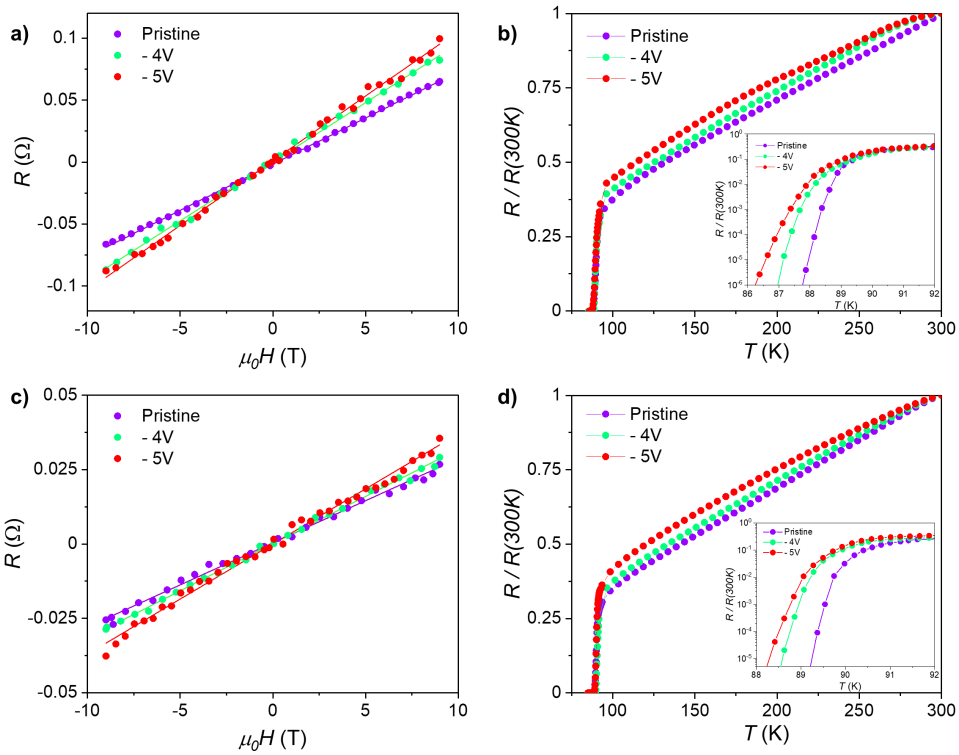



Figure 4.16: Evolution of a) Hall Resistance vs. applied magnetic field and b) longitudinal resistance as a function of temperature for a 100 nm YBCO sample at the pristine LRS and after several consecutive voltage switches. c) and d) Same as a) and b) but with a 250 nm sample. Insets in b) and d) are the same plot but in log-scale.

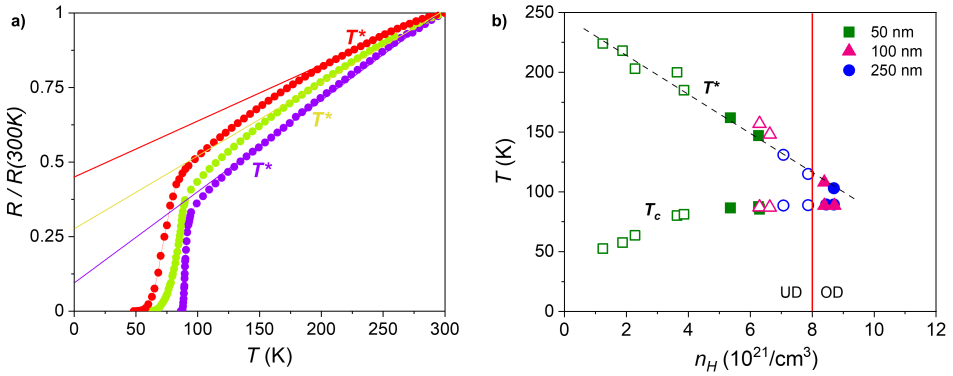



Figure 4.17: a) Linear normalized $R$ as a function of $T$ from different oxygen doping levels of the 50 nm sample. Added lines show the linear behavior where $T^*$ can be extracted. b) phase diagram for YBCO adding the values of $T_c$ and $T^*$ from different oxygen doping levels of 50 nm, 100 nm, and 250 nm samples.

The corresponding $T_c$ and Hall resistance, $R$, plots obtained for the 100 nm and 250 nm thick samples are shown at Fig.4.16, where we can closely see that the change obtained is lower than the observed in the thinner sample (Fig.4.15a-c).

Subsequently, we extract from the $R(T)$ measurements the pseudogap temperature, $T^*$. Fig.4.17 shows the normalized resistance variation with the temperature for three different oxygen doping levels of the 50 nm sample, including added fitted lines to obtain $T^*$. Fig.4.17b shows $T_c$ and $T^*$ obtained for the 50, 100 and 250 nm samples switched at different doping levels, to generate the phase diagram of switched samples that faithfully reproduce expected for cuprate films (Fig.1.16).

### 4.5.2 Impact of field-induced oxygen doping on $J_c$

The fine control of the oxygen content with the switching voltage allows us to perform a systematic study of the critical current density in the YBCO track, at different resistance states. Figs.4.18a,b show the magnetic field and angular dependence, respectively, of $J_c$ for a 100 nm sample at the pristine state and after being switched to three different HRS.

Starting from a pristine LRS we switch the sample to HRS-3 by applying -4 V. A very strong decrease of $J_c$ of more than one order

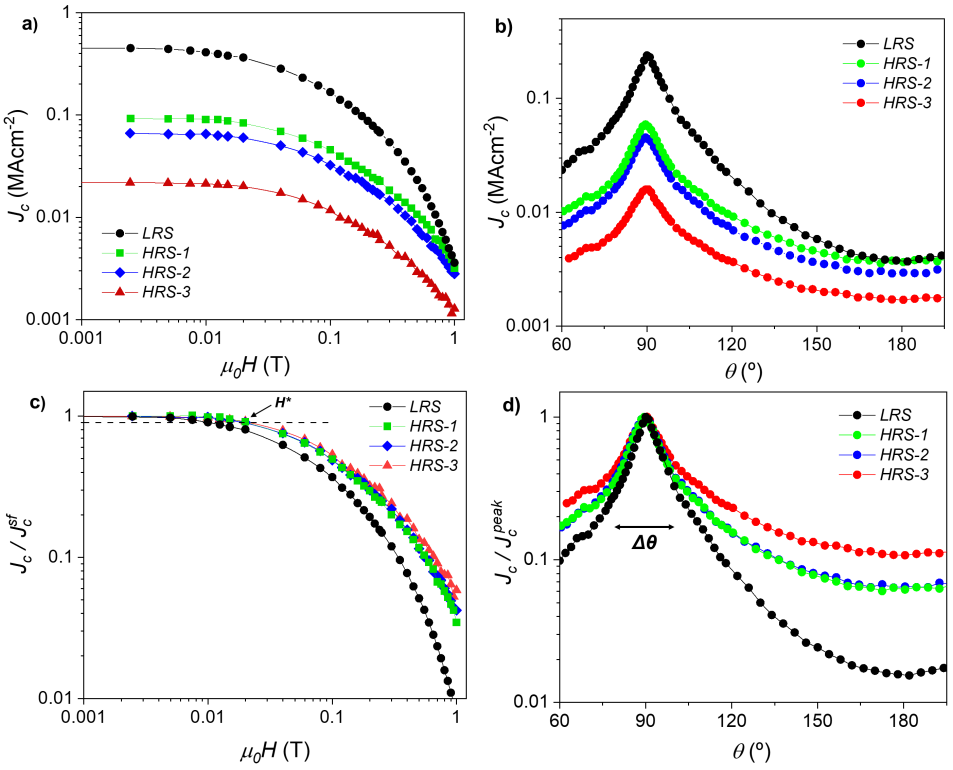



Figure 4.18: Field and angular dependence of the critical current density. a) $J_c(H)$ and b) $J_c(\theta)$ curves were measured at 1 T $H//c$, 85 K, for a 100 nm sample at three different oxygen doping states c) $J_c(H)$ curves shown in a) normalized at the value of self-field, $J_c^{sf}$. d) $J_c(\theta)$ curves shown in b) normalized at the maximum value of peak at $H//ab$ ($\theta = 90$ °).

of magnitude is observed. The track can be partially recovered to intermediated high resistance states by inverting the voltage polarity (HRS-2 @ 3 V and HRS-1 @4 V), although the system cannot be reversibly switched back to the initial LRS.

The changes in $J_c(H)$ and $J_c(\theta)$ at different doping levels can be better appreciated in the normalized plots shown in Figs.4.18c and 4.18d, respectively. Overall, we observe a smaller magnetic field decay of $J_c$ with an associated shift of $H^*$ (crossover field determined at 90 % of self-field $J_c$) to higher fields, and a broadening of the $H//ab$ peak by switching the sample to HRS. The same trend is observed at 77 K (Fig.4.19).

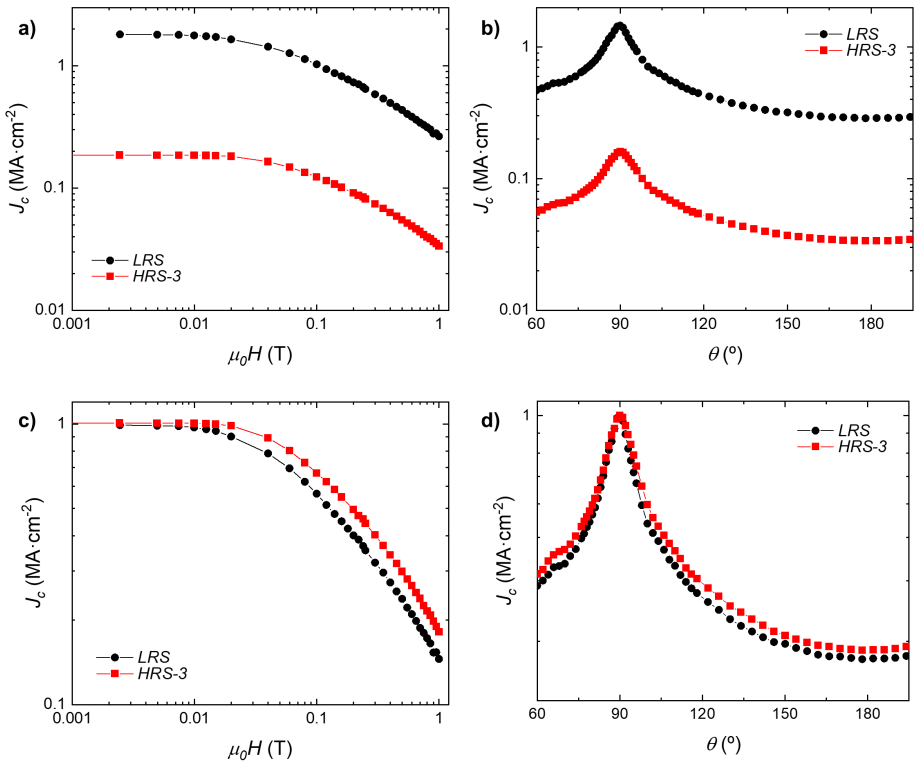



Figure 4.19: Field and angular dependence of the critical current density. a) $J_c(H)$ and b) $J_c(\theta)$ curves were measured at 1 T $H//c$, 77 K, for a 100 nm sample at two oxygen doping states c) $J_c(H)$ curves shown in a) normalized at the value of self-field, $J_c^{sf}$. d) $J_c(\theta)$ curves shown in b) normalized at the maximum value of peak at $H//ab$ ($\theta = 90$ °).

Fig.4.20 shows the normalized *ab*-peak measured at different doping levels at 77 K and 85 K. As discussed above, the width of the peak increases by switching the sample to HRS levels. Solid lines are fits with a Lorentzian peak function (eq.3.1).

The evolution of the $J_c^{sf}$, $H^*$ and $\Delta\theta$ with the reduction of the oxygen doping level at both 77 K and 85 K are depicted in Fig.4.21. Overall we observe a decrease of the critical current density values and an enhancement of the crossover field and trapping angle values, by switching the sample to progressively higher resistance states.

It should be noted that $J_c$ can be switched to intermediate reversible high resistance states, HRS$^{rev}$, if oxygen-depleted states are induced

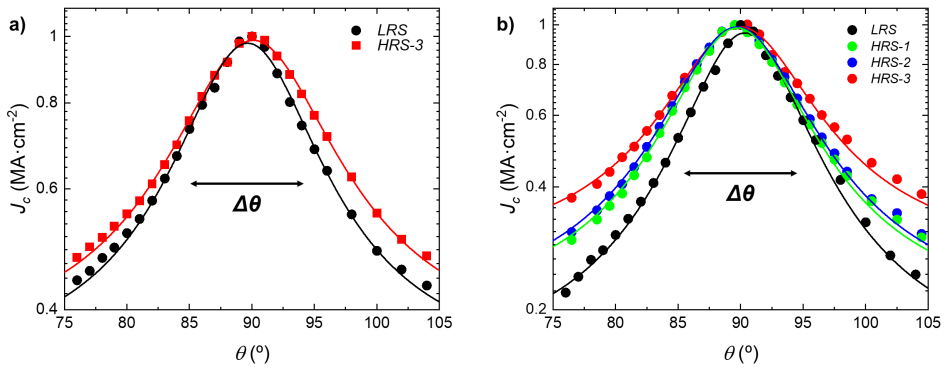



Figure 4.20: Angular dependence of the normalized critical current density at 90 ° and 1 T $H//c$, for a 100 nm sample at different oxygen doping levels. Solid lines are Lorentzian fits with $\Delta\theta$ full with half maximum. a) at 77 K and b) at 85 K.

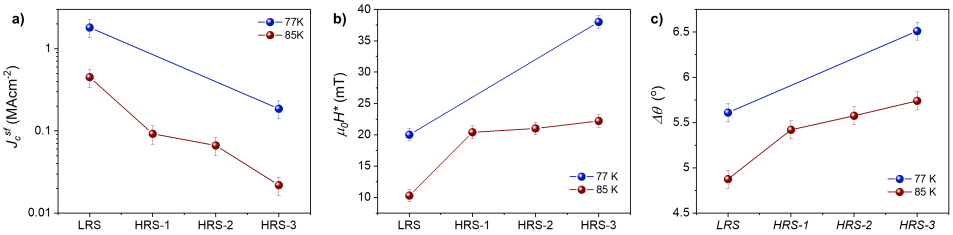



Figure 4.21: Dependence of the superconducting performance with oxygen doping level. Evolution of (a) self-field critical current density, $J_c^{sf}$, (b) crossover magnetic field, $H^*$, and (c) width of the $H//ab$ peak, $\Delta\theta$, by reducing the oxygen doping level through gate voltage pulses.

by applying lower voltage pulses. For instance, after applying -2 V, $J_c$ can be drecreased from 1.8 MA/cm$^2$ to 1.5 MA/cm$^2$ (black to green dots in Fig.4.22) and after +2 V, initial $J_c$ values can be recovered (from green to red). In order to obtain reversible changes however, the modulation of $J_c$ may be kept below 20 % , and the modulation of $\mu_0 H$ around 20 %.

In order to elucidate the defects that produce a change in the $J_c$ performance at the HRS, the microstructure of the YBCO layer was studied using scanning transmission electron microscopy (STEM) in combination with electron energy-loss spectroscopy (EELS). Figs. 4.23a,d show a Z-contrast image of a YBCO track in the LRS and HRS, respectively. Both images show an epitaxial and coherent YBCO layer as well as dark stripes running parallel to the (001) YBCO plane.

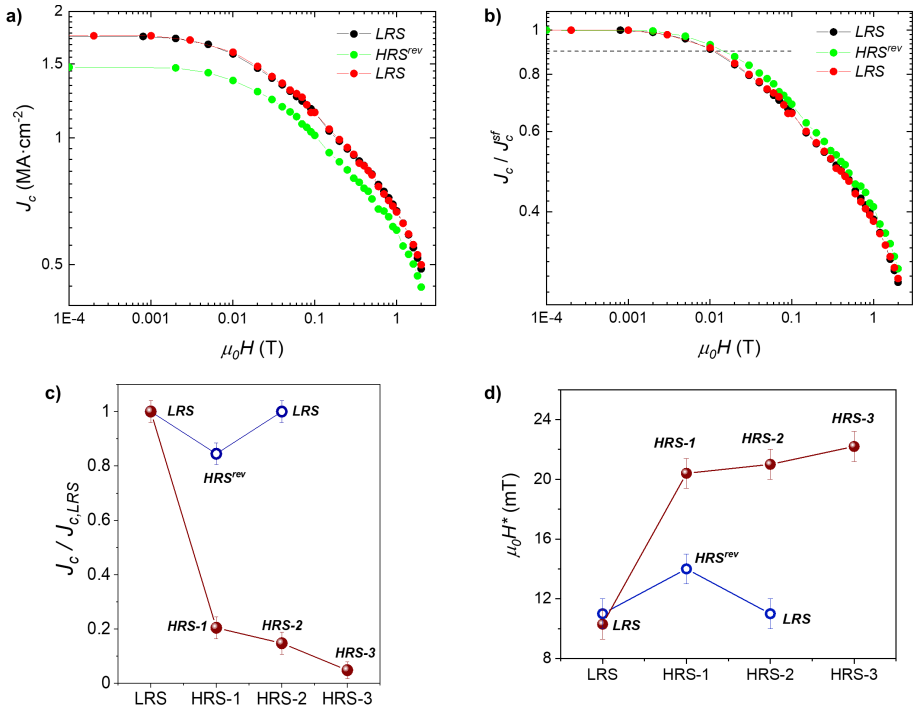



Figure 4.22: a) Critical current density dependence with the magnetic field in log-log scale, b) Same as a) but normalized values at self-field, c) Evolution of $J_c$ after being switched to different irreversible HRS using high voltage pulses (red symbols), and reversible HRS$^{rev}$ at low voltage pulses (blue symbols), d) shows the same as c) but with the evolution of $\mu_0 H$.

These planar defects are the well known as $YBa_2Cu_4O_7$ (Y124) structural defects, which consist of an intergrowth of an extra Cu–O chain layer inserted into the YBCO [207]. It should be noted, that the sample switched to the HRS presents a higher density of Y124 intergrowths, especially at the uppermost region of the layer. Indeed, close to the surface of the film there is an around 40 nm thick layer of pure Y124 phase, which is absent in the YBCO layer when it is in the LRS. Insets in Figs.4.23a,d show atomic-resolution images of the highlighted regions, in which the arrows point at the double Cu–O chain.

We also studied the electronic structure of the YBCO layer at high and low resistance states by means of EELS. Figs.4.23b,c,e,f show the Cu L and the O K edges at the LRS and HRS, respectively, acquired in different regions of the YBCO layer. Notice the different fine structure

or shape of the center peak (535 eV) of the O-K edge, or the different L3/L2 intensity ratio of the Cu L-edge when the YBCO layer is found at different resistance states. These differences are consistent with the presence of a higher concentration of oxygen vacancies and reduced Cu atoms in the HRS, which is also consistent with a larger number of double Cu–O chains, and therefore more reduced Cu atoms [197, 208].

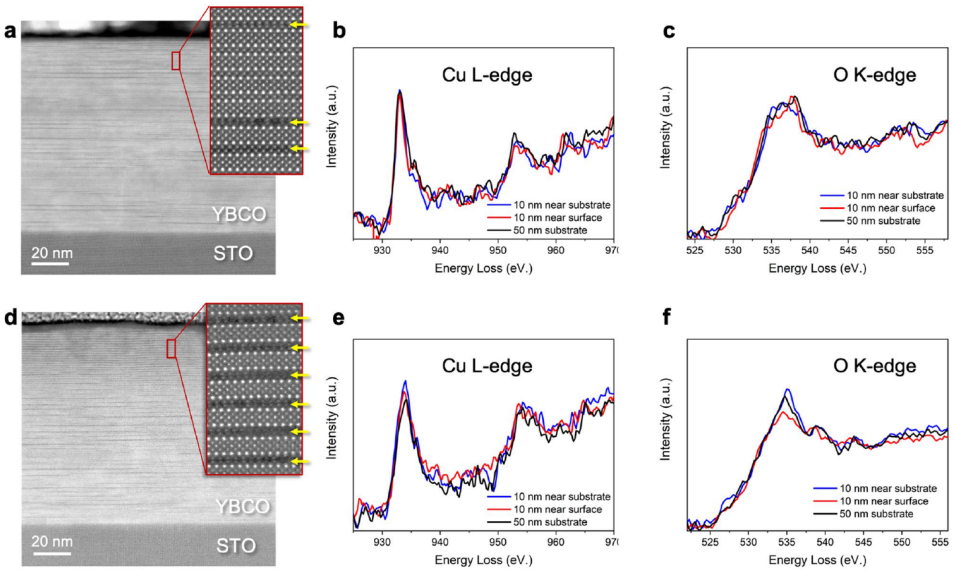



Figure 4.23: Microstructural defects. (a) Z-contrast image of a 100 nm YBCO track at the LRS, (b) Cu L-edge, and (c) O K-edge acquired at different regions of the pristine track. (d) Z-contrast image of a YBCO track switched to the HRS after applying a voltage pulse of -4 V. (e) Cu L-edge and (f) O K-edge at the HRS acquired at different regions of the track. Insets in (a,d) show a high-resolution Z-contrast image of the regions marked in red.

TEM results indicate that the field-induced transition to the HRS occurs due to the formation of Y124 intergrowths with a high density of oxygen vacancies, which can be clearly correlated with the obtained superconducting performance. A shift of $H^*$ to high fields together with a broadening of the $H//ab$ peak observed when the sample is switched to the HRS (Fig.4.21) is typically obtained in YBCO nanocomposites with a large amount of Y124 intergrowths induced by the presence of randomly oriented nanoparticles [61, 131] (see Chapter 3).

The formation of these large number of defects might be responsible for the non-reversible switching performance obtained when the sys-

tem is driven to a very high oxygen-depleted state. According to our previous works, reversible effects are obtained when oxygen diffusion can be reversibly controlled homogeneously tuning the sample doping [115, 125]. Irreversible effects, which may be associated to the presence of defects or inhomogeneous distributions of oxygen vacancies appear when thermal effects start to be important [123, 124]. Indeed, thermal defect nucleation at large applied voltages, producing irreversible resistivity changes, have also been obtained in perovskites [209].

## 4.6 Conclusions

We have studied the effect of field-induced metal insulating transition in YBCO devices on both the normal resistance state and superconducting performance. Our results demonstrate that reversible gate resistive switching effects, with very large resistive ratios up to $10^5$, can be obtained by applying moderate voltage pulses of 2–4 V using micrometric gate contacts.

Multiple gates can be used to change the resistance (local oxygen doping) between a source-drain channel in a reversible way. The movement and redistribution of oxygen vacancies within the channel, and thus its resistance, may be controlled by the device geometry, gate position, and bias voltage. A large design flexibility can be obtained by changing the switching performance of different gates, thus offering the possibility to locally adjust the conductance response in different regions of a YBCO bridge.

Gate voltage pulses have been used to tune the oxygen content of YBCO tracks and strongly manipulate the associated superconducting properties, including critical current temperature, carrier density and critical current density. A temperature-doping phase diagram with the critical temperature ($T_c$) and pseudogap temperature ($T^*$) of samples switched to different under-doped levels have been generated, reproducing the one expected for cuprate films.

The fine control of the oxygen content have been used to perform a systematic study of the superconducting properties of samples at different doping levels. Reversible changes in the superconducting performance may be obtained by inducing changes from a pristine low resis-

tance state to high resistance state with moderate oxygen-depleted regions. TEM measurements in agreement with $J_c(H)$, $J_c(\theta)$ dependencies indicate that the volume switch from a pristine low resistance state to different irreversible high oxygen-depleted high resistance states occurs through formation of Y124 intergrowths with a high density of oxygen vacancies. These results provide insight on understanding the role of field-induced defects in field-induced oxygen doping of cuprate superconductors.

# Chapter 5

# Thermally-induced oxygen doping in YBCO films

High-temperature cuprate superconductors offer unique opportunities to tune their physical properties through oxygen doping modulation. Unprecedented versatility in the design of novel device functionalities may be achieved by exploiting the metal-insulating (MIT) transition of these materials at micro-, nano-scale. In the previous chapter we discussed the control of the oxygen content in YBCO films by means of electric-field induced oxygen diffusion. This chapter focuses on a novel approach for the modulation of oxygen doping in YBCO films at local scale based on thermal induced effects through Direct Laser Writing (DLW).

Direct laser writing technology emerges as a versatile, mask-free method for shaping, refining, and structuring perovskites [210]. Depending on the irradiation conditions different effects can be induced, such as laser annealing, laser ablation, or laser-induced defects. Moreover, photothermal and photochemical effects, may be used to produce direct conversion of precursors into perovskites. This leads to the generation of diverse forms of laser-induced perovskites, including quantum dots, nanowires, nanocrystals, and films. Of particular note, the exploration of laser-induced perovskites within glass substrates gains momentum, driven by their notable attributes of high stability and adaptability for 3D printing.

In this work we patterned YBCO films of different thicknesses by using DLW. Direct observation of thermally-induced oxygen doping has been explored by optical imaging [123]. Additionally, the local surface conductivity was examined by using conductive atomic force microscopy (CAFM). A systematic investigation was carried out to analyze the impact of various writing parameters, such as laser power, writing duration, focus and pixel size. The effect of thermal-induced oxygen doping on the superconducting performance of the films was investigated by using YBCO devices patterned with transverse and Hall voltage contacts.

## 5.1 Device fabrication

YBCO thin films with thicknesses 10, 15, 20, and 30 nm were grown via pulsed laser deposition on a $LaAlO_3$ substrates. We used the same grown conditions and parameters described in Chapter 4. YBCO films were patterned with eight identical devices allowing Transverse and Hall measurements. Half of the film was kept un-patterned to allow the optimization of sample irradiation parameters. The device's geometry is depicted in Fig.5.1.

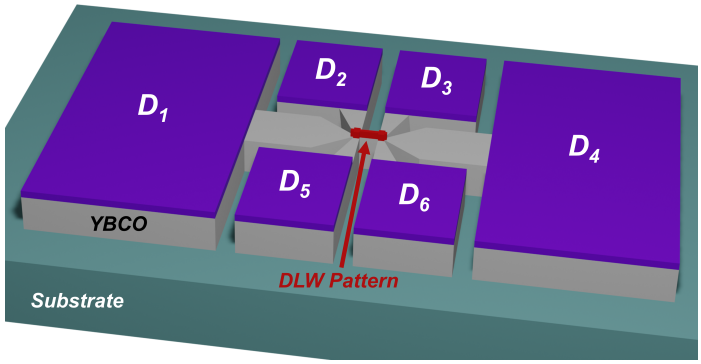



Figure 5.1: Schematic representation of the measurement configuration. Red area shows the zone irradiated with the laser.

Initially, the YBCO structure was fabricated through optical lithography, followed by the deposition of 75-nm gold contacts (in purple). The devices were designed with four different voltage, contacts enabling measurements in different configurations, and a central track of 10 $\mu$m width and 20 $\mu$m length. A 4-point configuration was used for

both transport ($T_c$ and $J_c$) and Hall ($n_H$) measurements. In the first case by applying current between $D_1$ and $D_4$, and measuring voltage between $D_2$ and $D_3$ or between $D_5$ and $D_6$. In the second case applying current between $D_1$ and $D_4$, and measuring voltage between $D_2$ and $D_5$ or between $D_3$ and $D_6$. Sample irradiation was performed just above the YBCO bridges (depicted in red).

## 5.2 Direct Laser writing in YBCO films

Sample irradiation was performed through a collaboration with Dr. Edoardo Albisetti at Polifab, Politecnico di Milano, where I did a 2-month doctoral stay in the Engineering Physics in Nanostructured materials and Devices group (PhyND). This section describes the optimization of direct laser patterning parameters.

To do so, different laser scans were performed writing pixel by pixel, starting from the bottom of the pattern and moving horizontally from left to right. Upon completing each line, the laser was switched off and moved to the left part of the following line to continue the writing procedure. The primary parameters that can be adjusted for laser patterning include focus position (FOC), laser power (LP) and laser time (LT). A detailed examination of the effects produced by different laser parameters was performed for samples of different thicknesses.

### 5.2.1 Adjustment of the laser focus

The optimal focus position is typically determined automatically by the software during calibration tests conducted prior to each writing session. However, the accuracy of the software calibration is not always the optimum one. Therefore, to ascertain the optimal value, a systematic study was conducted as a function of the focus position to directly observe the effect of the laser focus on the patterning. Fig.5.2 show an optical image obtained for a 10 nm YBCO film patterned with a series of squares drawn with different focus and laser times. A filter on the green component of the image is applied to enhance the visibility of the patterned areas. The effect of the laser on the film is clearly visible with a bright intensity. This is consistent with a laser-induced sample deoxygenation since as observed in [123, 211] higher reflectivity indicate the presence of oxygen vacancies.

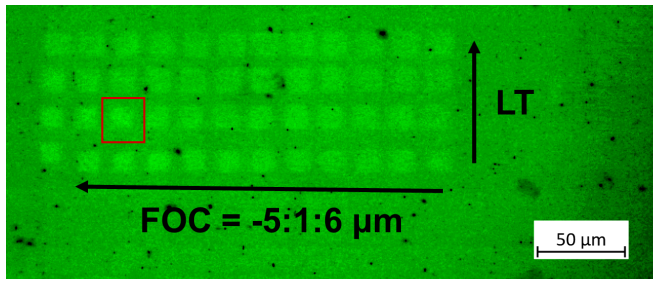



Figure 5.2: Optical image of YBCO with a thickness of 10 nm, displaying a grid of laser-patterned squares, each measuring 10 × 10 $\mu$m$^2$ with LP = 300 mW,

To obtain the calibration image shown in Fig.5.2 the focus position is adjusted between -5 and 6 $\mu$m in steps of 1 $\mu$m at different laser times (50, 100, 200, and 400 $\mu$s). Variations in pattern brightness at different focus positions are clearly visible. From this image we use the brightest region, FOC $\approx$ 4 $\mu$m (marked in red) for this particular test, to start with the sample writing. The focus was aligned for all samples before starting the irradiation.

### 5.2.2 Laser power and writing time

The most critical factors influencing the patterning process are the laser power (LP) and the laser writing time, as they directly control the amount of energy delivered to the system. In the case of the writing time, one has to consider two parameters, the laser pulse, which refers to the duration of the pulse for each pixel, and the pixel time, which defines the time interval between writing adjacent pixels. In all the experiments the pixel time was fixed at 30 $\mu$s and we changed the duration of the laser pulse, denoted as laser time (LT).

To examine the effect of patterning at various power and time levels, we conducted a series of line-shaped patterns of 30 $\mu$m x 30 $\mu$m on a 30-nm thick YBCO sample. Fig.5.3) shows an optical image of the irradiated sample were patterned areas are clearly visible. The laser power was varied from LP = 75 mW to LP = 200 mW with increments of 25 mW and we used 3 different laser times LT = 25 $\mu$s, 100 $\mu$s and 6400 $\mu$s. As expected the width of the patterned lines increases with LP an LT. In the sample patterned with LP = 200 mW and 6400 $\mu$s the lines almost overlap.

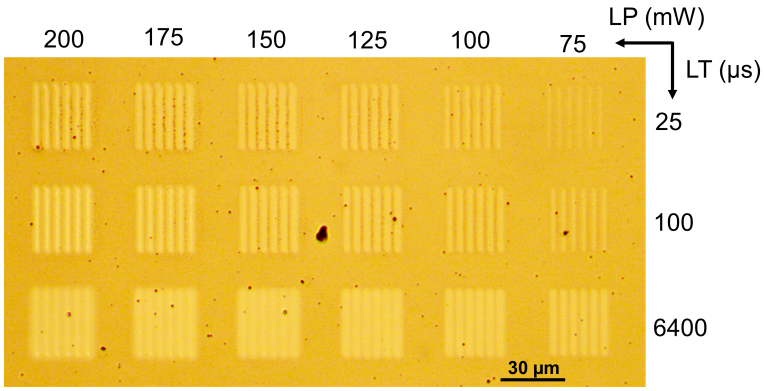



Figure 5.3: Optical image depicting the laser irradiation of a 30-nm thick YBCO sample with lines covering an area of 30 $\mu$m × 30 $\mu$m. LP was varied from 75 mW to 200 mW with LT 25 $\mu$s, 100 $\mu$s and 6400 $\mu$s.

Conductive atomic force microscopy (CAFM) measurements were performed in the patterned sample (shown in Fig.5.3) in order to evaluate the surface conductivity. Results are shown in Fig.5.4. The obtained CAFM image can be clearly correlated with the reflectivity changes observe in the optical image. However, contrary to what one would expect, the deoxygenated regions appear to be more conductive.

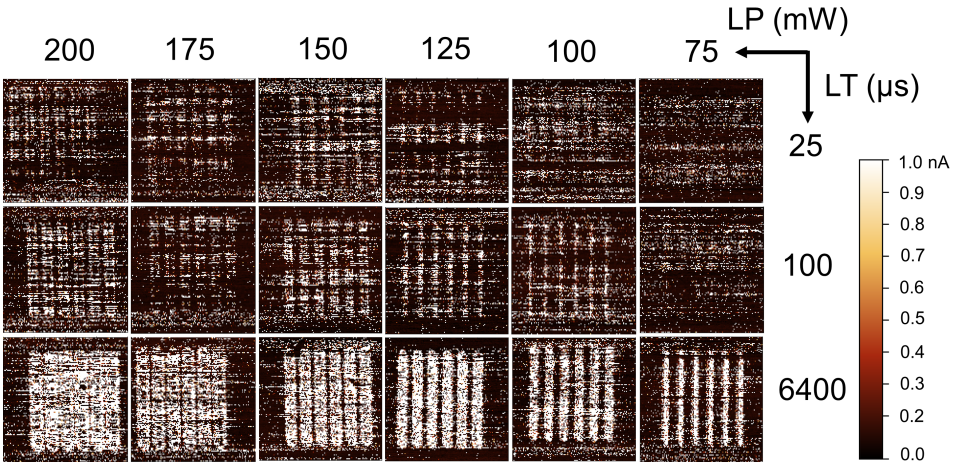



Figure 5.4: CAFM image obtained at 1V for a 30-nm thick YBCO sample patterned with lines covering an area of 30 $\mu$m × 30 $\mu$m. LP was varied from 75 mW to 200 mW with LT 25 $\mu$s, 100 $\mu$s and 6400 $\mu$s.

One possible explanation of these effect could be that laser-induced oxygen vacancies generated in the bulk induce a migration of oxygen at

the surface thus producing an enhancement of the surface conductivity measured by CAFM. Another possibility could be that, CFAM could produce field-induced oxygen motion (effect discussed in the previous section) that would be accumulated at the surface.

### 5.2.3 Thickness dependence of laser irradiation

Laser irradiation tests were conducted on YBCO samples of three different thickness, 10 nm, 20 nm, and 30 nm (Fig.5.5). Although the effect of laser writing is visible in all the samples, the brightness contrast increases with the sample thickness.

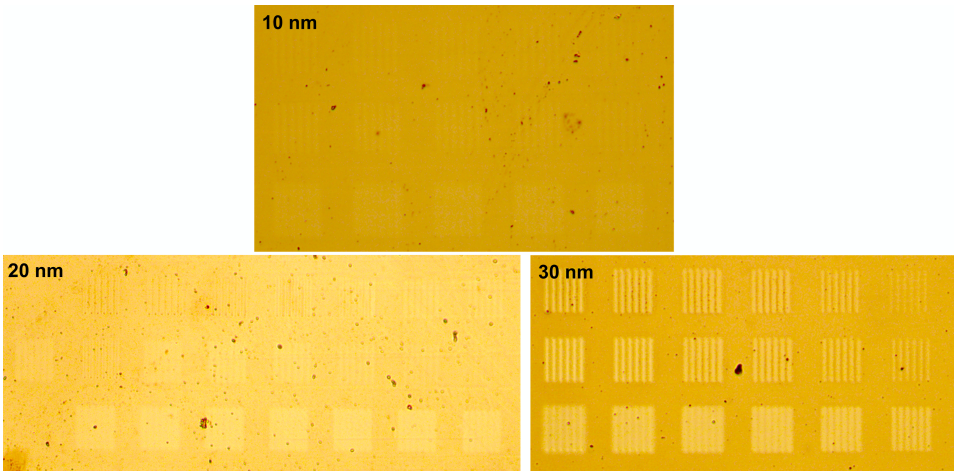



Figure 5.5: Optical images of patterns obtained for YBCO devices of different thicknesses, 10 nm, 20 nm and 30 nm, patterned under the same conditions as the one shown in Fig.5.3)

On the 10-nm thick sample, the patterns very difficult to be identified, often requiring a green filter to enhance the brightness (as seen in Fig.5.2). On the contrary on the 30-nm thick sample the patterns are clearly visible even with white light. Thickness dependence on the sample reflectivity could be associated to the fact that the starting oxygen doping is different in each sample. As shown in Fig.4.3 the oxygen doping decreases by decreasing the YBCO film thickness. So, the effect of laser irradiation seems to be lower in the samples with lower starting oxygen content. Moreover, it could also be possible that laser absorption could be enhanced by the thickness.

## 5.3 Impact of laser patterning on the SC performance

In order to evaluate the effect of direct laser writing on the YBCO superconducting performance we irradiated different YBCO patterned tracks. After laser irradiation under different conditions we measured the critical temperature, $T_c$, charge carrier density, $n_H$, and critical current density, $J_c$.

We irradiated six out of the eight devices present on the 10 nm, 15 nm and 20 nm YBCO films. Figs.5.6, 5.7 and 5.8 shows a description of the patterns performed and laser parameters used. In all the samples we reserved two un-patterned devices for comparison purposes. The one labeled as pristine is a device that we measured before sending the sample to irradiation and the one labeled as unpatterned is a device that was introduced inside the laser chamber but that was not exposed.

| | | | | | |
|---|---|---|---|---|---|
| **D10-1** | Pristine | | **D10-5** | LP = 225 mW, 35 x 15 μm$^2$ | |
| **D10-2** | Unpatterned | | **D10-6** | LP = 250 mW, 35 x 15 μm$^2$ | |
| **D10-3** | LP = 300 mW, 3 x 20 μm$^2$ lines | | **D10-7** | LP = 275 mW, 35 x 15 μm$^2$ | |
| **D10-4** | LP = 300 mW, 18 x 15 μm$^2$ | | **D10-8** | LP = 300 mW, 35 x 15 μm$^2$ | |

Figure 5.6: Table showing the different laser patterns irradiated on a 10 nm YBCO film using LT = 100 $\mu$s and FOC = +5 $\mu$m.

The purple regions depicted in the figures schematically show the patterns used. In some of the devices we completely irradiated the tracks with different laser power (D10-5 - D10-8, D15-5 - D15-8, D20-5 - D20-8). We also patterned tracks with lines using a fixed power (D10-3 and D15-3) and varying the power in each line (D20-30). D10-4 and D15-4 where irradiated just on half of the track.

| | | | | | |
|---|---|---|---|---|---|
| **D15-1** | Pristine | | **D15-5** | LP = 25 mW, 35 x 15 μm$^2$ | |
| **D15-2** | Unpatterned | | **D15-6** | LP = 50 mW, 35 x 15 μm$^2$ | |
| **D15-3** | LP = 150 mW, 3 x 20 μm$^2$ 6 lines | | **D15-7** | LP = 100 mW, 35 x 15 μm$^2$ | |
| **D15-4** | LP = 175 mW, 18 x 15 μm | | **D15-8** | LP = 150 mW, 35 x 15 μm$^2$ | |

Figure 5.7: Table showing the different laser patterns irradiated on a 15 nm YBCO film using LT = 100 $\mu$s and FOC = +5 $\mu$m.

| | | | | | |
|---|---|---|---|---|---|
| **D20-1** | Pristine | | **D20-5** | LP = 100 mW, 35 x 15 μm$^2$ | |
| **D20-2** | Unpatterned | | **D20-6** | LP = 125 mW, 35 x 15 μm$^2$ | |
| **D20-3** | LP = 125 mW, 3 x 20 μm$^2$ lines | | **D20-7** | LP = 150 mW, 35 x 15 μm$^2$ | |
| **D20-4** | Lines 22 x 1 μm 100:25:175 mW Separation 3 μm | | **D20-8** | LP = 175 mW, 35 x 15 μm$^2$ | |

Figure 5.8: Table showing the different laser patterns irradiated on a 30 nm YBCO film using LT = 100 $\mu$s and FOC = +5 $\mu$m.

The first YBCO film that we patterned was the one of 10-nm, using a laser power ranging from 225 mW to 300 mW. After irradiation, we performed transport measurements and observed that the sample was completely insulating so we decided to use lower power on the other two films. We used powers ranging from 25 mW to 150 mW and 100 mW to 175 mW for the 15 nm and 20 nm YBCO films, respectively.

Before starting with the patterning of the devices, a preliminary test was conducted in order to determine the focus position which was

fixed at +5 $\mu$m for the film of 10 nm, +5 $\mu$m for the one of 15 nm and +4 $\mu$m the one of 20 nm.

Initially, the patterned devices were examined under an optical microscope to preliminary assess the effects of laser writing. Figures 5.9 and 5.10 display optical images of several of the patterned devices. Images were acquired by using a green filter to enhance pattern visibility. Irradiated patterns, according to the used design, are visible in all of the devices.

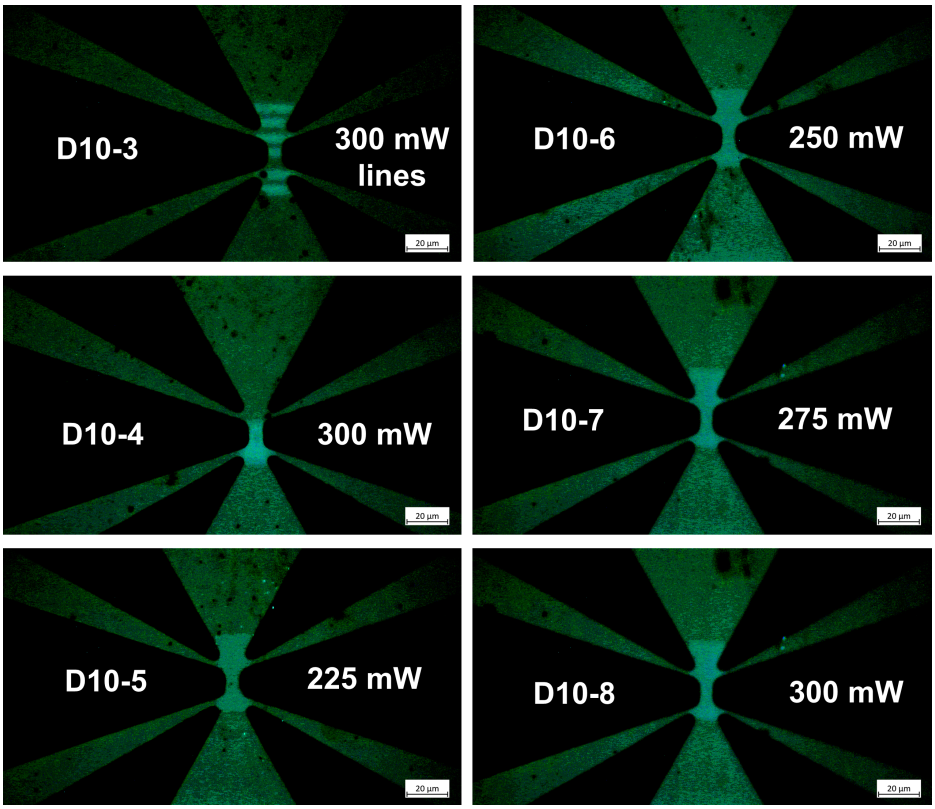



Figure 5.9: Optical images obtained at 50x magnification for several laser irradiated devices in a 10 nm YBCO film.

Low-temperature transport measurements were performed on the different laser irradiated tracks in order to study the effects on the critical temperature ($T_c$), carrier density ($n_H$), and critical current density ($J_c$).

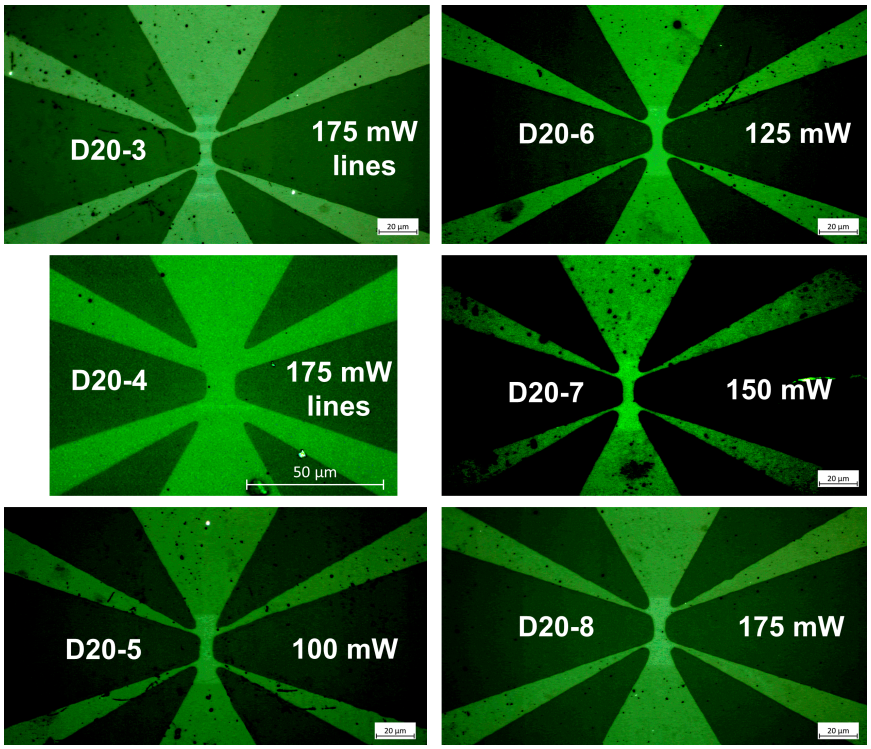



Figure 5.10: Optical images obtained at 50x magnification for several laser irradiated devices in a 20 nm YBCO film.

### 5.3.1 Impact of laser-induced oxygen doping on $T_c$

As commented above, the 10 nm sample could not be studied since all the devices were insulating after irradiation. Fig.5.11 shows the temperature dependence of the resistance measured for the devices patterned on the 20 nm (Fig.5.11(a, b)) and 15 nm (Fig.5.11(c, d)) YBCO films. It should be noted that in both samples, the $T_c$ of unpatterned devices is reduced as compared to the pristine ones indicating that the the sample is slightly deoxygenated when it is introduced on the laser chamber.

In the case of the 20 nm film, we observe that the critical temperature is strongly reduced from 75 K to 40 K using a laser irradiation of 100 mW and to 35 K using powers of 150 mW and 175 mW. The reduction obtained using 125 mW is highly higher to the expected beeing 30K. From these results we conclude that 100 mW is already a large power which induces a strong $T_c$ reductions. So, we used lower power

ranges for irradiating the 15 nm YBCO film. By doing so, a very clear trend of $T_c$ with the power can be obtained where $T_c$ is progressively reduced from 65 K to 30 K using power irradiation's of 25 mW to 150 mW.

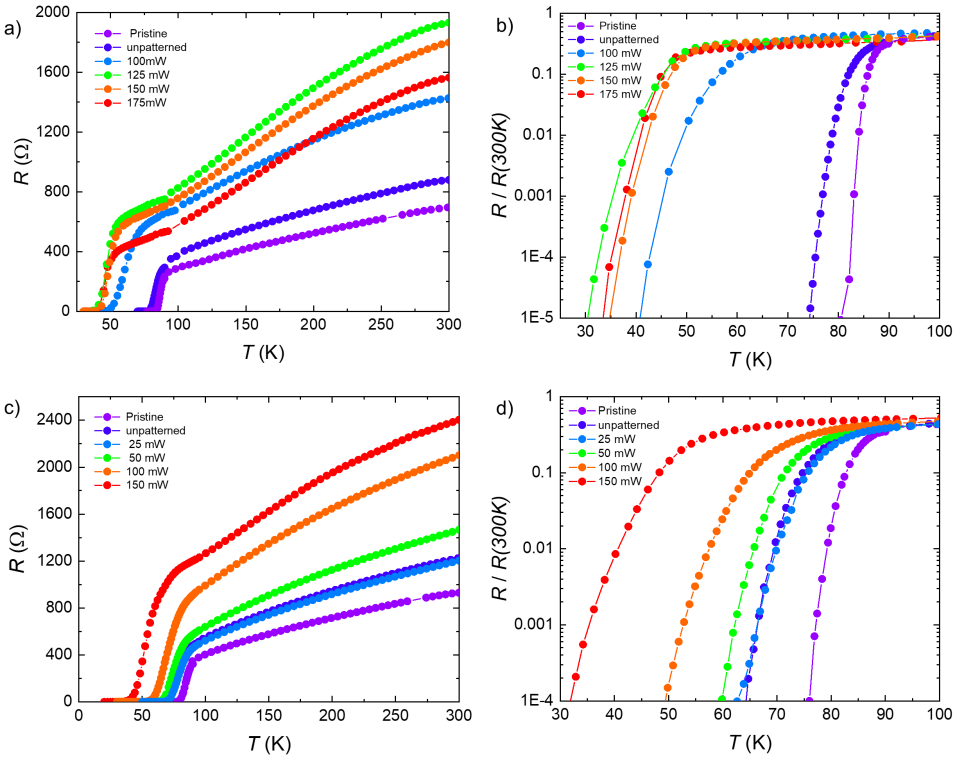



Figure 5.11: Critical temperature in linear and log scale obtained for several devices patterned on a 20 nm YBCO film (a,b) and 15 nm YBCO film (c,d).

Hall measurements were conducted at 300 K on the devices from the 15-nm and 20-nm thick samples in order to obtain the carrier density, $n_H$. Fig.5.12a show $T_c$ plotted as a function of the extracted $n_H$ values. A clear correlation of $T_c$ with the doping level is obtain reproducing the expected superconducting dome of $T_c$ vs doping. Fig.5.12b shows the same data plotted together with the values of the the pseudogap temperature, $T^*$, determined from the resistance vs. temperature curves as described in Chapter 4. Both the dependence of $T_c$ and $T^*$ with the carrier density follow the trend expected for cuprate films (Fig.1.16). It should be noted that in this case pristine samples are already in the under doped state since we used very thin samples.

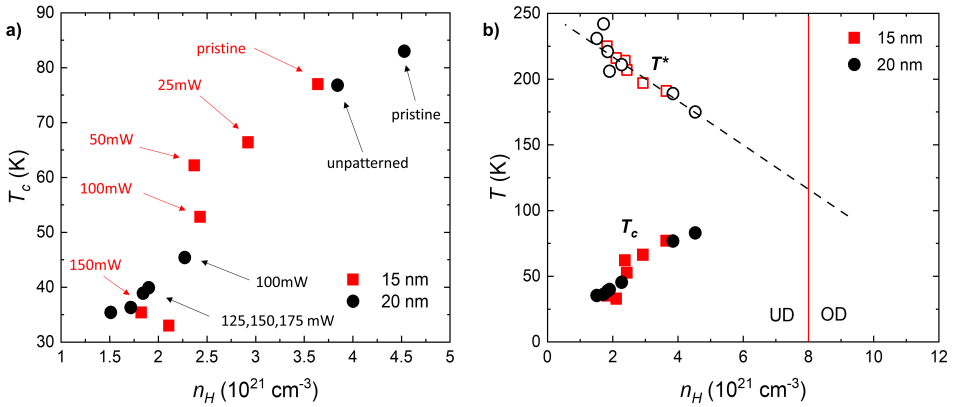



Figure 5.12: a) Critical temperature as a function of the charge carrier density for 15 nm and 20 nm devices irradiated at different laser powers. b) Phase diagram of $T_c$ and $T^*$ as a function of $n_H$ obtained for different irradiated devices.

### 5.3.2 Impact of laser-induced oxygen doping on $J_c$

In this section we will analyze the effect of laser writing on the critical current density of the 15 nm YBCO devices patterned at different conditions.

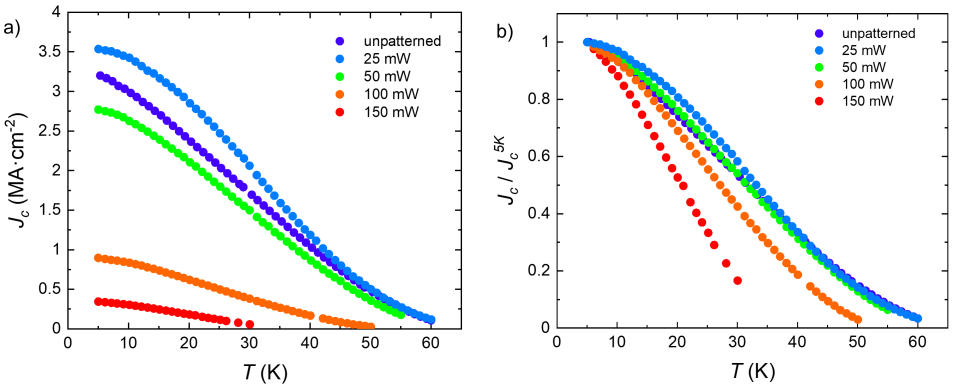



Figure 5.13: a) Critical current density dependence on the temperature for different patterned devices. b) curves shown in a) normalized to the value of $J_c$ at 5K.

Fig.5.13 shows the temperature dependence of $J_c$ obtained for tracks irradiated at different power, compared with an unpattterned one. A clar dependence is observe with a reduction of self-field $J_c$ and a fast decrease $J_c(T)$ as the laser power is increased. Very strong effects are obtained for the devices irradiated at higher powers (100 mW, 150 mW) in agreement with a large sample deoxygenation (Fig.5.11d).

Fig.5.14 shows the magnetic field dependence of $J_c$, normalized at self-field, obtained for tracks irradiated at 50 mW and 100 mW, and an unpatterned track. Fig.5.14(a) and (b) show the values obtained at 30 K and 50 K, respectively. Contrary to what we observed with the samples with field-induced oxygen motion (see Figs.4.18c), no clear changes in $\mu_0 H^*$, are obtained in this case. These results would indicate that laser-induced oxygen doping does not generate the same kind of defects than field-induced oxygen doping (stacking faults).

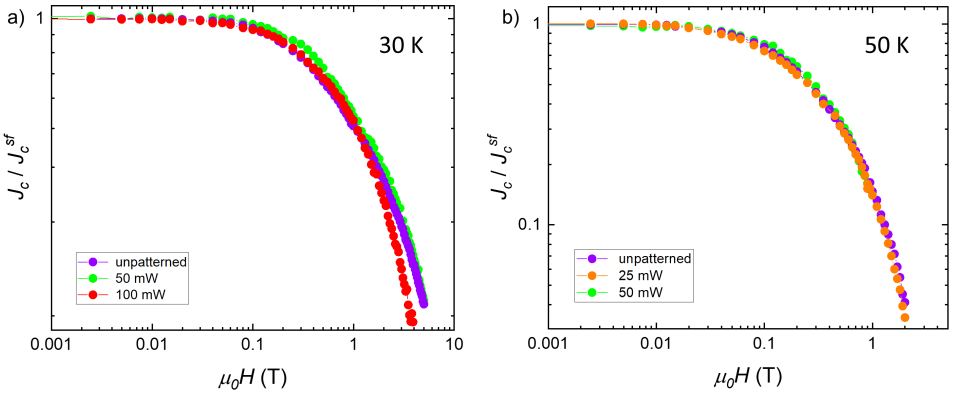



Figure 5.14: Critical current density, normalized at self-field, as a function of the applied field for different patterned devices at a) 30 K, and b) 50 K.

Finally, we study the dependence of the critical current density on the orientation of the magnetic field. Fig.5.15 show several $J_c(\theta)$ curves measured at various temperatures for devices irradiated at different powers. In all of the curves we observe a peak of $J_c(\theta)$ at 90 ° associated to a maximum critical current obtained for $H//ab$. However, besides the expected $ab$-peak a very surprising feature, a $J_c(\theta)$ plateau, is observed below 90 °. This plateau, completely unexpected, must be associated to the presence of some kind of laser-induced pinning centres efficient at this particular angle orientations.

In order to better elucidate the effect of this pinning centres we have plotted in Fig.5.16 the mid-point angle of the plateau, $\theta_{plateau}$, obtained for samples irradiated at different powers. It should be noticed that $\theta_{plateau}$ is shifted to low values with decreasing the magnetic field and the temperature. Moreover, sample irradiated at large power (100 mW) show lower $\theta_{plateau}$ values. The length of the plateau, indicated with error bars, is very similar for all the points ($\sim$ 5-6 °).

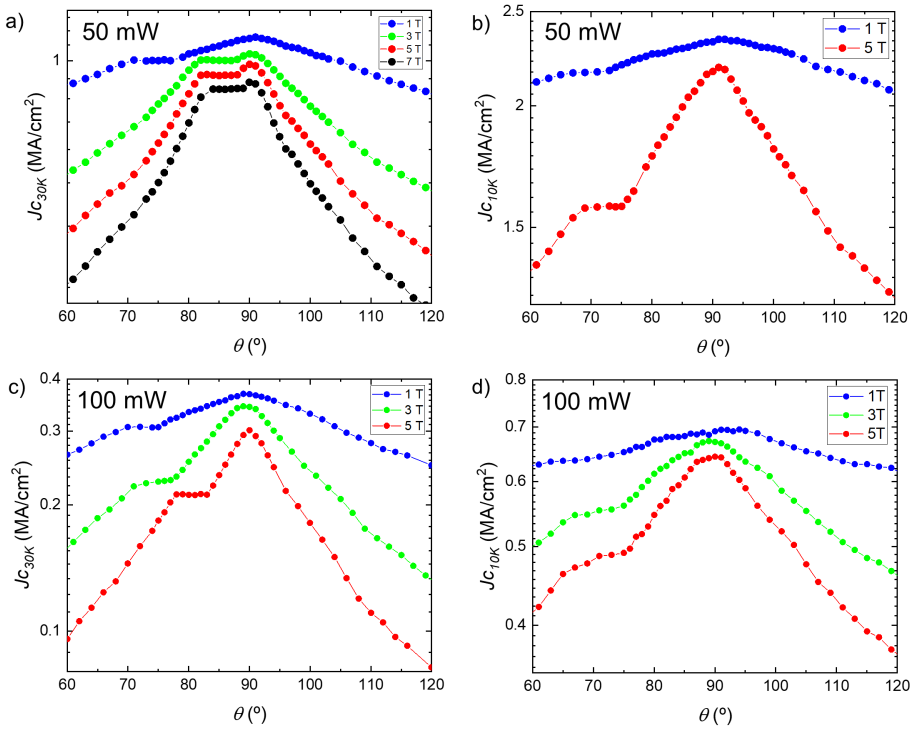



Figure 5.15: Critical current density dependence on the magnetic field orientation for devices irradiated at 50 mW and 100 mW at different magnetic fields and temperatures (10 K and 30 K).

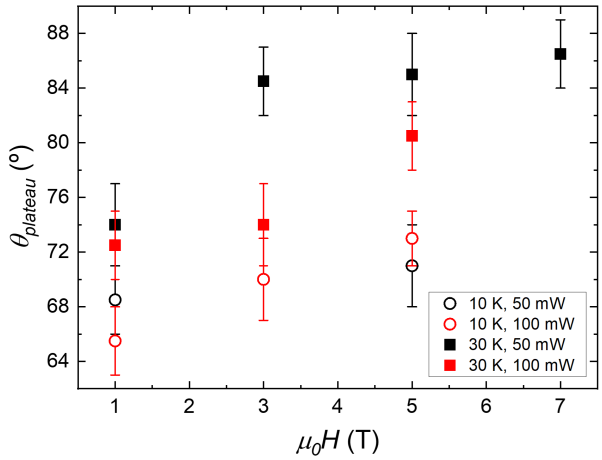



Figure 5.16: Values of $\theta_{plateu}$ as a function of the magnetic field for irradiated at 50 mW and 100 mW at 10K (open symbols) and 30 K (closed symbols). Error bars represents the length of the plateau.

Although a plateau in $\theta_{plateau}$ may be associated to the presence of laser-induced pinning centres in these particular directions, the origin of this pinning is not clear. Fig.5.17 shows a complete $J_c(\theta)$ curve obtained by increasing the rotation angle from 0 ° to 360 ° and decreasing it again to 0 °. Interestingly, the plateau is not symmetric around 90 ° and it just appears ($\sim$ 30 °) below 90 ° in the positive sweep and above 270 ° in the negative sweep. A representation of the magnetic field orientation at the plateau and rotation angle is depicted in Fig.5.17. Further investigations may be performed in order to clearly identify the origin of laser-induced pinning centres which according to the obtained results is highly anisotropic.

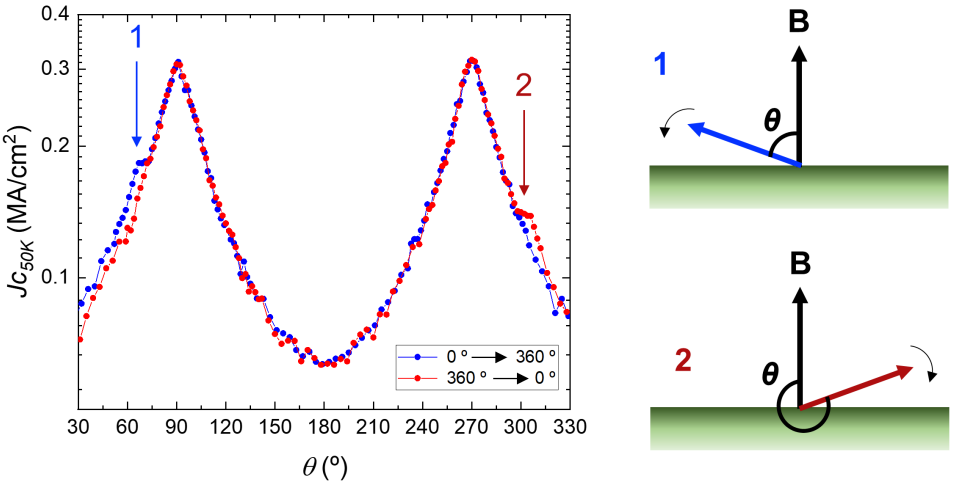



Figure 5.17: a) Critical current density dependence on the magnetic field orientation for the device irradiated at 50 mW at 50 K and $\mu_0 H = 1$ T. Black arrows indicate the $J_c$ plateaus. b) Sketch of field orientation and rotation direction at the plateau.

### 5.3.3 Local laser irradiation: Pattern with lines

In this section we evaluate the possibility to locally modify parts of the track by irradiating it with lines (D15-3 in Fig.5.7, and D20-3 and D20-4 in Fig.5.8). Fig.5.18a shows the resistance vs. temperature curves measured for devices with lines as compared with a pristine track. We observe that in all the cases a double transition is obtained indicating the presence of two marked regions with different $T_c$. The first transition ($T_1$) is associated to unpatterned regions and the second

one ($T_2$) to the regions patterned with lines. The double transition is less marked in the 15-nm sample irradiated at 175 mW probably because the power is too high and the two regions with different doping are not so clearly differentiated.

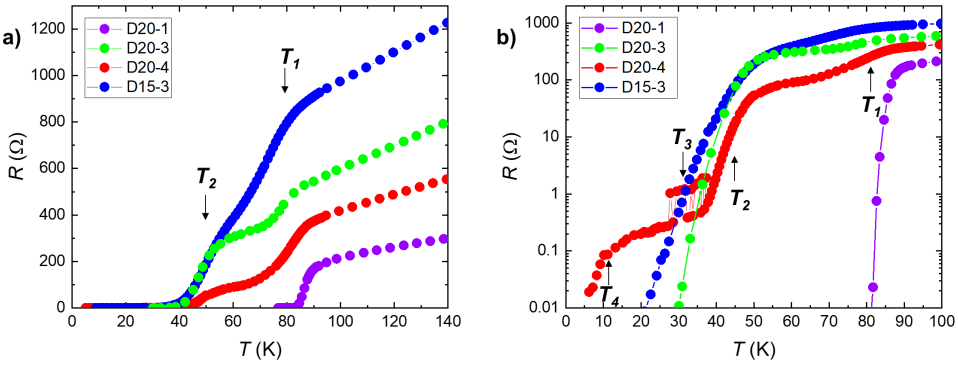



Figure 5.18: a) Resistance vs. temperature curves obtained for several devices patterned with lines in a) linear scale and b) log scale.

Fig.5.18b shows the same data in log scale. In this graph we can clearly see that the sample irradiated with lines at different power (identify the presence of four different $T_c$ values (D20-4 in Fig.5.8) show four different transitions. $T_1$ and $T_2$ as the samples irradiated with homogeneous lines and $T_3$ and $T_4$ that may be associated to regions with different oxygen doping. These results are very interesting since indicate that it is possible to locally modify the oxygen doping in the sample in a very controlled way.

## 5.4 Conclusions

The focus of this chapter was to modify the oxygen doping of YBCO films by using laser-induced thermal effects. Initially, the influence of different laser parameters on the irradiation effects were evaluated. The affected areas could be directly visualized by optical microscope and CAFM. The brightness of the optical images could be directly correlated with the laser patterning and the associated sample de-oxygenation. CAFM measurements revealed enhanced surface conductivity in patterned regions which should be associated to a local oxygen accumulation at the surface.

A systematic study performed by changing the laser power demonstrated the possibility to modulate the critical current density (oxygen content) of YBCO tracks. By using homogeneous sample irradiation at different powers a temperature-doping phase diagram with the critical temperature ($T_c$) and pseudogap temperature ($T^*$) of samples switched to different under-doped levels have been generated, reproducing the one expected for cuprate films. In the case of in-homogeneous irradiation using lines we observed that different transitions can be induced, associated to regions with different oxygen content demonstrating the possibility to locally modify the material at micro-metric scale.

Critical current density measurements as a function of the temperature, magnetic field value and orientation have been performed in several YBCO devices irradiated at different laser powers. Measurements have been used to identify the effects generated through laser-induced oxygen diffusion. Very interesting plateaus around the *ab*-peak were found in the patterned devices which should be associated to highly anisotropic pinning centres efficient at specific magnetic field orientations.

# Chapter 6

# General Conclusions

Throughout this thesis, we have investigated different methods to tune the superconducting properties of YBCO films. The first one is by tailoring their vortex pinning landscape through growing conditions by using low Barium precursor solutions. The second approach is by changing the oxygen doping in the material by field-effect oxygen diffusion or laser-induced thermal effects.

**Chapter 3** investigates the impact of growing temperature on the superconducting performance of YBCO films grown by chemical solution deposition using low Ba precursor solutions. These solutions, distinguished for being straightforward, inexpensive and eco-friendly, allow us to reduce the growing temperature of YBCO down to 750 °C. We investigated the influence of the growing temperatures on both the microstructure and superconducting properties of YBCO films by using conventional thermal annealing (CA) and flash-heating (FH) approaches.

A clear correlation between the growing temperature and the superconducting performance of the films was obtained with improved performances observed at 750 °C. The effective pinning landscape induced in the samples grown at low temperature is associated with the formation of a high-density of stacking faults, observed by TEM images. Moreover, those films show very high values of $J_c^{sf}$ which may be associated to a large carrier concentration at the overdoped state. It is worth pointing out that the combined effect of Ba-deficient precursor solution, low temperature growth and the addition of artificial defects (nanoparticles) may boost the pining performance of the films.

**Chapter 4** shows the potential of reversible, nonvolatile field-induced oxygen doping for a systematic tuning of the carrier density in YBCO films, which in turn is substantial and shows robust effects in the bulk critical temperature and electric properties at the normal state. We evidence that direct gating of metal-insulating transition induced by oxygen diffusion, appears as a very appealing for resistive switching devices in which the resistive ratio between the low and high resistance state increases by decreasing the gate size. A ratio of 5 orders of magnitude have been achieved by using micro-metric gates.

Field-induced resistive switching effects have been used to study the superconducting properties of YBCO films at different oxygen doping levels and thus identify the kind of defects generated. Reversible changes in the critical temperature and superconducting critical current density are achieved by transitioning from a pristine low resistance state to reversible high resistance states with moderate oxygen-depleted regions. Transmission electron microscopy (TEM) measurements, aligned with $J_c(H)$ and $J_c(\theta)$ dependencies, reveal that when large oxygen depletion is induced, various irreversible high resistance states can be obtained with the presence of stacking faults. These findings offer valuable insights into understanding the role of defects induced by field-induced oxygen diffusion in the switching performance of cuprate superconductors.

**Chapter 5** is devoted to investigate the possibility to induce metal-insulating transitions through thermal effects generated by direct laser writing. The generation of laser-induced oxygen vacancies have been directly visualized by an increased reflectivity in optical images. A clear correlation of the reflectivity change with the irradiation pattern an laser power used could be obtained. Surprisingly an enhancement of the conductivity in the irradiated zones have been detected by CAFM measurements that could be ascribed to a local oxygenation of the film surface.

Low-temperature angular transport measurements have been used to explore the pinning performance of irradiated samples. We observed that contrary to what we found with field-induced oxygen doping, no presence of stacking faults have been observed in the case of laser-induced oxygen diffusion. However, very a very interesting and unex-

pected $J_c(\theta)$ plateau have been observed in all the irradiated samples which depend on the magnetic field, temperature and laser power. Further investigations may be performed in order to elucidate the origin of the pinning centres that create this plateau. The potential of the technique has been elucidated by designing non-homogeneous patterning (lines) in which we could observe that different transitions could be induced. This approach may be interesting for technological applications since it offers the possibility to nano-engineer the superconducting order parameter at very local scale with a very high design flexibility.

The results obtained in **Chapter 4** and **Chapter 5** have been used to recreate most of the phase diagram of YBCO, covering a wide range of doping states(Fig.6.1). The systematic control of the oxygen content in superconducting cuprates by means of external inputs (electric field or laser irradiation) may be used to study their complex phase diagrams and opens new routes for the design of superconducting devices with improved functionalities.

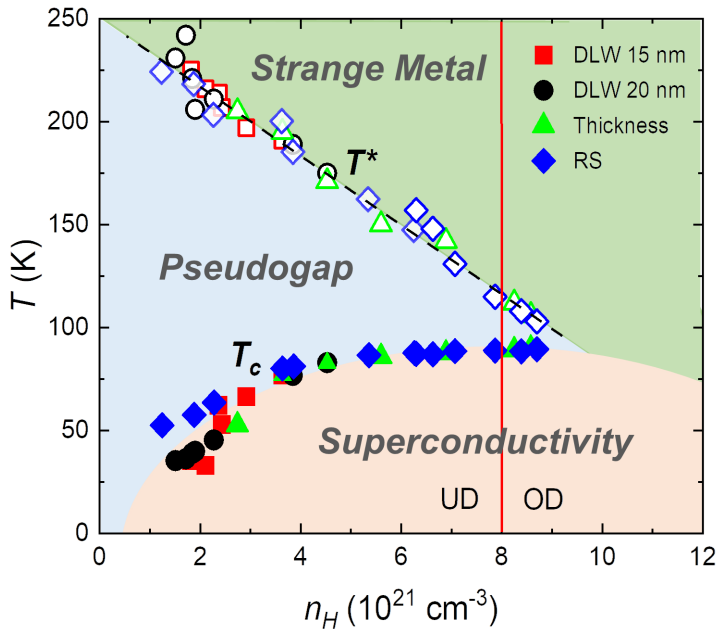



Figure 6.1: Temperature-doping phase diagram of YBCO obtained with the different samples analyzed in this theses. Red line divides the under-doped (UD) and over-doped (OD) regions.

# Publications

A. Fernández-Rodríguez, **J. Alcalà**, J. Sune, N. Mestres, and A. Palau. Multi-Terminal Transistor-Like Devices Based on Strongly Correlated Metallic Oxides for Neuromorphic Applications. *Materials*, 13(2):281, 2020.

E. Bartolomé, **J. Alcalà**, F. Vallès, T. Puig, X. Obradors, N. Pompeo, A. Alimenti, K. Torokhtii, F. Rizzo, A. Augieri, G. Celentano, E. Silva, and A. Palau. Vortex pinning properties at dc and microwave frequencies of YBa2Cu3O7-x films with nanorods and nanoparticles. *Superconductor Science and Technology*, 33(7):74006–74016, 2020.

P. Ternero, **J. Alcalà**, L. Piperno, C. Pop, S. Ricart, N. Mestres, X. Obradors, T. Puig, G. Sotgiu, G. Celentano, and A. Palau. Low-Fluorine Ba-Deficient Solutions for High-Performance Superconducting YBCO Films. *Coatings*, 11(2):199, 2021.

**J. Alcalà**, M. Roig, S. Martín, A. Barrera, A. Fernández-Rodríguez, A. Pomar, L. Balcells, M. Coll, N. Mestres, A. Palau. Potential of Copper Oxide High-Temperature Superconductors for Tailoring Ferromagnetic Spin Textures, In book: Surfaces and Interfaces of Metal Oxide Thin Films, Multilayers, Nanoparticles and Nanocomposites. *Springer, Cham.* 167-182, 2021.

**J. Alcalà**, P. Ternero, C. Pop, L. Piperno, S. Ricart, N. Mestres, T. Puig, X. Obradors, A. Meledin, G. Celentano, and A. Palau. Influence of growth temperature on the pinning landscape of YBa2Cu3O7-$\delta$ films grown from Ba-deficient solutions. *Superconductor Science and Technology*, 35(10):104004, 2022.

**J. Alcalà**, U. Bhattacharya, J. Biegert, M. Ciappina, U. Elu, T. Graß, P.T. Grochowski, M. Lewenstein, A. Palau, T.P.H. Sidiropoulos, T. Steinle, and I. Tyulnev. High-harmonic spectroscopy of quantum phase transitions in a high-Tc superconductor. *Proceedings of the National Academy of Sciences of the United States of America*, 119(40):e2207766119, 2022.

A. Barrera, E. Fourneau, S. Martín, J. M. Batllori, **J. Alcalà**, L. Balcells, N. Mestres, N. D. Nguyen, A. Sanchez, A. V. Silhanek and A. Palau. Tunable Perpendicular Magnetoresistive Sensor Driven by Shape and Substrate Induced Magnetic Anisotropy. *Advanced Sensor Research*, 2(2):2200042, 2022.

P. Machado, R. Guzmán, R. J. Morera, **J. Alcalà**, A. Palau, W. Zhou and M. Coll. Chemical Synthesis of $La_{0.75}Sr_{0.25}CrO_3$ Thin Films for p-Type Transparent Conducting Electrodes. *Chem. Mater.* 35(9):3513–3521, 2023.

**J. Alcalà**, A. Fernández-Rodríguez, T. Günkel, A. Barrera, M. Cabero, J. Gazquez, L. Balcells, N. Mestres and A. Palau. Tuning the superconducting performance of $YBa_2Cu_3O_{7-\delta}$ films through field-induced oxygen doping. *Scientific Reports* 14:1939, 2024.

# Bibliography


[1] J. De Nobel and P. Lindenfeld. The Discovery of Superconductivity. *Physics Today*, 49(9):40–42, 1996.

[2] D. Van Delft and P. Kes. The discovery of superconductivity. *Physics Today*, 63(9):38–43, 2010.

[3] R. de Bruyn Ouboter. Heike Kamerlingh Onnes's Discovery of Superconductivity. *Scientific American*, 276(3):98–103, 1997.

[4] W. Meissner and R. Ochsenfeld. Ein neuer Effekt bei Eintritt der Supraleitfähigkeit. *Die Naturwissenschaften*, 21(44):787–788, 1933.

[5] C Kittel. *Introduction to solid state physics*. John Wiley & Sons, Inc., 2005.

[6] R. P Huebener. *Magnetic Flux Structures in Superconductors*, volume 6. Springer Berlin Heidelberg, 2001.

[7] G. Grosso and G. P. Parravicini. Superconductivity. In *Solid State Physics*, pages 789–849. Academic Press, 2014.

[8] L.D. Landau. On the Theory of Superconductivity. In *Collected Papers of L.D. Landau*, pages 546–568. Pergamon, 1965.

[9] V. L. Ginzburg and L. D. Landau. On the Theory of Superconductivity. In *On Superconductivity and Superfluidity*, pages 113–137. Springer, Berlin, Heidelberg, 2009.

[10] M. Tinkham. *Introduction to superconductivity*. Dover Publications, 2nd edition, 2004.

[11] G. Blatter, M. V. Feigel'Man, V. B. Geshkenbein, A. I. Larkin, and V. M. Vinokur. Vortices in high-temperature superconductors. *Reviews of Modern Physics*, 66(4):1125, 1994.

[12] J. R. Waldram. *Superconductivity of metals and cuprates*. Institute of Physics Publishing, 1996.

[13] V. V. Shmidt and G. S. Mkrtchyan. Vortices in type-ll superconductors. *Soviet Physics - Uspekhi*, 17(2):170–185, 1974.

[14] S. J. Chapman and G. Richardson. Motion of Vortices in Type II Superconductors. *Journal on Applied Mathematics*, 55(5):1275–1296, 2006.

[15] B. Rosenstein and D. Li. Ginzburg-Landau theory of type II superconductors in magnetic field. *Reviews of Modern Physics*, 82(1):109–168, 2009.

[16] A. A. Abrikosov. On the Magnetic Properties of Superconductors of the Second Group. *Soviet Phys. JETP*, 5:1174, 1957.

[17] A. A. Abrikosov. Nobel Lecture: Type-II superconductors and the vortex lattice. *Reviews of Modern Physics*, 76(3 I):975–979, 2004.

[18] H. F. Hess, R. B. Robinson, R. C. Dynes, J. M. Valles, and J. V. Waszczak. Scanning-Tunneling-Microscope Observation of the Abrikosov Flux Lattice and the Density of States near and inside a Fluxoid. *Physical Review Letters*, 62(2):214, 1989.

[19] H. Ullmaier. Irreversible Properties of Type II Superconductors. *New York: Springer-Verlag*, 76, 1975.

[20] C. P. Bean. Magnetization of Hard Superconductors. *Physical Review Letters*, 8(6):250, 1962.

[21] C.P. Bean. Magnetization of High-Field Superconductors. *Reviews of Modern Physics*, 36(1):31, 1964.

[22] D. X. Chen and R. B. Goldfarb. Kim model for magnetization of type-II superconductors. *JAP*, 66(6):2489–2500, 1989.

[23] A. Sanchez and C. Navau. Critical-current density from magnetization loops of finite high-Tc superconductors. *Superconductor Science and Technology*, 14(7):444, 2001.

[24] D.X. Chen, C. Prados, E. Pardo, A. Sanchez, and A. Hernando. Transverse demagnetizing factors of long rectangular bars: I. Analytical expressions for extreme values of susceptibility. *Journal of Applied Physics*, 91:5254, 2002.

[25] E. Pardo, A. Sanchez, and D. X. Chen. Transverse demagnetizing factors of long rectangular bars. II. Numerical calculations for arbitrary susceptibility. *Journal of Applied Physics*, 91(8):5260–5267, 2002.

[26] J. Bardeen, L. N. Cooper, and J. R. Schrieffer. Theory of superconductivity. *Physical Review*, 108(5):1175–1204, 1957.

[27] J. Bardeen, L. N. Cooper, and J. R. Schrieffer. Microscopic Theory of Superconductivity. *Physical Review*, 106(1):162, 1957.

[28] W. S. Corak, B. B. Goodman, C. B. Satterthwaite, and A. Wexler. Exponential Temperature Dependence of the Electronic Specific Heat of Superconducting Vanadium. *Physical Review*, 96(5):1442, 1954.

[29] E. Maxwell. Isotope Effect in the Superconductivity of Mercury. *Physical Review*, 78(4):477, 1950.

[30] C. A. Reynolds, B. Serin, W. H. Wright, and L. B. Nesbitt. Superconductivity of Isotopes of Mercury. *Physical Review*, 78(4):487, 1950.

[31] B. D. Josephson. Possible new effects in superconductive tunnelling. *Physics Letters*, 1(7):251–253, 1962.

[32] B. D. Josephson. The discovery of tunnelling supercurrents. *Reviews of Modern Physics*, 46(2):251–254, 1974.

[33] A. Barone and G. Paternò. *Physics and Applications of the Josephson Effect*. Wiley, 1982.

[34] J. G. Bednorz and K. A. Müller. Possible high Tc superconductivity in the Ba-La-Cu-O system. *Zeitschrift für Physik B Condensed Matter*, 64(2):189–193, 1986.

[35] A. P. Drozdov, M. I. Eremets, I. A. Troyan, V. Ksenofontov, and S. I. Shylin. Conventional superconductivity at 203 kelvin at high pressures in the sulfur hydride system. *Nature*, 525(7567):73–76, 2015.

[36] D. Duan, Y. Liu, F. Tian, D. Li, X. Huang, Z. Zhao, H. Yu, B. Liu, W. Tian, and T. Cui. Pressure-induced metallization of dense (H2S)2H2 with high-Tc superconductivity. *Scientific Reports*, 4(1):1–6, 2014.

[37] P. J. Ray. Structural investigation of La(2-x)Sr(x)CuO(4+y) - Following staging as a function of temperature. *Master's Thesis*, 2016.

[38] T.P. Sheahen. *Introduction to high-temperature superconductivity*. Plenum Press, 1994.

[39] Y. Kamihara, T. Watanabe, M. Hirano, and H. Hosono. Iron-based layered superconductor La[O1-xFx]FeAs (x= 0.05-0.12) with Tc = 26 K. *Journal of the American Chemical Society*, 130(11):3296–3297, 2008.

[40] A. A. Kordyuk. Iron-based superconductors: Magnetism, superconductivity, and electronic structure. *Low Temperature Physics*, 38(9):888–899, 2012.

[41] M. K. Wu, J. R. Ashburn, C. J. Torng, P. H. Hor, R. L. Meng, L. Gao, Z. J. Huang, Y. Q. Wang, and C. W. Chu. Superconductivity at 93K in a new mixed-phase Y-Ba-Cu-O compound system at ambient pressure. *Physical Review Letters*, 58(9):908, 1987.

[42] J. L. Tallon, C. Bernhard, H. Shaked, R. L. Hitterman, and J. D. Jorgensen. Generic superconducting phase behavior in high-Tc cuprates: Tc variation with hole concentration in YBa2Cu3O7-$\delta$. *Physical Review B*, 51(18):12911, 1995.

[43] E. F. Talantsev, N. M. Strickland, S. C. Wimbush, J. G. Storey, J. L. Tallon, and N. J. Long. Hole doping dependence of critical current density in YBa2Cu3O7-$\delta$ conductors. *Applied Physics Letters*, 104(24), 2014.

[44] W. Tabis, Y. Li, M. Le Tacon, L. Braicovich, A. Kreyssig, M. Minola, G. Dellea, E. Weschke, M. J. Veit, M. Ramazanoglu, A. I. Goldman, T. Schmitt, G. Ghiringhelli, N. Barišić, M. K. Chan, C. J. Dorow, G. Yu, X. Zhao, B. Keimer, and M. Greven. Charge order and its connection with Fermi-liquid charge transport in a pristine high-Tc cuprate. *Nature Communications*, 5(1):1–6, 2014.

[45] V. Breit, P. Schweiss, R. Hauff, H. Wuhl, H. Claus, H. Rietschel, A. Erb, and G. Muller-Vogt. Evidence for chain superconductivity in near-stoichiometric YBa2Cu3Ox single crystals. *Physical Review B*, 52(22):R15727, 1995.

[46] M. A. Beno, L. Soderholm, D. W. Capone, D. G. Hinks, J. D. Jorgensen, J. D. Grace, Ivan K. Schuller, C. U. Segre, and K. Zhang. Structure of the single-phase high-temperature superconductor YBa2Cu3O7-$\delta$. *Applied Physics Letters*, 51(1):57–59, 1987.

[47] X. Obradors, T. Puig, A. Palau, A. Pomar, F. Sandiumenge, P. Mele, and K. Matsumoto. Nanostructured Superconductors with Efficient Vortex Pinning. In *Comprehensive Nanoscience and Technology*, volume 1-5, pages 303–349. Academic Press, 2011.

[48] D. Larbalestier, A. Gurevich, D. M. Feldmann, and A. Polyanskii. High-Tc superconducting materials for electric power applications. *Nature*, 414(6861):368–377, 2001.

[49] A. Xu, J. Jaroszynski, F. Kametani, and D. Larbalestier. Broad temperature range study of Jc and Hirr anisotropy in YBa2Cu3Ox thin films containing either Y2O3 nanoparticles or stacking faults. *Applied Physics Letters*, 106(5):52603, 2015.

[50] E. Bartolomé, F. Vallés, A. Palau, V. Rouco, N. Pompeo, F. F. Balakirev, B. Maiorov, L. Civale, T. Puig, X. Obradors, and E. Silva. Intrinsic anisotropy versus effective pinning anisotropy

in YBa2Cu3O7 thin films and nanocomposites. *Physical Review B*, 100(5):054502, 2019.

[51] G. Blatter, V. B. Geshkenbein, and A. I. Larkin. From isotropic to anisotropic superconductors: A scaling approach. *Physical Review Letters*, 68(6):875, 1992.

[52] F. Bouquet, C. Marcenat, E. Steep, R. Calemczuk, W. K. Kwok, U. Welp, G. W. Crabtree, R. A. Fisher, N. E. Phillips, and A. Schilling. An unusual phase transition to a second liquid vortex phase in the superconductor YBa2Cu3O7. *Nature*, 411(6836):448–451, 2001.

[53] M. P.A. Fisher. Vortex-glass superconductivity: A possible new phase in bulk high-Tc oxides. *Physical Review Letters*, 62(12):1415, 1989.

[54] C. Yao and Y. Ma. Superconducting materials: Challenges and opportunities for large-scale applications. *iScience*, 24(6):102541, 2021.

[55] A. Gurevich. To use or not to use cool superconductors? *Nature Materials*, 10(4):255–259, 2011.

[56] J. Kumar, D. Sharma, P. K. Ahluwalia, and V. P.S. Awana. Enhanced superconducting performance of melt quenched Bi2Sr2CaCu2O8 (Bi-2212) superconductor. *Materials Chemistry and Physics*, 139(2-3):681–688, 2013.

[57] W. Jiang, N. C. Yeh, D. S. Reed, U. Kriplani, D. A. Beam, M. Konczykowski, T. A. Tombrello, and F. Holtzberg. Evidence of a Bose-glass transition in superconducting YBa2Cu3O7 single crystals with columnar defects. *Physical Review Letters*, 72(4):550, 1994.

[58] D.R. Nelson and V. M. Vinokur. Boson localization and correlated pinning of superconducting vortex arrays. *Physical Review B*, 48(17):13060, 1993.

[59] D. R. Nelson and V. M. Vinokur. Boson localization and pinning by correlated disorder in high-temperature superconductors. *Physical Review Letters*, 68(15):2398, 1992.

[60] D. S. Fisher, M P.A. Fisher, and D. A. Huse. Thermal fluctuations, quenched disorder, phase transitions, and transport in type-II superconductors. *Physical Review B*, 43(1):130, 1991.

[61] A. Palau, F. Valles, V. Rouco, M. Coll, Z. Li, C. Pop, B. Mundet, J. Gazquez, R. Guzman, J. Gutierrez, X. Obradors, and T. Puig. Disentangling vortex pinning landscape in chemical solution deposited superconducting YBa2Cu3O7-x films and nanocomposites. *Superconductor Science and Technology*, 31(3):034004, 2018.

[62] N. Haberkorn, J. Kim, S. Suárez, J.H. Lee, and S. H. Moon. Influence of random point defects introduced by proton irradiation on the flux creep rates and magnetic field dependence of the critical current density Jc of co-evaporated GdBa2Cu3O7-$\delta$ coated conductors. *Superconductor Science and Technology*, 28(12):125007, 2015.

[63] S. R. Foltyn, L. Civale, J. L. Macmanus-Driscoll, Q. X. Jia, B. Maiorov, H. Wang, and M. Maley. Materials science challenges for high-temperature superconducting wire. *Nature Materials*, 6(9):631–642, 2007.

[64] J. L. Macmanus-Driscoll, S. R. Foltyn, Q. X. Jia, H. Wang, A. Serquis, L. Civale, B. Maiorov, M. E. Hawley, M. P. Maley, and D. E. Peterson. Strongly enhanced current densities in superconducting coated conductors of YBa2Cu3O7-x + BaZrO3. *Nature Materials*, 3(7):439–443, 2004.

[65] A. Goyal, S. Kang, K. J. Leonard, P. M. Martin, A. A. Gapud, M. Varela, M. Paranthaman, A. O. Ijaduola, E. D. Specht, J. R. Thompson, D. K. Christen, S. J. Pennycook, and F. A. List. Irradiation-free, columnar defects comprised of self-assembled nanodots and nanorods resulting in strongly enhanced flux-pinning in YBa2Cu3O7-$\delta$ films. *Superconductor Science and Technology*, 18(11):1533, 2005.

[66] B. Dam, J. M. Huijbregtse, and J. H. Rector. Strong pinning linear defects formed at the coherent growth transition of pulsed-laser-deposited YBa2Cu3O7-$\delta$. *Physical Review B*, 65(6):064528, 2002.

[67] Y. Yamada, K. Takahashi, H. Kobayashi, M. Konishi, T. Watanabe, A. Ibi, T. Muroga, S. Miyata, T. Kato, T. Hirayama, and Y. Shiohara. Epitaxial nanostructure and defects effective for pinning in Y(RE)Ba2Cu3O7-x coated conductors. *Applied Physics Letters*, 87(13):1–3, 2005.

[68] L. Civale. Vortex pinning and creep in high-temperature superconductors with columnar defects. *Superconductor Science and Technology*, 10(7A):A11–A28, 1997.

[69] S. H. Wee, A. Goyal, J. Li, Y. L. Zuev, S. Cook, and L. Heatherly. The incorporation of nanoscale columnar defects comprised of self-assembled BaZrO3 nanodots to improve the flux pinning and critical current density of NdBa2Cu3O7-$\delta$ films grown on RABiTS. *Superconductor Science and Technology*, 20(8):789–793, 2007.

[70] M. Peurla, H. Huhtinen, M. A. Shakhov, K. Traito, Yu P. Stepanov, M. Safonchik, P. Paturi, Y. Y. Tse, R. Palai, and R. Laiho. Effects of nanocrystalline target and columnar defects on flux pinning in pure and BaZrO3 -doped YBa2Cu3O6+x films in fields up to 30T. *Physical Review B - Condensed Matter and Materials Physics*, 75(18):184524, 2007.

[71] A. Díaz, L. Mechin, P. Berghuis, and J. E. Evetts. Evidence for Vortex Pinning by Dislocations in YBa2Cu3O7-$\delta$ Low-Angle Grain Boundaries. *Physical Review Letters*, 80(17):3855, 1998.

[72] A. Palau, T. Puig, J. Gutierrez, X. Obradors, and F. De La Cruz. Pinning regimes of grain boundary vortices in YBa2Cu3O7-x coated conductors. *Physical Review B - Condensed Matter and Materials Physics*, 73(13):132508, 2006.

[73] J. Z. Liu, Y. X. Jia, R. N. Shelton, and M. J. Fluss. In-plane anisotropy of the interaction between vortex and twin boundary in YBa2Cu3O7 single crystals. *Physical Review Letters*, 66(10):1354, 1991.

[74] H. Yamasaki, Y. Nakagawa, A. Sawa, H. Obara, and K. Develos. Flux pinning effects of twin boundaries studied with unidirectionally twinned YBCO films. *Physica C: Superconductivity*, 372-376(376):1885–1889, 2002.

[75] G. Blatter, J. Rhyner, and V. M. Vinokur. Vortex pinning by twin boundaries in copper oxide superconductors. *Physical Review B*, 43(10):7826, 1991.

[76] H. Yamasaki, K. Ohki, I. Yamaguchi, M. Sohma, W. Kondo, H. Matsui, T. Manabe, and T. Kumagai. Strong flux pinning due to dislocations associated with stacking faults in YBa2Cu3O7-$\delta$ thin films prepared by fluorine-free metal organic deposition. *Superconductor Science and Technology*, 23(10):105004, 2010.

[77] J. Gutiérrez, B. Maiorov, T. Puig, J. Gzquez, N. Rom, H. Wang, F. Sandiumenge, and X. Obradors. The role of stacking faults in the critical current density of MOD films through a thickness dependence study. *Superconductor Science and Technology*, 22(1):015022, 2008.

[78] V. Rouco, A. Palau, R. Guzman, J. Gazquez, M. Coll, X. Obradors, and T. Puig. Role of twin boundaries on vortex pinning of CSD YBCO nanocomposites. *Superconductor Science and Technology*, 27(12):125009, 2014.

[79] L. Opherden, M. Sieger, P. Pahlke, R. Huhne, L. Schultz, A. Meledin, G. Van Tendeloo, R. Nast, B. Holzapfel, M. Bianchetti, J.L. MacManus-Driscoll, and J. Hanisch. Large pinning forces and matching effects in YBa2Cu3O7-$\delta$ thin films with Ba2Y(Nb/Ta)O6 nano-precipitates. *Scientific Reports*, 6(1):1–10, 2016.

[80] P. Mele, K. Matsumoto, T. Horide, A. Ichinose, M. Mukaida, Y. Yoshida, and S. Horii. Enhanced high-field performance in PLD films fabricated by ablation of YSZ-added YBa2Cu3O7-x target. *Superconductor Science and Technology*, 20(3):244, 2007.

[81] V. F. Solovyov, H. J. Wiesmann, L. Wu, Q. Li, L. D. Cooley, M. Suenaga, B. Maiorov, and L. Civale. High critical currents by isotropic magnetic-flux-pinning centres in a 3 µm-thick YBa2Cu3O7 superconducting coated conductor. *Superconductor Science and Technology*, 20(4):L20, 2007.

[82] P. Mele, K. Matsumoto, T. Horide, A. Ichinose, M. Mukaida, Y. Yoshida, and S. Horii. Insertion of nanoparticulate artificial pinning centres in YBa2Cu3O7-x films by laser ablation of a

Y2O3-surface modified target. *Superconductor Science and Technology*, 20(7):616, 2007.

[83] A. Llordés, A. Palau, J. Gázquez, M. Coll, R. Vlad, A. Pomar, J. Arbiol, R. Guzmán, S. Ye, V. Rouco, F. Sandiumenge, S. Ricart, T. Puig, M. Varela, D. Chateigner, J. Vanacken, J. Gutiérrez, V. Moshchalkov, G. Deutscher, C. Magen, and X. Obradors. Nanoscale strain-induced pair suppression as a vortex-pinning mechanism in high-temperature superconductors. *Nature Materials*, 11(4):329–336, 2012.

[84] J. Gutiérrez, A. Llordés, J. Gázquez, M. Gibert, N. Romà, S. Ricart, A. Pomar, F. Sandiumenge, N. Mestres, T. Puig, and X. Obradors. Strong isotropic flux pinning in solution-derived YBa2Cu3O7-x nanocomposite superconductor films. *Nature Materials*, 6(5):367–373, 2007.

[85] P. Mele, K. Matsumoto, T. Horide, A. Ichinose, M. Mukaida, Y. Yoshida, S. Horii, and R. Kita. Incorporation of double artificial pinning centers in YBa2Cu3O7-d films. *Superconductor Science and Technology*, 21(1):015019, 2007.

[86] B. Maiorov, A. Kursumovic, L. Stan, H. Zhou, H. Wang, L. Civale, R. Feenstra, and J. L. MacManus-Driscoll. Vortex pinning landscape in YBa2Cu3O7 films grown by hybrid liquid phase epitaxy. *Superconductor Science and Technology*, 20(9):S223, 2007.

[87] T. Puig and X. Obradors. Anisotropic Vortex Plasticity in the Liquid State of YBa2Cu3O7: Evidence for Quenched c-Axis Vortex Correlation Length. *Physical Review Letters*, 84(7):1571, 2000.

[88] M. Miura, B. Maiorov, S. A. Baily, N. Haberkorn, J. O. Willis, K. Marken, T. Izumi, Y. Shiohara, and L. Civale. Mixed pinning landscape in nanoparticle-introduced YGdBa2Cu3Oy films grown by metal organic deposition. *Physical Review B - Condensed Matter and Materials Physics*, 83(18):184519, 2011.

[89] B. Maiorov, S. A. Baily, H. Zhou, O. Ugurlu, J. A. Kennison, P. C. Dowden, T. G. Holesinger, S. R. Foltyn, and L. Civale.

Synergetic combination of different types of defect to optimize pinning landscape using BaZrO3-doped YBa2Cu3O7. *Nature Materials*, 8(5):398–404, 2009.

[90] T. Puig, J. Gutiérrez, A. Pomar, A. Llordés, J. Gzquez, S. Ricart, F. Sandiumenge, and X. Obradors. Vortex pinning in chemical solution nanostructured YBCO films. *Superconductor Science and Technology*, 21(3):034008, 2008.

[91] K. Matsumoto, T. Horide, A.K. Jha, P. Mele, Y. Yoshida, and S. Awaji. Irreversibility fields and critical current densities in strongly pinned YBa2Cu3O7-x films with artificial pinning centers. *IEEE Transactions on Applied Superconductivity*, 25(3), 2015.

[92] C. J. Van Der Beek, M. Konczykowski, V. M. Vinokur, T. W. Li, P. H. Kes, and G. W. Crabtree. Vortex Line Pinning and Bose-Glass Dynamics in Heavy-Ion Irradiated Bi2Sr2CaCu2O8+$\delta$ Single Crystals. *Physical Review Letters*, 74(7):1214, 1995.

[93] B. Martínez, X. Obradors, A. Gou, V. Gomis, S. Piñol, J. Fontcuberta, and H. Van Tol. Critical currents and pinning mechanisms in directionally solidified YBa2Cu3O7-Y2BaCuO5 composites. *Physical Review B*, 53(5):2797, 1996.

[94] J. Plain, T. Puig, F. Sandiumenge, X. Obradors, and J. Rabier. Microstructural influence on critical currents and irreversibility line in melt-textured YBa2Cu3O7-x reannealed at high oxygen pressure. *Physical Review B*, 65(10):104526, 2002.

[95] E. Morosan, D. Natelson, A.H. Nevidomskyy, and Q. Si. Strongly Correlated Materials. *Advanced Materials*, 24(36):4896–4923, 2012.

[96] A. Stangl, A. Palau, G. Deutscher, X. Obradors, and T. Puig. Ultra-high critical current densities of superconducting YBa2Cu3O7-$\delta$ thin films in the overdoped state. *Scientific Reports*, 11(1):1–12, 2021.

[97] E. Trabaldo, A. Kalaboukhov, R. Arpaia, E. Wahlberg, F. Lombardi, and T. Bauch. Mapping the Phase Diagram of a

YBa2Cu3O7-$\delta$ Nanowire Through Electromigration. *Physical Review Applied*, 17(2):024021, 2022.

[98] I. M. Vishik. Photoemission perspective on pseudogap, superconducting fluctuations, and charge order in cuprates: a review of recent progress. *Reports on Progress in Physics*, 81(6):062501, 2018.

[99] P. Limelette, A. Georges, D. Jérome, P. Wzietek, P. Metcalf, and J. M. Honig. Universality and critical behavior at the Mott transition. *Science*, 302(5642):89–92, 2003.

[100] J. Jeong, N. Aetukuri, T. Graf, T.D. Schladt, M.G. Samant, and S.S.P. Parkin. Suppression of metal-insulator transition in VO2 by electric field-induced oxygen vacancy formation. *Science*, 339(6126):1402–1405, 2013.

[101] Y. Zhou and S. Ramanathan. Correlated Electron Materials and Field Effect Transistors for Logic: A Review. *Critical Reviews in Solid State and Materials Sciences*, 38(4):286–317, 2013.

[102] C. H. Ahn, A. Bhattacharya, M. Di Ventra, J. N. Eckstein, C. Daniel Frisbie, M. E. Gershenson, A. M. Goldman, I. H. Inoue, J. Mannhart, Andrew J. Millis, Alberto F. Morpurgo, Douglas Natelson, and Jean Marc Triscone. Electrostatic modification of novel materials. *Reviews of Modern Physics*, 78(4):1185–1212, 2006.

[103] V.R. Morrison, R. P. Chatelain, K.L. Tiwari, A. Hendaoui, A. Bruhács, M. Chaker, and B.J. Siwick. A photoinduced metal-like phase of monoclinic VO2 revealed by ultrafast electron diffraction. *Science*, 346(6208):445–448, 2014.

[104] J. Alcalà, U. Bhattacharya, J. Biegert, M. Ciappina, U. Elu, T. Graß, P.T. Grochowski, M. Lewenstein, A. Palau, T.P.H. Sidiropoulos, T. Steinle, and I. Tyulnev. High-harmonic spectroscopy of quantum phase transitions in a high-Tc superconductor. *Proceedings of the National Academy of Sciences of the United States of America*, 119(40):e2207766119, 2022.

[105] R. Waser and M. Aono. Nanoionics-based resistive switching memories. *Nature Materials*, 6(11):833–840, 2007.

[106] E.Y. Tsymbal and H. Kohlstedt. Tunneling across a ferroelectric. *Science*, 313(5784):181–183, 2006.

[107] I. Valov, R. Waser, J.R. Jameson, and M.N. Kozicki. Electrochemical metallization memories-fundamentals, applications, prospects. *Nanotechnology*, 22(28):289502, 2011.

[108] E. Janod, J. Tranchant, B. Corraze, M. Querré, P. Stoliar, M. Rozenberg, T. Cren, D. Roditchev, V. T. Phuoc, M. P. Besland, and L. Cario. Resistive Switching in Mott Insulators and Correlated Systems. *Advanced Functional Materials*, 25(40):6287–6305, 2015.

[109] R. Waser, R. Dittmann, C. Staikov, and K. Szot. Redox-Based Resistive Switching Memories – Nanoionic Mechanisms, Prospects, and Challenges. *Advanced Materials*, 21(25-26):2632–2663, 2009.

[110] S. Bagdzevicius, K. Maas, M. Boudard, and M. Burriel. Interface-type resistive switching in perovskite materials. *Journal of Electroceramics*, 39(1):157–184, 2017.

[111] J.C. Gonzalez-Rosillo, R. Ortega-Hernandez, J. Jareño-Cerulla, E. Miranda, J. Suñe, X. Granados, X. Obradors, A. Palau, and T. Puig. Volume Resistive Switching in metallic perovskite oxides driven by the Metal-Insulator Transition. *Journal of Electroceramics*, 39(1-4):185–196, 2017.

[112] S. Bagdzevicius, M. Boudard, J.M. Caicedo, L. Rapenne, X. Mescot, R. Rodríguez-Lamas, F. Robaut, J. Santiso, and M. Burriel. Superposition of interface and volume type resistive switching in perovskite nanoionic devices. *Journal of Materials Chemistry C*, 7(25):7580–7592, 2019.

[113] J. C. Gonzalez-Rosillo, S. Catalano, I. Maggio-Aprile, M. Gibert, X. Obradors, A. Palau, and T. Puig. Nanoscale Correlations between Metal–Insulator Transition and Resistive Switching Effect in Metallic Perovskite Oxides. *Small*, 16(23):2001307, 2020.

[114] R. Ortega-Hernandez, M. Coll, J.C. Gonzalez-Rosillo, A. Palau, X. Obradors, E. Miranda, T. Puig, and J. Suñe. Resistive switching in CeO2/La0.8Sr0.2MnO3 bilayer for non-volatile memory applications. *Microelectronic Engineering*, 147:37–40, 2015.

[115] A. Fernández-Rodríguez, J. Alcalà, J. Suñe, N. Mestres, and A. Palau. Multi-Terminal Transistor-Like Devices Based on Strongly Correlated Metallic Oxides for Neuromorphic Applications. *Materials*, 13(2):281, 2020.

[116] C. H. Ahn, J. M. Triscone, and J. Mannhart. Electric field effect in correlated oxide systems. *Nature*, 424(6952):1015–1018, 2003.

[117] A.S. Dhoot, S.C. Wimbush, T. Benseman, J. L. MacManus-Driscoll, J. R. Cooper, and R.H. Friend. Increased Tc in Electrolyte-Gated Cuprates. *Advanced Materials*, 22(23):2529–2533, 2010.

[118] K. S. Takahashi, M. Gabay, D. Jaccard, K. Shibuya, T. Ohnishi, M. Lippmaa, and J. M. Triscone. Local switching of two-dimensional superconductivity using the ferroelectric field effect. *Nature*, 441(7090):195–198, 2006.

[119] X. Leng, J. Garcia-Barriocanal, S. Bose, Y. Lee, and A. M. Goldman. Electrostatic control of the evolution from a superconducting phase to an insulating phase in ultrathin YBa2Cu3O7-x films. *Physical Review Letters*, 107(2):027001, 2011.

[120] G. Dubuis, Y. Yacoby, H. Zhou, X. He, A. T. Bollinger, D. Pavuna, R. Pindak, and I. Božović. Oxygen Displacement in Cuprates under Ionic Liquid Field-Effect Gating. *Scientific Reports*, 6(1):1–8, 2016.

[121] A. Crassous, R. Bernard, S. Fusil, K. Bouzehouane, D. Le Bourdais, S. Enouz-Vedrenne, J. Briatico, M. Bibes, A. Barthélémy, and J. E. Villegas. Nanoscale electrostatic manipulation of magnetic flux quanta in ferroelectric/superconductor BiFeO3/YBa2Cu3O7-$\delta$ heterostructures. *Physical Review Letters*, 107(24):247002, 2011.

[122] A.M. Perez-Muñoz, P. Schio, R. Poloni, A. Fernandez-Martinez, A. Rivera-Calzada, J.C. Cezar, E. Salas-Colera, G.R. Castro, J. Kinney, C. Leon, J. Santamaria, J. Garcia-Barriocanal, and A.M. Goldman. In operando evidence of deoxygenation in ionic liquid gating of YBa2Cu3O7-X. *Proceedings of the National Academy of Sciences of the United States of America*, 114(2):215–220, 2017.

[123] S. Marinković, A. Fernández-Rodríguez, S. Collienne, S. B. Alvarez, S. Melinte, B. Maiorov, G. Rius, X. Granados, N. Mestres, A. Palau, and A.V. Silhanek. Direct Visualization of Current-Stimulated Oxygen Migration in YBa2Cu3O7-$\delta$Thin Films. *ACS Nano*, 14(9):11765–11774, 2020.

[124] X. D.A. Baumans, A. Fernández-Rodríguez, N. Mestres, S. Collienne, J. Van de Vondel, A. Palau, and A. V. Silhanek. Electromigration in the dissipative state of high-temperature superconducting bridges. *Applied Physics Letters*, 114(1), 2019.

[125] A. Palau, A. Fernandez-Rodriguez, J.C. Gonzalez-Rosillo, X. Granados, M. Coll, B. Bozzo, R. Ortega-Hernandez, J. Suñé, N. Mestres, X. Obradors, and T. Puig. Electrochemical Tuning of Metal Insulator Transition and Nonvolatile Resistive Switching in Superconducting Films. *ACS Applied Materials and Interfaces*, 10(36):30522–30531, 2018.

[126] X. Obradors, T. Puig, A. Pomar, F. Sandiumenge, S. Piñol, N. Mestres, O. Castaño, M. Coll, A. Cavallaro, A. Palau, J. Gázquez, J. C. González, J. Gutiérrez, N. Romà, S. Ricart, J. M. Moretó, M. D. Rossell, and G. Van Tendeloo. Chemical solution deposition: a path towards low cost coated conductors. *Superconductor Science and Technology*, 17(8):1055, 2004.

[127] T. Schneller and R. Waser. Chemical Solution Deposition of Ferroelectric Thin Films - State of the Art and Recent Trends. *Ferroelectrics*, 267(1):293–301, 2002.

[128] R.W. Schwartz, T. Schneller, and R. Waser. Chemical solution deposition of electronic oxide films. *Comptes Rendus Chimie*, 7(5):433–461, 2004.

[129] G. Hodes. *Chemical Solution Deposition Of Semiconductor Films*. CRC Press, 2002.

[130] R.W. Schwartz. Chemical Solution Deposition of Perovskite Thin Films. *Chemistry of Materials*, 9(11):2325–2340, 1997.

[131] X Obradors, T Puig, S Ricart, M Coll, J Gazquez, A Palau, and X Granados. Growth, nanostructure and vortex pinning in superconducting YBa2Cu3O7 thin films based on trifluoroacetate solutions, 2012.

[132] T. Araki, T. Kato, T. Muroga, T. Niwa, T. Yuasa, H. Kurosaki, Y. Iijima, Y. Yamada, T. Hirayama, T. Saitoh, Y. Shiohara, and I. Hirabayashi. Carbon expelling scheme and required conditions for obtaining high-Jc YBa2Cu3O7-x film by metalorganic deposition using trifluoroacetates. *IEEE Transactions on Applied Superconductivity*, 13(2):2803–2808, 2003.

[133] A. Calleja, S. Ricart, X. Palmer, R. F. Luccas, T. Puig, and X. Obradors. Water determination of precursor solutions with oxidant cations by the Karl Fischer method: The YBCO-TFA case. *Journal of Sol-Gel Science and Technology*, 53(2):347–352, 2010.

[134] X. Palmer, C. Pop, H. Eloussifi, B. Villarejo, P. Roura, J. Farjas, A. Calleja, A. Palau, X. Obradors, T. Puig, and S. Ricart. Solution design for low-fluorine trifluoroacetate route to YBa2Cu3O7 films. *Superconductor Science and Technology*, 29(2):024002, 2016.

[135] T. Puig, J.C. González, A. Pomar, N. Mestres, O. Castaño, M. Coll, J. Gázquez, F. Sandiumenge, S. Piñol, and X. Obradors. The influence of growth conditions on the microstructure and critical currents of TFA-MOD YBa2Cu3O7 films. *Superconductor Science and Technology*, 18(8):1141, 2005.

[136] P. Cayado, B. Mundet, H. Eloussifi, F. Vallés, M. Coll, S. Ricart, J. Gázquez, A. Palau, P. Roura, J. Farjas, T. Puig, and X. Obradors. Epitaxial superconducting GdBa2Cu3O7-$\delta$ /Gd2O3 nanocomposite thin films from advanced low-fluorine solutions. *Superconductor Science and Technology*, 30(12):125010, 2017.

[137] Z. Li, M. Coll, B. Mundet, N. Chamorro, F. Vallès, A. Palau, J. Gazquez, S. Ricart, T. Puig, and X. Obradors. Control of nanostructure and pinning properties in solution deposited YBa2Cu3O7-x nanocomposites with preformed perovskite nanoparticles. *Scientific Reports*, 9(1), 2019.

[138] Z. Li, M. Coll, B. Mundet, A. Palau, T. Puig, and X. Obradors. Accelerated growth by flash heating of high critical current trifluoroacetate solution derived epitaxial superconduct-

ing YBa2Cu3O7 films. *Journal of Materials Chemistry C*, 7(16):4748–4759, 2019.

[139] R.K. Singh and D. Kumar. Pulsed laser deposition and characterization of high-Tc YBa2Cu3O7-x superconducting thin films. *Materials Science & Engineering R*, 4(22):113–185, 1998.

[140] D. M. Feldmann, O. Ugurlu, B. Maiorov, L. Stan, T. G. Holesinger, L. Civale, S. R. Foltyn, and Q. X. Jia. Influence of growth temperature on critical current and magnetic flux pinning structures in YBa2Cu3O7-x. *Applied Physics Letters*, 91(16), 2007.

[141] S. R. Foltyn, P. N. Arendt, Q. X. Jia, H. Wang, J. L. MacManus-Driscoll, S. Kreiskott, R. F. DePaula, L. Stan, J. R. Groves, and P. C. Dowden. Strongly coupled critical current density values achieved in Y1Ba2Cu3O7-$\delta$ coated conductors with near-single-crystal texture. *Applied Physics Letters*, 82(25):4519–4521, 2003.

[142] L. Civale, B. Maiorov, A. Serquis, J. O. Willis, J. Y. Coulter, H. Wang, Q. X. Jia, P. N. Arendt, M. Jaime, J. L. MacManus-Driscoll, M. P. Maley, and S. R. Foltyn. Understanding high critical currents in YBa2Cu3O7 thin films and coated conductors. *Journal of Low Temperature Physics*, 135(1-2):87–98, 2004.

[143] W.H. Bragg and W.L. Bragg. The reflection of X-rays by crystals. *Proceedings of the Royal Society of London. Series A, Containing Papers of a Mathematical and Physical Character*, 88(605):428–438, 1913.

[144] B. Tlili. Caractérisation de films durs multicouches élaborés par pulvérisation magnétron. Influence des conditions d'élaboration sur leurs propriétés. *Matériaux. Arts et Métiers ParisTech.*, 2010.

[145] M. Lanza. *Conductive Atomic Force Microscopy: Applications in Nanomaterials*. Wiley-VCH Verlag GmbH & Co. KGaA, 2017.

[146] A. Kovács, R. Schierholz, and K. Tillmann. FEI Titan G2 80-200 CREWLEY. *Journal of large-scale research facilities JLSRF*, 2:A43–A43, 2016.

[147] P. D. Nellist and S. J. Pennycook. Incoherent imaging using dynamically scattered coherent electrons. *Ultramicroscopy*, 78(1-4):111–124, 1999.

[148] S.T. Howell, A. Grushina, F. Holzner, and J. Brugger. Thermal scanning probe lithography-a review. *Microsystems & Nanoengineering*, 6(1):1–24, 2020.

[149] E. Albisetti, A. Calò, A. Zanut, X. Zheng, G.M. de Peppo, and E. Riedo. Thermal scanning probe lithography. *Nature Reviews Methods Primers*, 2(1):1–21, 2022.

[150] V. Levati, D. Girardi, N. Pellizzi, M. Panzeri, M. Vitali, D. Petti, and E. Albisetti. Phase Nanoengineering via Thermal Scanning Probe Lithography and Direct Laser Writing. *Advanced Materials Technologies*, 8(16):2300166, 2023.

[151] L. J. van der Pauw. A method of measuring the resistivity and Hall coefficient on lamellae of arbitrary shape. *Philips Technical Review*, 20(8):220–224, 1958.

[152] X. Obradors, T. Puig, A. Pomar, F. Sandiumenge, N. Mestres, M. Coll, A. Cavallaro, N. Romà, J. Gázquez, J.C. González, O. Castaño, J. Gutierrez, A. Palau, K. Zalamova, S. Morlens, A. Hassini, M. Gibert, S. Ricart, J.M. Moretó, S. Piñol, D. Isfort, and J. Bock. Progress towards all-chemical superconducting YBa2Cu3O7-coated conductors. *Superconductor Science and Technology*, 19(3):S13, 2006.

[153] P. Mele, K. Prassides, C. Tarantini, A. Palau, P. Badica, A.K. Jha, and T. Endo. *Superconductivity: From Materials Science to Practical Applications*. Springer Cham, 1 edition, 2020.

[154] H. Padamsee. The science and technology of superconducting cavities for accelerators. *Superconductor Science and Technology*, 14(4):R28, 2001.

[155] D. Di Gioacchino, C. Gatti, D. Alesini, C. Ligi, S. Tocci, A. Rettaroli, G. Carugno, N. Crescini, G. Ruoso, C. Braggio, P. Falferi, C. S. Gallo, U. Gambardella, Gerardo Iannone, Gianluca Lamanna, Augusto Lombardi, Renato Mezzena, Antonello

Ortolan, Ruggero Pengo, Enrico Silva, and Nicola Pompeo. Microwave losses in a DC magnetic field in superconducting cavities for axion studies. *IEEE Transactions on Applied Superconductivity*, 29(5), 2019.

[156] T. Puig, P. Krkotić, A. Romanov, J. O'Callaghan, D. A. Zanin, H. Neupert, P. C. Pinto, P. Demolon, A. Granadeiro Costa, M. Taborelli, F. Perez, M. Pont, J. Gutierrez, and S. Calatroni. Coated conductor technology for the beamscreen chamber of future high energy circular colliders. *Superconductor Science and Technology*, 32(9):094006, 2019.

[157] A. Chen, M. Weigand, Z. Bi, W. Zhang, X. Lü, P. Dowden, J.L. MacManus-Driscoll, H. Wang, and Q. Jia. Evolution of microstructure, strain and physical properties in oxide nanocomposite films. *Scientific Reports*, 4(1):1–7, 2014.

[158] J.L. MacManus-Driscoll and S.C. Wimbush. Processing and application of high-temperature superconducting coated conductors. *Nature Reviews Materials*, 6(7):587–604, 2021.

[159] A.K. Jha, K. Matsumoto, T. Horide, S. Saini, P. Mele, Y. Yoshida, and S. Awaji. Tuning the microstructure and vortex pinning properties of YBCO-based superconducting nanocomposite films by controlling the target rotation speed. *Superconductor Science and Technology*, 27(2):025009, 2013.

[160] F. Rizzo, A. Augieri, A. Angrisani Armenio, V. Galluzzi, A. Mancini, V. Pinto, A. Rufoloni, A. Vannozzi, M. Bianchetti, A. Kursumovic, J. L. MacManus-Driscoll, A. Meledin, G. Van Tendeloo, and G. Celentano. Enhanced 77 K vortex-pinning in y Ba2Cu3O7-x films with Ba2Y TaO6 and mixed Ba2Y TaO6 + Ba2Y NbO6 nano-columnar inclusions with irreversibility field to 11 T. *APL Materials*, 4(6), 2016.

[161] M. Coll, J. Gázquez, R. Hühne, B. Holzapfel, Y. Morilla, J. García-López, A. Pomar, F. Sandiumenge, T. Puig, and X. Obradors. All chemical YBa2Cu3O7 superconducting multilayers: Critical role of CeO2 cap layer flatness. *Journal of Materials Research*, 24(4):1446–1455, 2009.

[162] V.R. Vlad, K. Zalamova, M. Coll, A. Pomar, A. Palau, J. Gutierrez, T. Puig, X. Obradors, and A. Usoskin. Growth of chemical solution deposited TFAYBCO/MOD(Ce, Zr)O2/ABADYSZ/SS Coated Conductors. *IEEE Transactions on Applied Superconductivity*, 19(3):3212–3215, 2009.

[163] T Izumi and K Nakaoka. Control of artificial pinning centers in REBCO coated conductors derived from the trifluoroacetate metal-organic deposition process. *Superconductor Science and Technology*, 31(3):34008, 2018.

[164] M. Coll, R. Guzman, P. Garcés, J. Gazquez, V. Rouco, A. Palau, S. Ye, C. Magen, H. Suo, H. Castro, T. Puig, and X. Obradors. Size-controlled spontaneously segregated Ba2YTaO6 nanoparticles in YBa2Cu3O7 nanocomposites obtained by chemical solution deposition. *Superconductor Science and Technology*, 27(4):044008, 2014.

[165] P. Cayado, K. De Keukeleere, A. Garzón, L. Perez-Mirabet, A. Meledin, J. De Roo, F. Vallés, B. Mundet, H. Rijckaert, G. Pollefeyt, M. Coll, S. Ricart, A. Palau, J. Gázquez, J. Ros, G. Van Tendeloo, I. Van Driessche, T. Puig, and X. Obradors. Epitaxial YBa2Cu3O7-x nanocomposite thin films from colloidal solutions. *Superconductor Science and Technology*, 28(12):124007, 2015.

[166] X. Obradors, T. Puig, Z. Li, C. Pop, B. Mundet, N. Chamorro, F. Vallés, M. Coll, S. Ricart, B. Vallejo, F. Pino, A. Palau, J. Gázquez, J. Ros, and A. Usoskin. Epitaxial YBa2Cu3O7-x nanocomposite films and coated conductors from BaMO3 (M = Zr, Hf) colloidal solutions. *Superconductor Science and Technology*, 31(4):044001, 2018.

[167] A. Palau, E. Bartolomé, A. Llordés, T. Puig, and X. Obradors. Isotropic and anisotropic pinning in TFA-grown YBa2Cu3O7-x films with BaZrO3 nanoparticles. *Superconductor Science and Technology*, 24(12):125010, 2011.

[168] V. Rouco, E. Bartolomé, A. Palau, M. Coll, X. Obradors, and T. Puig. Nanostrain induced pinning in YBa2Cu3O7-x nanocomposites even close to the irreversibility line. *Superconductor Science and Technology*, 25(12):122001, 2012.

[169] F. A. List, P. G. Clem, L. Heatherly, J. T. Dawley, K. J. Leonard, D. F. Lee, and A. Goyal. Low-pressure conversion studies for YBCO precursors derived by PVD and MOD methods. *IEEE Transactions on Applied Superconductivity*, 15(2):2656–2658, 2005.

[170] R. Pratap, G. Majkic, E. Galstyan, G. Mohanasundaram, S. Chakradhar, and V. Selvamanickam. Growth of High-Performance Thick Film REBCO Tapes Using Advanced MOCVD. *IEEE Transactions on Applied Superconductivity*, 29(5), 2019.

[171] E Galstyan, R Pratap, G Majkic, M Kochat, D Abraimov, J Jaroszynski, and V Selvamanickam. In-field critical current and pinning mechanisms at 4.2 K of Zr-Added REBCO coated conductors. *Superconductor Science and Technology*, 33(7):12, 2020.

[172] B.A. Albiss and I.M. Obaidat. Applications of YBCO-coated conductors: A focus on the chemical solution deposition method. *Journal of Materials Chemistry*, 20(10):1836–1845, 2010.

[173] B. Malič, S. Glinšek, T. Schneller, and M. Kosec. Mixed metallo-organic precursor systems. In *Chemical Solution Deposition of Functional Oxide Thin Films*, volume 9783211993, pages 51–69. Springer-Verlag Wien, dec 2013.

[174] P. Vermeir, I. Cardinael, M. Bäcker, J. Schaubroeck, E. Schacht, S. Hoste, and I.V. Driessche. Fluorine-free water-based sol-gel deposition of highly epitaxial YBa2Cu3O7-$\delta$ films. *Superconductor Science and Technology*, 22(7):075009, 2009.

[175] P.C. McIntyre, M.J. Cima, M.F. Ng, R.C. Chiu, and W.E. Rhine. Texture development in Ba2YCu307–x films from trifluoroacetate precursors. *Journal of Materials Research*, 5(12):2771–2779, 1990.

[176] A. Gupta, R. Jagannathan, E. I. Cooper, E. A. Giess, J. I. Landman, and B. W. Hussey. Superconducting oxide films with high transition temperature prepared from metal trifluoroacetate precursors. *Applied Physics Letters*, 52(24):2077–2079, 1988.

[177] Y. Chen, C. Wu, G. Zhao, and C. You. An advanced low-fluorine solution route for fabrication of high-performance YBCO superconducting films. *Superconductor Science and Technology*, 25(6):069501, 2012.

[178] T. Araki and I. Hirabayashi. Review of a chemical approach to YBa2Cu3O7-x-coated superconductors-metalorganic deposition using trifluoroacetates. *Superconductor Science and Technology*, 16(11):R71, 2003.

[179] L. Soler, J. Jareño, J. Banchewski, S. Rasi, N. Chamorro, R. Guzman, R. Yáñez, C. Mocuta, S. Ricart, J. Farjas, P. Roura-Grabulosa, X. Obradors, and T. Puig. Ultrafast transient liquid assisted growth of high current density superconducting films. *Nature Communications*, 11(1), 2020.

[180] L. Ciontea, A. Angrisani, G. Celentano, T. Petrisor, A. Rufoloni, A. Vannozzi, A. Augieri, V. Galuzzi, A. Mancini, and T. Petrisor. Metal propionate synthesis of epitaxial YBa2Cu3O7-x films. *Journal of Physics: Conference Series*, 97:012302, 2008.

[181] M. Erbe, J. Hänisch, T. Freudenberg, A. Kirchner, I. Mönch, S. Kaskel, L. Schultz, and B. Holzapfel. Improved REBa2Cu3O7-x (RE = Y, Gd) structure and superconducting properties by addition of acetylacetone in TFA-MOD precursor solutions. *Journal of Materials Chemistry A*, 2(14):4932–4944, 2014.

[182] K. Nakaoka, M. Yoshizumi, Y. Usui, T. Izumi, and Y. Shiohara. Effect of solution composition on superconducting properties of YBCO derived from TFA-MOD process. *IEEE Transactions on Applied Superconductivity*, 23(3), 2013.

[183] K. Nakaoka, J. Matsuda, Y. Kitoh, T. Goto, Y. Yamada, T. Izumi, and Y. Shiohara. Influence of starting solution composition on superconducting properties of YBCO coated conductors by advanced TFA-MOD process. *Physica C: Superconductivity and its Applications*, 463-465(SUPPL.):519–522, 2007.

[184] K. Tada, J. Yoshida, N. Mori, K. Yamada, R. Teranishi, M. Mukaida, T. Kiss, M. Inoue, Y. Shiohara, T. Izumi, J. Matsuda, and K. Nakaoka. Growth process of Ba-poor YBCO film

fabricated by TFA-MOD process. *Physica C: Superconductivity and its Applications*, 468(15-20):1554–1558, 2008.

[185] Z. Xie, Z. Li, H. Lu, J. Xu, X. Luo, Y. Zhu, and Y. Wang. Manipulation of G1Ba2Cu3O7-x Film Properties by Simply Changing Growth Temperature with RF Sputtering Method. *Journal of Physics: Conference Series*, 1637(1):012069, 2020.

[186] M. Coll, J. Gázquez, A. Pomar, T. Puig, F. Sandiumenge, and X. Obradors. Stress-induced spontaneous dewetting of heteroepitaxial YBa2Cu3O7 thin films. *Physical Review B - Condensed Matter and Materials Physics*, 73(7):075420, 2006.

[187] X. Obradors, F. Martínez-Julián, K. Zalamova, V. R. Vlad, A. Pomar, A. Palau, A. Llordés, H. Chen, M. Coll, S. Ricart, N. Mestres, X. Granados, T. Puig, and M. Rikel. Nucleation and mesostrain influence on percolating critical currents of solution derived YBa2Cu3O7 superconducting thin films. *Physica C: Superconductivity and its Applications*, 482:58–67, 2012.

[188] I. Park, W.J. Oh, J.H. Lee, S.H. Moon, and S.I. Yoo. Stability Phase Diagram of GdBa2Cu3O7-$\delta$ for the Nominal Composition of Gd:Ba:Cu = 1:1:2.5 in Low Oxygen Pressures. *IEEE Transactions on Applied Superconductivity*, 28(4), 2018.

[189] W Wong-Ng and L P Cook. Liquidus Diagram of the Ba-Y-Cu-O System in the Vicinity of the Ba2YCu3O6+x Phase Field. *Journal of Research of the National Institute of Standards and Technology*, 103(4):379–403, 1998.

[190] C. Pop, B. Villarejo, F. Pino, B. Mundet, S. Ricart, M. de Palau, T. Puig, and X. Obradors. Growth of all-chemical high critical current YBa2Cu3O7-$\delta$ thick films and coated conductors. *Superconductor Science and Technology*, 32(1):015004, 2019.

[191] P. Darapaneni, N..S. Moura, D. Harry, D.A. Cullen, K.M. Dooley, and J.A. Dorman. Effect of Moisture on Dopant Segregation in Solid Hosts. *Journal of Physical Chemistry C*, 123(19):12234–12241, 2019.

[192] E Bartolomé, J Alcalà, F Vallès, T Puig, X Obradors, N Pompeo, A Alimenti, K Torokhtii, F Rizzo, A Augieri, G Celentano, E Silva, and A Palau. Vortex pinning properties at dc and microwave frequencies of YBa2Cu3O7-x films with nanorods and nanoparticles. *Superconductor Science and Technology*, 33(7):074006, jun 2020.

[193] F Vallès, A Palau, D Abraimov, J Jaroszynski, A-M. Constantinescu, B Mundet, X Obradors, D Larbalestier, and T Puig. Optimizing vortex pinning in YBa2Cu3O7-x superconducting films up to high magnetic fields. *Communications Materials*, 3(1):1–11, 2022.

[194] K. De Keukeleere, P. Cayado, A. Meledin, F. Vallès, J. De Roo, H. Rijckaert, G. Pollefeyt, E. Bruneel, A. Palau, M. Coll, S. Ricart, G. Van Tendeloo, T. Puig, X. Obradors, and I. Van Driessche. Superconducting YBa2Cu3O7-$\delta$ Nanocomposites Using Preformed ZrO2 Nanocrystals: Growth Mechanisms and Vortex Pinning Properties. *Advanced Electronic Materials*, 2(10):1600161, 2016.

[195] L. Civale, B. Maiorov, J. L. MacManus-Driscoll, H. Wang, T. G. Holesinger, S. R. Foltyn, A. Serquis, and P. N. Arendt. Identification of intrinsic ab-plane pinning in YBa2Cu3O7 thin films and coated conductors. *IEEE Transactions on Applied Superconductivity*, 15(2):2808–2811, 2005.

[196] S. R. Foltyn, H. Wang, L. Civale, Q. X. Jia, P. N. Arendt, B. Maiorov, Y. Li, M. P. Maley, and J. L. MacManus-Driscoll. Overcoming the barrier to 1000 A / cm width superconducting coatings. *Applied Physics Letters*, 87(16):1–3, 2005.

[197] J. Gazquez, R. Guzman, R. Mishra, E. Bartolomé, J. Salafranca, C. Magén, M. Varela, M. Coll, A. Palau, S. M. Valvidares, P. Gargiani, E. Pellegrin, J. Herrero-Martin, S.J. Pennycook, S.T. Pantelides, T. Puig, and X. Obradors. Emerging Diluted Ferromagnetism in High-Tc Superconductors Driven by Point Defect Clusters. *Advanced Science*, 3(6):1500295, 2016.

[198] N. M. Strickland, A. Semwal, G. V.M. Williams, D. T. Verebelyi, and W. Zhang. Optimizing the doping state of YBCO coated

conductors. *Superconductor Science and Technology*, 17(9):S473, 2004.

[199] H. Castro and G. Deutscher. Anomalous Fermi liquid behavior of overdoped high-Tc superconductors. *Physical Review B - Condensed Matter and Materials Physics*, 70(17):1–8, 2004.

[200] M Miura, B Maiorov, M Sato, M Kanai, T Kato, T Kato, T Izumi, S Awaji, P Mele, M Kiuchi, and T Matsushita. Tuning nanoparticle size for enhanced functionality in perovskite thin films deposited by metal organic deposition. *NPG Asia Materials*, 9(11):e447, 2017.

[201] X.D.A. Baumans, J. Lombardo, J. Brisbois, G. Shaw, V.S. Zharinov, G. He, H. Yu, J. Yuan, B. Zhu, K. Jin, R.B.G. Kramer, J. Van de Vondel, and A.V. Silhanek. Healing Effect of Controlled Anti-Electromigration on Conventional and High-Tc Superconducting Nanowires. *Small*, 13(26):1700384, 2017.

[202] H. Y. Zhai and W. K. Chu. Effect of interfacial strain on critical temperature of YBa2Cu3O7-$\delta$ thin films. *Applied Physics Letters*, 76(23):3469–3471, 2000.

[203] M. Mazini, S. Favre, D. Ariosa, and R. Faccio. Substrate and thickness influence on YBa2Cu3O7-$\delta$ thin films grown by PLD deposition. *Applied Physics A: Materials Science and Processing*, 128(12):1–13, 2022.

[204] J. M. Triscone, O. Fischer, O. Brunner, L. Antognazza, A. D. Kent, and M. G. Karkut. YBa2. *Physical Review Letters*, 64(7):804, 1990.

[205] Q. Li, X. X. Xi, X. D. Wu, A. Inam, S. Vadlamannati, W. L. McLean, T. Venkatesan, R. Ramesh, D. M. Hwang, J. A. Martinez, and L. Nazar. Interlayer coupling effect in high-Tc superconductors probed by YBa2Cu3O7-x/PrBa2Cu3O7-x superlattices. *Physical Review Letters*, 64(25):3086, 1990.

[206] R. Arpaia, E. Andersson, E. Trabaldo, T. Bauch, and F. Lombardi. Probing the phase diagram of cuprates with YBa2Cu3O7-$\delta$ thin films and nanowires. *Physical Review Materials*, 2(2):024804, 2018.

[207] H. W. Zandbergen, R. Gronsky, and G. Thomas. Surface decomposition of superconducting YBa2Cu3O7. *physica status solidi (a)*, 105(1):207–218, 1988.

[208] N. Gauquelin, D. G. Hawthorn, G. A. Sawatzky, R. X. Liang, D. A. Bonn, W. N. Hardy, and G. A. Botton. Atomic scale real-space mapping of holes in YBa2Cu3O6+$\delta$. *Nature Communications 2014 5:1*, 5(1):1–7, jul 2014.

[209] S. Marinković, A. Fernández-Rodríguez, E. Fourneau, M. Cabero, H. Wang, N. D. Nguyen, J. Gazquez, N. Mestres, A. Palau, and A. V. Silhanek. From Electric Doping Control to Thermal Defect Nucleation in Perovskites. *Advanced Materials Interfaces*, 9(34):2200953, 2022.

[210] Z. Wan, Z. Liu, Q. Zhang, Q. Zhang, and M. Gu. Laser Technology for Perovskite: Fabrication and Applications. *Advanced Materials Technologies*, page 2302033, 2024.

[211] S. Collienne, S. Marinković, A. Fernández-Rodríguez, N. Mestres, A. Palau, and A.V. Silhanek. Electrically-Driven Oxygen Vacancy Aggregation and Displacement in YBa2Cu3O7-$\delta$ Films. *Advanced Electronic Materials*, 8(9):2101290, 2022.